MRI Cell-labeling with Xenon Nanocarriers

Inaugural-Dissertation
to obtain the academic degree
Doctor rerum naturalium (Dr. rer. nat.)

submitted to the
Department of Biology, Chemistry and Pharmacy
of Freie Universität Berlin

by
Diplom-Ingenieur Stefan Klippel
from Zittau

2015

This work has been carried out from January 2011 to January 2015 at the Leibniz-Institut für Molekulare Pharmakologie (FMP) in Berlin and the Freie Universität (FU) Berlin under the supervision of Dr. Leif Schröder and Prof. Dr. Christian Freund.

First reviewer: Dr. Leif Schröder
Molecular Imaging Group
Leibniz-Institut für Molekulare Pharmakologie (FMP)
Robert-Rössle-Str. 10
13125 Berlin

Second reviewer: Prof. Dr. Christian Freund
Protein Biochemistry Group
Institute of Chemistry and Biochemistry
Freie Universität (FU) Berlin
Thielallee 63
14195 Berlin

Thesis defense: 01.06.2015

Contents

Summary

Medical imaging has the potential to significantly improve our capabilities to understand, diagnose and treat diseases. Novel strategies include cell-tracking with non-targeted contrast agents in basic research and molecular imaging with targeted contrast agents for clinical applications. Both strategies rely on the sensitive detection of labeled cells by non-invasive modalities such as PET, SPECT, CT and MRI. Among these, MRI is the only modality that avoids the use of ionizing radiation. Nevertheless, it suffers from the low sensitivity of conventional relaxivity-based contrast agents (ca. 10^{-4} M detection limit). Molecular imaging applications that require nanomolar sensitivity are therefore restricted. Hyperpolarized xenon MRI in combination with indirect detection of xenon nanocarriers (hyper-CEST) overcomes this limitation by a 10^{7}-fold signal gain.

The MRI signal of the noble gas xenon is therefore dramatically enhanced by laser induced spin exchange optical pumping (SEOP) which further allows for the *in vivo* localization of dissolved xenon within organs such as the brain and the heart following inhalation. In addition, different synthetic as well as biological structures that serve as temporal hosts for xenon atoms have been identified. These nanocarriers are ideal contrast agents for xenon MRI since their indirect detection by chemical exchange saturation transfer combines high sensitivity (nano to picomolar concentrations) with the potential for multiplexing, functionalization and even genetic encoding.

Within this study, substantial progress for cell-labeling with synthetic xenon nanocarriers including cryptophane-A cages (CrA) and perfluorcarbon nanodroplets (PFOB) could be achieved. Unspecific cell-labeling with unmodified CrA and PFOB was established as a labeling scheme for potential cell-tracking applications. Specific cell-labeling for the purpose of molecular imaging was confirmed for three different functionalized CrA molecules targeting cell surface epitopes (CD-14, EGF-receptors and metabolically labeled glycans). The functionalization strategies include modular antibody conjugation, scaffolding as well as the coupling of a bioorthogonal group. It was demonstrated for the first time, that the achievable labeling concentrations (micromolar to nanomolar) are indeed sufficient for the *in vitro* MRI localization of labeled cells by exploiting the signal amplification of indirect hyper-CEST detection. Further on, the frequency selectivity of the hyper-CEST principle has been employed for the multiplexed detection of CrA- and PFOB labeled cells. The multiplexing concept was demonstrated for non-targeted xenon nanocarriers and can be translated to specific labeling applications with functionalized versions in the future. Final *in vitro* MRI experiments have been performed in an advanced imaging setup (bioreactor) under physiological conditions with live cells. The setup simulates *in vivo*-like xenon delivery by cell perfusion with xenon saturated medium. All achievements were further discussed with respect to recent developments within the field.

The thesis therefore provides a detailed *in vitro* characterization of MRI cell-labeling with xenon nanocarriers and thereby addresses the fundamental need for a successful translation of the concept to preclinical cell-tracking and molecular imaging applications.

Zusammenfassung

Neue Konzepte auf dem Gebiet der medizinischen Bildgebung haben das Potential unsere Möglichkeiten zum Verständnis, der Diagnose und der Heilung von Krankheiten entscheidend zu verbessern. Diese Strategien beinhalten sowohl die Zellverfolgung mittels nicht-zielgerichteter Kontrastmittel im Bereich der Grundlagenforschung, als auch molekulare Bildgebung mit Hilfe von zielgerichteten Kontrastmitteln für klinische Anwendungen. Beide Verfahren basieren auf der sensitiven Detektion von markierten Zellen mittels nicht-invasiver Bildgebungsmethoden wie PET, SPECT, CT und MRT. Von diesen ist MRT das einzige Verfahren, welches nicht auf dem Einsatz ionisierender Strahlung beruht. Die Verwendung von MRT im Bereich der molekularen Bildgebung ist jedoch aufgrund der relativ geringen Sensitivität konventioneller, relaxations-basierter Kontrastmittel limitiert.

MRT von hyperpolarisiertem Xenon in Kombination mit der indirekten Detektion von Xenon Nanoträgern (hyper-CEST) ermöglicht es, diese Beschränkung aufgrund einer etwa 10^7-fachen Signalverstärkung zu überwinden. Das MRT-Signal des ungiftigen Edelgases Xenon wird zu diesem Zweck erheblich mittels laser-induziertem “spin exchange optical pumping (SEOP)“ verstärkt. Diese Signalverstärkung ermöglicht es anschließend, die Verteilung von gelöstem Xenon in Organen wie dem Gehirn oder dem Herzen, nach dessen Inhalation zu detektieren. Zudem wurden verschiedene synthetische als auch biologische Strukturen identifiziert, die als temporärer Wirt für Xenonatome fungieren. Diese Nanoträger stellen ideale Kontrastmittel für Xenon-MRT dar, da ihre indirekte Lokalisierung mittels “chemical exchange saturation transfer“ (CEST) hohe Sensitivität (nano- bis pikomolar) mit der Möglichkeit zur Mehrfachdetektion, Funktionalisierung und genetischen Kodierung verbindet.

Im Rahmen dieser Arbeit konnten erhebliche Fortschritte bei der Markierung von Zellen mit synthetischen Xenon-Nanoträgern erzielt werden. Bei den verwendeten Nanoträgern handelt es sich um Cryptophan-A Käfige (CrA) und Perfluorcarbon-Nanotröpfchen (PFOB). Unspezifische Zellmarkierung mit nicht-modifiziertem CrA und PFOB wurde als eine Markierungsstrategie für potentielle Anwendungen der Zellverfolgung etabliert. Spezifische Markierung von zellulären Oberflächenstrukturen (CD-14, EGF-Rezeptor, metabolisch markierte Glykane) zum Zwecke der molekularen Bildgebung wurde für drei unterschiedlich funktionalisierte CrA-Konjugate nachgewiesen. Die verwendeten Funktionalisierungsstrategien umfassen die modulare Konjugation mit Antikörpern, den Einsatz von zielgerichteten Gerüststrukturen sowie die Kopplung einer bioorthogonalen Gruppe.

Es wurde zum ersten Mal gezeigt, dass die erzielbaren Markierungskonzentrationen (mikromolar bis nanomolar) in der Tat ausreichend sind, um die *in vitro* MRT Lokalisierung von markierten Zellen unter Ausnutzung der Signalverstärkung durch indirekte hyper-CEST Detektion zu ermöglichen. Des Weiteren wurde die Frequenzselektivität des hyper-CEST Prinzips zur Mehrfachdetektion von CrA- und PFOB markierten Zellen eingesetzt.

Das Konzept wurde für nicht-modifizierte Xenon-Nanoträger demonstriert und kann in der Zukunft auf Anwendungen mit funktionalisierten Nanoträgern übertragen werden.

Weiterführende *in vitro* MRT-Experimente wurden in einem neu entwickelten Bildgebungsaufbau (Bioreaktor) mit lebenden Zellen und unter physiologischen Bedingungen durchgeführt. Der Aufbau simuliert die *in vivo*-Anlieferung von Xenon durch Zellperfusion mit Xenon-gesättigtem Medium.

Die vorgelegte Studie liefert die Grundlagen für eine detaillierte *in vitro*-Charakterisierung der MRT-Zellmarkierung mit Xenon-Nanoträgern. Eine solche Charakterisierung ist die Vorrausetzung für eine erfolgreiche Übertragung des Konzeptes hin zu präklinischen Anwendungen auf dem Gebiet der Zellverfolgung und der molekularen Bildgebung.

1. Introduction

1.1. Cell-labeling in medical imaging

1.1.1. Medical imaging: A brief introduction

"Medical imaging comprises different imaging modalities and processes to image the human body for diagnostic and treatment purposes and therefore has an important role in the improvement of public health in all population groups. Furthermore, medical imaging is justified also to follow the course of a disease already diagnosed and/or treated."

- World Health Organization (WHO), 2014 -

Within the last century, the noninvasive diagnosis of diseases based on investigating anatomical and cellular structures became an indispensable part of medicine itself. In 1896, Edwin Frost reported the first clinical image of a bone fracture that was recorded by using X-rays, only 3 month after the discovery of this to that point unknown type of electromagnetic radiation by Wilhelm Röntgen.[1] For his discovery, Röntgen was honored with the Nobel Prize in physics in 1901. In 1955, Ian Donald started to investigate the use of ultrasound (US) to diagnose gynaecological patients. Thirty years later ultrasound imaging became a routine procedure in prenatal diagnosis. Another milestone in the timeline of medical imaging was the first patient brain scan in 1971 recorded by computed tomography (CT), an X-ray based imaging technique conceived by Godfrey Hounsfield 4 years before. Hounsfield and Cormack got the Nobel Prize in physiology or medicine for the development of CT in 1979. In 1974 Michael Phelps and coworkers invented the first whole-body system for positron emission tomography (PET), a functional imaging modality that is today routinely used in clinical oncology worldwide. 1973 Paul Lauterbur reported the first magnetic resonance image (MRI), while three years later the first MRI human body scan was performed on a scanner developed by Raymond Damadian, Larry Minkoff and Michael Goldsmith. Since 1980 MR imaging has been routinely used in hospitals. Paul Lauterbur and Peter Mansfield share the 2003 Nobel prize in physiology or medicine for their work related to the development of MRI.[2]

The development of noninvasive imaging techniques such as CT, US, MRI and PET lead to a revolution of clinical diagnosis on one hand but also helped significantly to improve our understanding of disease as a basic tool in fundamental research.

The possibility to diagnose disease strongly benefits from the development of tracer substances that are capable to enhance the inherent contrast provided by a certain imaging technique in order to detect abnormalities. The distribution of these so called contrast agents within the body improves the

visualization of anatomical structures such as organs, blood vessels, different tissue types as well as regions of enhanced metabolic activity.

Contrast agents have a special importance in oncology, a subfield of medicine that deals with the detection, characterization and treatment of malignant cells that form tumors. In "classical" medical imaging the detection of solid tumors is mainly based on the visualization of abnormal anatomical structures. Conventional contrast agents can help to improve the detectability of such morphological changes for example by an unspecific accumulation within malignant tissue. This accumulation is a result of an enhanced vascular permeability that occurs in tumors and surrounding tissue.[3] One prominent example for such indications is gadopentetate dimeglumine (Magnevist), the first intravenous MRI contrast agent which was clinical approved in 1987 and that reached more than 120 million administrations from 1988 to 2011.[4]
Nevertheless, the efficient detection and treatment of tumors by using such established imaging strategies is restricted as underlined by a quote from Schreiber and Rowley (2010)[5] claiming that:

"Human cancers when first detected usually have an average diameter of at least 1 cm and contain about 10^9 cancer cells, including thousands of diverse heritable variants resistant to drugs, radiation, and immunotherapy."

In this context the detection of cancer at an early stage is essential since the probability of successful treatment based on radiation, chemotherapy or curative approaches is significantly improved at this time point. In one example given by Hussain and Nguyen (2014)[6] the survival rates for patients with non-small cell lung cancer (NSCLC) has been analyzed based on the 2010 National Cancer Database. In 60 %, patients had a cancer removal surgery when diagnosed at stage I while only 6 % had a surgery when diagnosed at stage III. Patients that had a resection showed a 5-year survival rate of 60–80 % for stage I and 40–50 % for stage II cancers. On the other hand stage III patients that had to be treated with chemotherapy instead of surgery had a 2-year survival rate of less than 20 %.

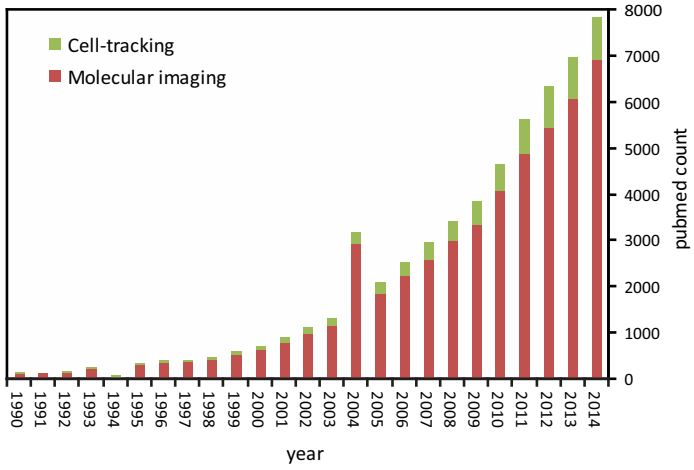

Figure 1.1:
Biomedical literature and publications related to Molecular imaging (red bars) and Cell-tracking (green bars) sorted per year starting from 1990. The online search was done in December 2014 using the PubMed database provided by the National Center for Biotechnology Information (NCBI).

Overall, the detection of cancers at stage I is associated with a 90 % 5-year survival rate while detection at the premalignant stage (before stage 1) is in most cases curative.[7] Cancer is still one of the main public health problems in modern societies. In 2014 around 25 % of all death cases in the USA have been related to cancer.[8] In 2008 the World Health Organization (WHO) reported of 7.9 million cancer deaths (ca. 13 % of all deaths) worldwide while estimations suggest a triplication of this number by 2030 under the given medical standards.[9]

On the background of this dramatical development novel subfields of medical imaging evolved within the last three decades aiming for an improvement in early diagnosis and treatment of cancer and disease in general. One of these subfields is molecular imaging, which relies on the development of contrast agents that are designed to specifically label disease associated cells types or molecular targets in a selective manner. A second subfield of modern medical imaging is the noninvasive localization of therapeutic cells, a research area that is known as cell-tracking. The growing interest in this novel imaging areas is reflected by a strong increase of biomedical publications related to molecular imaging and cell-tracking as shown in figure 1.1.

1.1.2. Cell-labeling strategies

Figure 1.2 gives a simplified overview about the two different cell-labeling strategies to which novel conceptual ideas have been developed in this thesis for the purpose of either cell-tracking or molecular imaging. In cell-tracking, cells are labeled *ex vivo* by means of unspecific labeling with non-targeted contrast agents. In case of molecular imaging the contrast agent is conjugated to a targeting unit which allows for specific *in vivo* cell-labeling after systemic administration.

1.1.2.1. Cell-tracking

Motivated by the need for novel ways to treat diseases, cellular therapy has become an active area of research.

"Cellular therapy is the treatment of disease using therapeutic cells that have been derived from the patient, a matched donor, other organisms, or immortalized cell lines. Often these cells are sorted, multiplied, pharmacologically treated and/or genetically transformed in culture prior to infusion or transplantation into a patient. Therapeutic cells have the potential to accomplish complex tasks such as the regeneration of tissues, for example replacing cartilage or brain cells or to re-program a patient's immune system, for example, to elicit an anti-tumor response." [10]

Cell-tracking describes imaging strategies that allows studying the *in vivo* behavior of injected or transplanted therapeutic cells such as stem- or immune cells in a non-invasive manner. It is therefore an essential part of preclinical and clinical studies and enables the monitoring of cell-delivery and cell fate in order to evaluate and optimize cell therapeutic applications. For this purpose therapeutic cells are in most cases labeled *ex vivo* with contrast agents in an unspecific manner. In this context the main issue is to keep the cellular phenotype and function unaffected by the labeling event in order to retain the therapeutic potential of the cells. Next to this, a high amount of contrast agent per cell is desired for an efficient detection of low cell numbers. A detailed summary about the progress of cell based therapy in basic research and clinical translation can be found in Koh and Suck (2012)[11].

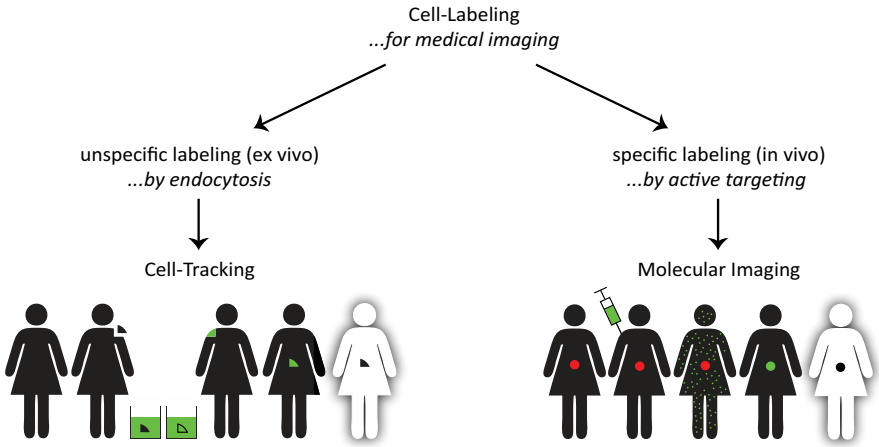

Figure 1.2: Schematic of the different cell-labeling strategies to which contributions have been made in this thesis and their potential contribution to modern medical imaging. Cell-tracking applications (left): Therapeutic cells (here patient derived) are extracted, manipulated and further labeled with a non-targeted contrast agent (green) by unspecific cell uptake (endocytosis). The labeled cell material is further injected to the patient while cell fate can be studied by noninvasive imaging. Molecular imaging applications (right): A targeted contrast agent is administered parentally (here by injection). The contrast agent gets further distributed within the patient's body. A tumor (red) gets specifically labeled by the contrast agent (e.g. via interactions between an antibody and cancer cell specific surface structures). Non-invasive imaging allows for tumor detection.

1.1.2.2. Molecular imaging

"Generally speaking, molecular imaging involves specialized instrumentation, used alone or in combination with targeted imaging agents, to visualize tissue characteristics and/or biochemical markers. The data generated from molecular imaging studies can be used to help understand biological phenomena, identify regions of pathology, and provide insight regarding the mechanisms of disease." [9]

The development of targeted contrast agents for biomarkers that are characteristic for early states of disease is a major aspect in molecular imaging. Such biomarkers can be extra- and intracellular proteins (receptors, transporters and enzymes) as well as glycan structures or even DNA/RNA.

One example in oncology are targeted contrast agents that are specific for transmembrane proteins of the integrin family that are highly abundant on tumor endothelial cells in general.[12] On the other hand, targeted probes that are specific to a certain cancer type have been reported. Such specific probes can improve the diagnostic information content which allows for a more specialized therapeutic treatment. Examples for such cancer-type specific target structures are antigens that are correlated with prostate cancer [13] or pancreatic cancer [14].

Other molecular imaging studies within the field of oncology were aiming for the detection of angiogenesis, hypoxia, proliferation, tumor metabolism, apoptosis and metastasis. In neuroscience, neurodegenerative diseases as well as neuroinflammatory conditions have been targeted while other studies were performed to access cardiovascular disease such as arteriosclerosis or even heart failures. A summary about the different application routes of molecular imaging is given by James and Gambhir (2012)[9].

Different targeting units such as peptides, engineered antibodies or antibody fragments, small molecules, aptamers or bioorthogonal groups are established while the main criteria is the achievement of high affinity paired with target specificity. In most cases, the final imaging probe is designed for a systemic administration that allows for an in depth penetration of diseased tissue and a sufficient washout time to eliminate unspecific interactions.

The specific labeling of cells *in vivo* therefore requires some key criteria for targeted contrast agents such as: reasonable pharmacodynamics, the ability to overcome biologic delivery barriers (vascular, interstitial, cell membrane) as well as the availability of a sensitive, fast, high-resolution imaging technique for *in vivo* detection.[15]

1.1.3. Comparison of imaging modalities

Independent of the applied cell-labeling scheme, the contrast agent of choice and its corresponding imaging modality should be highly sensitive in order to detect a minimal amount of labeled cells *in vivo*. Ideally, the applied imaging strategy should have no negative impact on the patients' health. The most important imaging modalities with relevance for clinical whole body imaging are: Computed tomography (CT), Positron-emission-tomography (PET) and Magnetic resonance imaging (MRI).

In CT anatomical information is generated based on differences in the attenuation of X-rays passing through the body. CT is comparably fast and achieves a high spatial resolution (0.5–1.0 mm). Next to this, it is relatively inexpensive and CT scanners are widely available. One of the main concerns is the use of ionizing radiation for image acquisition that limits the number of scans per patient. Classical CT contrast agents are based on iodinated molecules that efficiently absorb X-rays. These agents are typically used to overcome the low soft tissue contrast of CT.[9] Nevertheless they are not suited for molecular imaging and cell-tracking because they are relatively insensitive (millimolar concentrations are required for detection) and have limited targeting performance[16]. Novel contrast agents such as bismuth sulfite nanoparticles have been developed that have the potential to overcome this limitation in the future.[17]

PET imaging detects the distribution of instable radionuclide tracers (^{18}F, ^{11}C, ^{68}Ga) within the body. The tracers decay under positron emission which subsequently during annihilation leads to the emission of highly energetic photons (gamma-rays) that are detected. The most prominent PET-tracer, ^{18}F-2-fluoro-2-deoxy-glucose, is accumulated within malignant cells based on their enhanced glucose metabolism.[18] PET-tracers show an excellent sensitivity (picomolar concentrations) and have therefore an important role in clinical cancer detection today.[6] The main limitation of PET imaging is the production of ionizing radiation. Other limitations include a very low spatial resolution (5-7 mm) and a limited specificity of traditional PET-tracers that are accumulated in tumor cells by metabolic labeling instead of active targeting[19]. The technique is relatively expensive since cyclotrons are needed for the production of the instable tracer molecules. The restricted half life time of the radiotracers further hinders prolonged cell-tracking applications. PET imaging alone gives no information about the defined anatomical localization of a certain tracer signal. This restriction led to the development of combined PET/CT scanners that pair the advantages of both modalities (PET: high sensitivity, functional information, CT: high resolution, anatomical information).

Nevertheless the health risk that is related to radiation exposure in CT and PET has to be considered. In a recent study performed by Huang et al (2009)[20] the lifetime cancer incidence was estimated for an typically PET/CT scan:

"…the effective dose from ^{18}F-FDG PET/CT scanning with a diagnostic CT protocol and an administered FDG activity of 370 MBq was calculated to be up to 32.18 mSv, and the associated lifetime cancer incidence was estimated to be up to 0.514 % for the U.S. population and up to 0.622 % for the Hong Kong population (for patients 20 years of age). The results are important from both an individual and a public health perspective."

Based on this estimation, it is questionable if CT/PET is an valid strategy for molecular imaging applications that aims for an early stage cancer diagnosis since such indications would require imaging sessions to be done in a routinely manner. On this background, MRI is the image modality of choice since high energy radiation is not necessary.

In conventional proton detected MRI, anatomical information is achieved by localizing magnetic properties of water protons within the body. Therefore strong magnetic fields (typically ca. 3 T) are used in combination with low energy radiofrequency radiation.

MRI is characterized by a high soft tissue contrast, a high spatial resolution (ca. 1 mm) and it is widely used for anatomical imaging in clinics. Conventional MRI contrast agents such as iron oxide nanoparticles or gadolinium chelates modulates the magnetic properties of surrounding water protons. These contrast agents can be functionalized with targeting units which lead to the development of molecular imaging probes for cancer biomarkers such as the transferrin receptor [21] or folate receptors [22]. In addition iron oxide nanoparticles are widely used for cell-tracking applications based on beneficial properties when compared to PET-tracers that are associated with cytotoxicity concerns.[23]

The main limitation of conventional MRI contrast agents is their low sensitivity (micromolar concentrations are required)[24] in comparison to PET contrast agents that are more sensitive by several orders of magnitude. This sensitivity limitation is problematic, especially for molecular imaging applications aiming for the detection of low concentrated (nanomolar concentrations) disease markers.[25]

A detailed overview and comparison of imaging modalities with relevance for molecular imaging, their current applications as well as future directions can be found in Ref. [6,9,25]. For a comprehensive scheme of cell-tracking techniques with focus on MRI see Ref. [23].

1.1.4. General achievements in MRI cell-labeling

To capitalize on the superior resolution and the safety of MRI, different approaches have been developed to overcome the sensitivity limitation related to conventional relaxivity-based contrast agents (typically micromolar concentrations are required)[24]. The following section gives a brief overview about recent developments.
A basic understanding about the theory of Nuclear Magnetic Resonance Imaging (MRI) is assumed. An comprehensive introduction to MRI is given by Hashemi et al. (2012)[26]. MRI contrast agents can be divided into two classes based on the detected nuclei: (i) proton detected contrast agents and (ii) X-nuclei detected contrast agents:

(i) A conventional clinical MRI scanner detects water protons that are abundant throughout the human body. The contrast is based on different relaxation properties of these protons that depend on their physicochemical environment and tissue properties.

(i,a) Conventional contrast agents in proton detected MRI modulate the relaxation rates (R_1: paramagnetic Gd-chelates, R_2: superparamagnetic iron oxid nanoparticles) of surrounding water protons. One indirect possibility to overcome the sensitivity limitation is to drastically increase the contrast agent concentration at a certain target side. Such amplification strategies have been developed especially for Gd-chelates. One example is the achievements of high Gd payloads within targeted perfluorcarbon (PFC) nanoparticles, an approach that allowed the detection of sparse cellular epitopes at picomolar concentrations.[27] Other strategies describe the design of so-called “smart probes” that are activated by cancer associated enzymes such as matrix metalloproteinase (MMP) followed by an accumulation of Gd at the target side.[28] Another strategy used Gd-chelates conjugated to cell penetrating peptides that are activated by MMPs. By doing so, the accumulation and subsequent detection of up to 50 µM Gd could have been achieved in cancer xenografts.[29]

(i,b) A novel class of contrast agents in proton detected MRI is based on chemical exchange saturation transfer (CEST).
“A CEST agent is a system containing mobile protons in slow/intermediate exchange with water proton resonances. Thus, on irradiation of the absorption of the exchanging protons, saturated magnetization is transferred to the water signal, thereby causing a decrease in its intensity.” [30]
Such systems have been optimized within the last years to meet the sensitivity criteria of molecular imaging applications. The most promising systems on this background are LipoCEST agents. The agents are designed from liposomes filled with paramagnetic lanthanide complexes. The presence of the lanthanide complexes shifts the resonance frequency of liposome entrapped water which creates a huge pool of exchangeable protons (10^6–10^8). Saturation transfer further allowed the detection of picomolare liposome concentrations.[31] First *in vivo* molecular imaging experiments with integrin-targeted lipoCEST agents have been performed recently.[32] The experiments revealed problems with

tumor specificity of the liposomes, an issue that needs to be optimized in the future. A well-written review about nanoparticle-based proton-CEST agents can be found in Castelli et al. (2013)[30].

(ii) MRI applications detecting the magnetization of nuclei different from protons (^{1}H) are known as X-nuclei MRI. On this background, the spin -½ nuclei ^{19}F, ^{13}C and ^{129}Xe are of specific interest for modern medical cell-labeling applications. The natural abundance of these NMR active isotopes within the body is typically low. Therefore strategies have been developed where such isotopes are used as MRI contrast agents. Conventional proton contrast agents rely on the modulation of the abundant water signal (concentration of ^{1}H is ca 100 M) and are therefore indirectly detected. In contrast, X-nuclei are detected directly. Due to the lack of an anatomical background signal, morphological information is provided by additional proton-MRI.

Nevertheless the NMR sensitivity of the given nuclear isotopes is quite different under physiological conditions as characterized by the spin polarization in thermal equilibrium [P_{th}]. As it can be seen in figure 1.3 the sensitivity of ^{19}F is comparable to ^{1}H. Therefore nanoemulsions formulated from ^{19}F-rich molecules (perfluorocarbons) can be applied as tracer substances in cell-tracking and molecular imaging applications without further manipulation. Examples for such applications are summarized on page 29.

Other X-nuclei such as ^{13}C and ^{129}Xe are far less sensitive (see figure 1.3) which makes their MRI detection at the achievable *in vivo* tracer concentrations (micromolar) impossible under standard conditions. To overcome this limitation, hyperpolarization strategies have been developed that dramatically increase the sensitivity for such nuclei by up to 5 orders of magnitude.[33] Hyperpolarization therefore enabled new possibilities for the detection of insensitive X-nuclei in medical MRI applications.

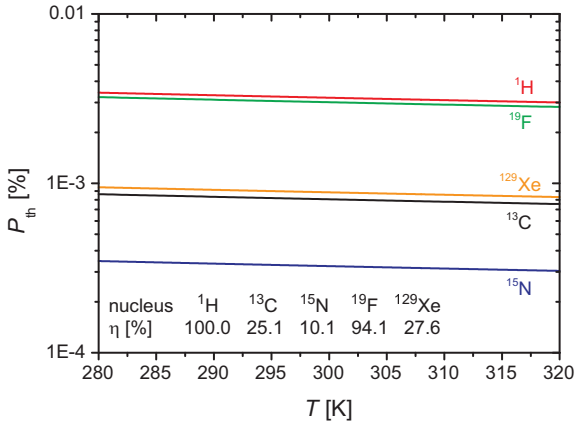

Figure 1.3: Thermal polarization of various nuclei used in biomedical NMR assuming a field strength of 9.4 T.
η represents the gyromagnetic ratio, normalized to the value for ^{1}H; the X nuclei, in particular, suffer from very low polarization around room temperature. Figure and figure caption from Ref. [33].

On this background, hyperpolarized ^{13}C-tracers such as 1-^{13}C-pyruvic acid have been developed for the purpose of metabolic imaging in disease like cancer.[34] The tracers have been primarily designed to study enzymatic biochemical processes at the cellular and tissue levels while classical targeting approaches such as receptor imaging are still restricted to initial studies.[35] In addition, long term cell-tracking with hyperpolarized ^{13}C is not achievable due to the restricted hyperpolarization lifetime.

The use of hyperpolarized ^{129}Xe for sensitive cell-labeling applications is subject of this thesis. The thesis was motivated by the need for alternative strategies in medical imaging with the aim to improve the early detection and treatment of disease, while avoiding the use of ionizing radiation. The following section gives a brief overview about relevant NMR and MRI properties of xenon followed by a summary of achievements in cell-labeling.

1.2. Xenon-129 in NMR spectroscopy and imaging

1.2.1. General properties

In 1898 the chemists William Ramsay and Morris Travers discovered xenon by fractional evaporation of liquid air. Xenon is a chemically inert, odorless, colorless and tasteless noble gas with the atomic number 54. As a zero-valence element, it is characterized by a stable configuration of its outer electron shell. Based on this minimum energy configuration xenon is not chemically reactive under standard conditions. Today xenon is used for the production of lasers, incandescent lamps, plasma display panels as well as in silicon etching, semiconductor manufacturing and in medicine.[36]

The use of xenon in medical applications is based on its nontoxic nature, its anesthetic properties[37] as well as on the special NMR characteristics of the xenon isotope 129. Two of the eight stable xenon isotopes have a non-zero intrinsic angular momentum and are therefore NMR active. These isotopes are xenon-129, a spin -1/2 nucleus with 26.4 % natural abundance and xenon-131, a spin -3/2 nucleus with a natural abundance of 21.2 %

Xenon-129 is of special interest for biomedical imaging due to some favorable NMR characteristics that are: (i) a very high sensitivity for different physicochemical environments that is displayed by a broad chemical shift range, (ii) its potential for signal enhancement by hyperpolarization and (iii) the property to form transient inclusion complexes with different xenon host structures or synthetic nanocarriers.

1.2.2. Chemical shift sensitivity

Xenon-129 has a large, highly polarizable electron cloud that shields the nucleus. Depending on the molecular environment, this electron cloud gets deformed resulting in a change within the effective magnetic field that is sensed by the nucleus within an NMR experiment. The resonance frequency of xenon that depends on the strength of the effective magnetic field is therefore a measure for changes within its immediate environment and reports on non-covalent interactions as well as on changes in temperature and pressure.[38]

Figure 1.4 shows chemical shift values for xenon within different biologically relevant environments such as xenon dissolved in water or blood, xenon bound to proteins (myoglobin) as well as xenon entrapped within synthetic supramolecular carbon structures (cryptophane-A). Relative to xenon within the gas phase, a broad chemical shift range of ca. 250 ppm is covered. The chemical shift sensitivity of xenon-129 has been used to study properties of materials[39,40] as well as biomolecules[41,42] by NMR spectroscopy in the past. The unique chemical shift of xenon within synthetic structures like cryptophanes is of special importance because it enables the detection of this xenon host within mixtures of biomolecules, tissue or potentially in whole organisms as discussed later on.

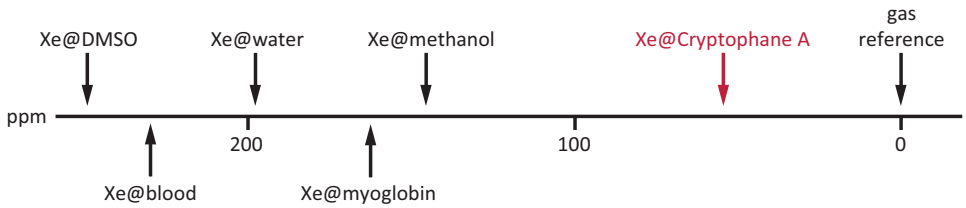

Figure 1.4: Chemical shift values of xenon in different chemical environments. Values are given relative to gaseous xenon at 0 ppm that serves as reference. The resonance for xenon within cryptophane A is highlighted in red to illustrate the unique chemical shift properties of synthetic xenon hosts structures. Figure adapted from Ref. [43].

1.2.3. Signal enhancement by hyperpolarization

NMR experiments with thermally polarized xenon dissolved within in aqueous environments are restricted by the low signal that is obtained. This low signal is a consequence of the relative low solubility of xenon within water that results in a low spin density. At 1 atmosphere pressure the amount of xenon gas dissolved in water is ca 3.3 mM. In addition, the gyromagnetic ratio of xenon-129 (γ= 11.842 MHz/T) is low when compared with other nuclei such as protons (γ= 42.576 MHz/T). Only ~9 spins in a million (B_0 = 9.4 T, room temperature) contribute to the detectable NMR signal (net magnetization) that is given by the population difference between the upper and the lower energy state for spin -1/2 nuclei within a magnetic field. In summary the NMR receptivity of xenon-129 in water is only 2.6 % when compared to protons. The possibility to perform NMR and MRI experiments with thermally polarized xenon in biological environments such as tissue is therefore strongly restricted.[44]

Nevertheless, the NMR signal of xenon-129 can be dramatically amplified by manipulating the population ratio R ($R = exp(-\gamma B_0/k)T$, *B_0: external magnetic field, k: Boltzmann constant, T: absolute temperature* , high temperature approximation) of the two xenon spin states. This process is called hyperpolarization. Xenon hyperpolarization can be achieved by spin exchange optical pumping (SEOP) a process that theoretically allows for an enhancement of the normalized polarization P ($P=(1-R)/(1+R)$) by up to five orders of magnitude as illustrated within figure 1.5.

In brief: Circularly polarized laser light (emission at 795 nm) is used to pump a specific energy transition (D_1 transition) of electrons in a rubidium vapor that is exposed to a magnetic field (ca. 2.5 mT). As a consequence a high rubidium electron spin polarization is achieved that is further converted into Xe nuclear spin polarization by dipolar interactions. For this purpose xenon gas is guided through the rubidium vapor while xenon spins in the lower energy state are converted into the higher spin state by flip-flop processes.[44] More details about the SEOP process concerning spin physics, setup, experimental conditions and their optimization can be found in Ref. [44–46].

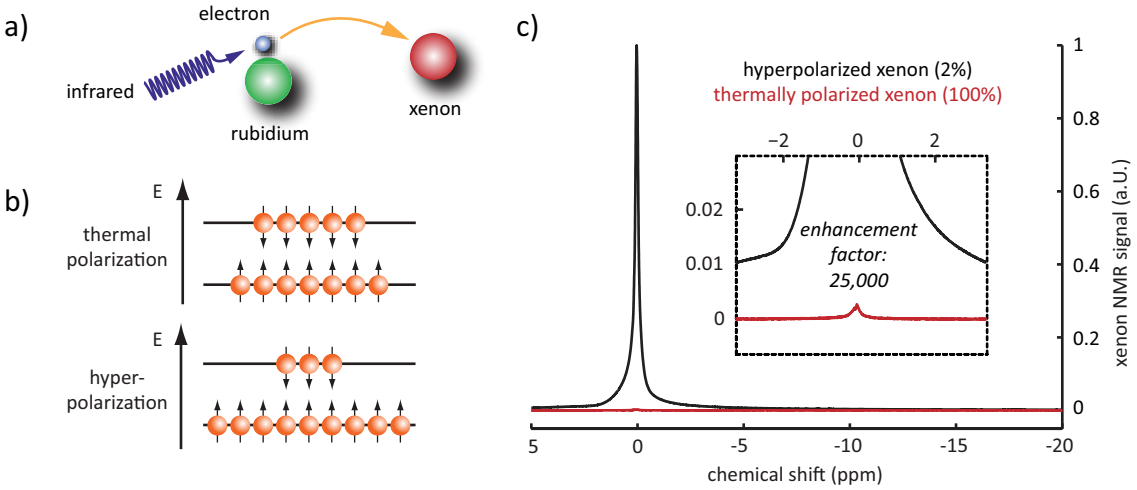

Figure 1.5: Xenon hyperpolarization by spin exchange optical pumping. Circular polarized laser light is used to hyperpolarize rubidium electrons. The hyper-polarization gets further transferred onto the nuclei of xenon atoms via direct spin-spin interactions (a, figure from Ref. [33]). As a consequence the population difference between both xenon spin states gets increased resulting in a strong enhancement of the NMR detectable net magnetization (b, figure from Ref. [44]). The enhancement (factor 25000) in the NMR signal is shown for a comparison of thermal polarized and hyperpolarized xenon gas. The shown NMR spectra were measured at 110 MHz with the hyperpolarization setup (25 % spin polarization) used within this thesis (c).

Modern hyperpolarizes can achieve high spin polarizations levels (up to 90 %) and produce substantial amounts of hyperpolarized xenon gas in short time (ca. 1 liter per hour). Due to favorable relaxation conditions, hyperpolarized xenon gas can be further stored in Tedlar bags (T_1 ca 2 h) for several hours. Therefore, the hyperpolarization process and the NMR measurement can be performed spatially and temporally independent from each other.[47]

As a consequence of the signal enhancement due to hyperpolarization, medical MR imaging and spectroscopy with hyperpolarized xenon (hp-xenon) evolved, including applications in basic research, preclinical animal studies as well as clinical studies with humans. Most preclinical/clinical studies in this context are related to lung void space imaging that is very challenging with conventional proton detected MRI due to the low proton spin density within the lung. For such purposes hp-xenon has to be inhaled by the patient followed by the localization of the gas-phase signal after distribution. The gas distribution further allows studying diseases that are related with ventilation defects such as asthma or chronic obstructive pulmonary disease (COPD), (see figure 1.6a).

Next to this, the chemical shift sensitivity of xenon is used to differentiate the distribution of xenon dissolved within lung tissue and blood (dissolved phase signal at ca. 210 ppm) from xenon within the lung air space (gas phase signal at 0 ppm). The time dependent ratio of both signals (dissolved and gas phase) is a measure of the gas uptake capability of the lung and allows to characterize the lung function and correlated defects in more detail (see figure 1.6b). A comprehensive review about the use of hyperpolarized xenon for clinical MRI of the human lung can be found in Mugler and Altes (2013)[48].

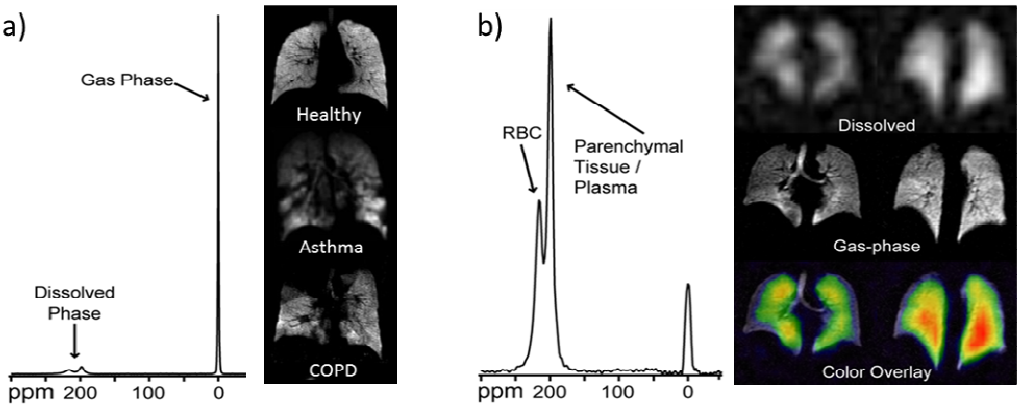

Figure 1.6. Human lung imaging and spectroscopy with inhaled hp-xenon. a) NMR spectrum of the lung showing a comparable small signal for xenon within the dissolved phase (ca. 210 ppm) and an intense signal from xenon within the gas phase at 0 ppm (left). MRI of the gas phase signal is used to visualize the lung void space and reveals regions of reduced ventilation capacity corelated to disease like Asthma or COPD (right). b) The dissolved phase signal arises from xenon in red blood cells (RBC) at 218 ppm and xenon in blood plasma and lung tissues at 197 ppm as shown for a NMR spectrum measured with a selective read out pulse (left). The dissolved phase signal and the gas phase signal can be imaged seperatily to study gas uptake as a measure of lung function (right). Figures are composed from Ref. [48,49].

Other preclinical studies with small animals demonstrated the detection of hp-xenon dissolved within brain tissue (see figure 1.7) following the inhalation of hp-xenon gas.[50–54] In one of these studies, the distribution of dissolved xenon has been used to map regions of brain stroke that are correlated with a lower xenon concentration. Such experiment therefore illustrate the potential to image even low concentrations of hp-xenon (ca. 20 µM in mouse brain) within strongly perfused organs[55]. Next to inhalation of xenon gas, other delivery routes that are for example based on continuous extracorporeal infusion are also under investigation. Initial results suggest the potential to deliver xenon to any organ of the body.[50,56]

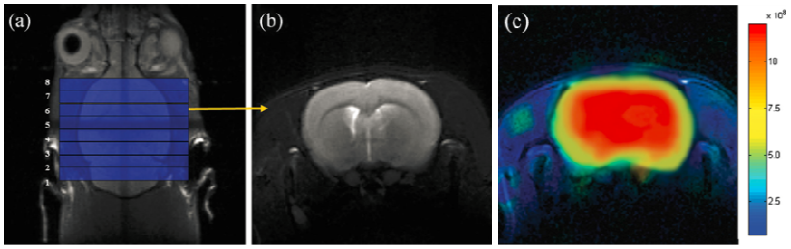

Figure 1.7: (a) Proton image of a rat brain. (b) Selected single slice that has been used as anatomical proton reference. (c) Overlay of proton reference slice and dissolved phase signal of hp-xenon (signal intensity in arbitrary units) following inhalation. Images are adapted from Ref. [51].

The mentioned clinical and preclinical MRI applications all rely on the localization of the unspecific distribution of hp-xenon within the body. On the background of desired cell-tracking and molecular imaging applications, xenon based contrast agents are necessary in order to achieve cell-labeling. For this purpose different xenon nanocarriers have been studied in the past.

1.2.4. Xenon nanocarriers

1.2.4.1. Cryptophane-A

The transient interaction of xenon with several molecules including supramolecular structures (cryptophanes[57], cyclodextrin[58], calixarene[59], curcubituril[60], crown ether[61]) as well as different proteins [41,42,62–64] has been confirmed in various publications. The mentioned molecules (see figure 1.8) form hydrophobic cavities that are temporarily occupied (several milliseconds) by the non-polar xenon atoms. As a consequence of this interaction, the resonance frequency of xenon gets changed. This allows differentiating free xenon in solution from xenon within the host structure.

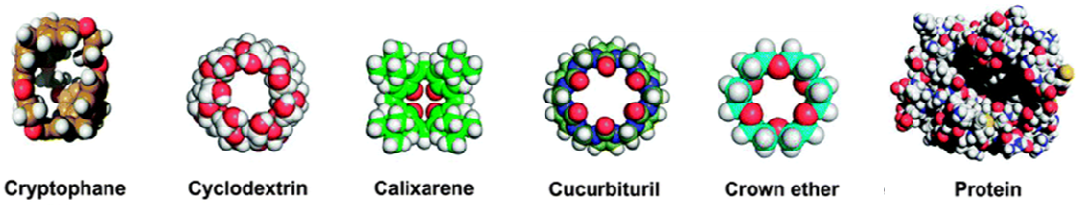

Figure 1.8: Nanocarriers for hyperpolarized xenon. Figure adapted and rearranged from Ref. [65].

The best characterized xenon host is cryptophane-A (CrA, cryptophane-222) a synthetic molecule that consists of two linked cyclotriveratrylene (CTV)-caps that are each formed by aromatic ring structures. Cryptophane-A forms a cage-like cavity with an inner volume of ca. 95 Å^3 that fits exactly one xenon atom with a volume of 42 Å^3 (see figure 1.9) by an induced fit mechanism[66]. The binding kinetics between xenon and CrA are nearly optimal for NMR measurements and are characterized by an affinity of K = 3900 M^{-1} in organic solvent (at 278 K) and a residence time of ca. 30 ms paired with minimal relaxation effects.[43] The resonance frequency of dissolved xenon (191 ppm) gets shifted by ca. 130 ppm by the entrapment within the cryptophane cage resulting in a chemical shift position of ca. 60 ppm for the complex as shown within figure 1.9.

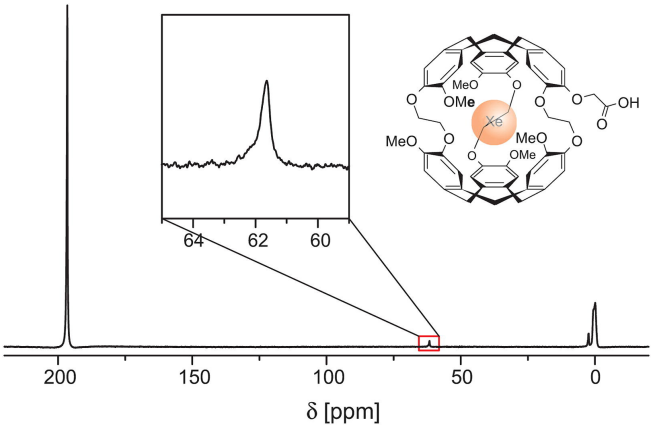

Figure 1.9: ^{129}Xe NMR spectrum of xenon dissolved in water with 5 % DMSO and 200 µM of the molecular cage cryptophane-A monoacid. Xenon in gas phase on top of the solution is used as reference at 0 ppm. Free Xe in solution resonates at ca. 191 ppm whereas atoms trapped in the cage cavity yield a signal at ca. 61.8 ppm. Figure and figure caption adapted from Ref. [44].

Importantly, the resonance frequency of xenon within CrA is well separated from other resonance frequencies reported for interactions between xenon and biomolecules (proteins, lipids), complex tissues or blood that occurs *in vivo* (see figure 1.4). This observation motivated the use of cryptophane molecules as a contrast agent for cell-labeling applications that can be detected based on the chemical shift information of hp-xenon. In this context, the chemical modification and functionalization of CrA with targeting units have been demonstrated.

1.2.4.2. Biosensor concept

A fundamental need for molecular imaging applications is the targeting potential of a certain contrast agent. For cryptophane-A this targeting potential has been demonstrated by Spence et al. in 2001[67]. The authors synthesized a CrA molecule that has been conjugated to biotin via a linker unit (figure 1.10, left). They further demonstrated that the binding of this functionalized CrA molecule to avidin can be monitored by a chemical shift change of ca. 2 ppm for cryptophane entrapped xenon (figure 1.10, right).

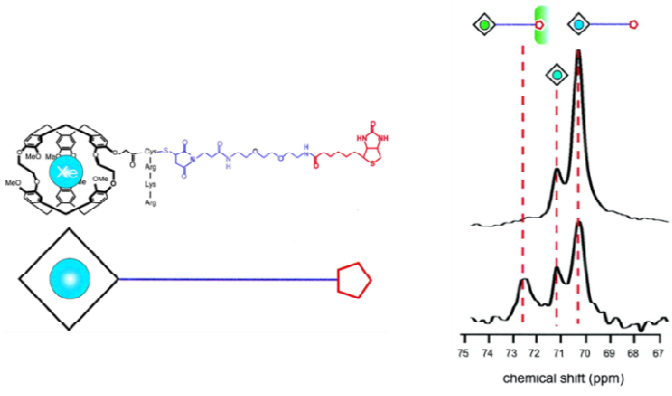

Figure 1.10: Prototype of a cryptophane-A based xenon biosensor. Cryptophane-A monoacid (black) has been conjugated to biotin (red) by a linker unit (blue). The cryptophane molecule was further coupled to a short peptide fragment to achieve solubility within aqueous environments. The unbound biosensor is detected at a xenon resonance frequency of ca. 70.3 ppm. The binding of the biosensor to avidin can be observed by the appearance of an additional xenon resonance at ca. 72.5 ppm. Figure adapted from Ref. [67].

The chemical shift sensitivity of xenon entrapped within functionalized cryptophane molecules gets therefore retained and allows to sense for the binding event of the conjugated targeting unit. This initial experiment describes the prototype of a targeted xenon contrast agent. Based on their potential to report on a certain binding event in a noninvasive manner, such molecules are called biosensors.

1.2.4.3. Sensitive detection by hyper-CEST

Hyperpolarization increases the NMR signal of xenon by up to five orders of magnitude which allows for the *in vivo* MRI localization of dissolved xenon at low micromolar concentrations. Nevertheless, the direct NMR detection of xenon nanocarriers such as cryptophane-A is restricted due to the following reasons: Only a small fraction of the dissolved xenon is temporally entrapped by the cryptophane molecules. Therefore the NMR signal of xenon inside the host molecule is much smaller than the signal of free xenon in solution. Thus, the concentration of cryptophane molecules that is necessary to detect the NMR signal of entrapped xenon above the noise level is relatively high. Typically, micromolar CrA concentrations are necessary to observe a signal for xenon in cryptophane-A without substantial signal averaging (as an example see the spectrum in figure 1.9).

Although *in vitro* experiments are possible under such conditions (high concentrations of hp-xenon and cryptophane), an aspired *in vivo* translation aiming for the use of xenon nanocarriers as contrast agents would be dramatically hampered by the low concentration of dissolved xenon that is achievable *in vivo* (ca. 1 µM in human brain[68]). In addition, the sensitivity of xenon based contrast agents needs to be in the nanomolar range in order to meet the requirements of modern cell-labeling applications as introduced earlier.

The mentioned limitations for direct detection of the nanocarrier related xenon signal can be overcome by an indirect detection scheme that is based on chemical exchange saturation transfer (CEST). Rather than detecting the small signal of xenon entrapped by the nanocarrier, the abundant signal of xenon in solution is used as a sensing medium that reports on the presence of the xenon host. The magnetization of xenon inside the xenon host is therefore depolarized by a selective radiofrequency pulse of several seconds. This depolarization gets further transferred onto the magnetization of xenon in solution as a consequence of an ongoing chemical exchange between both spin ensembles as illustrated for cryptophane-A monoacid in figure 1.11, left. The combination of saturation transfer based signal amplification (CEST) in combination with hyperpolarized xenon is termed hyper-CEST.[69] The detection scheme allows enhancing the sensitivity for the detection of xenon hosts by up to seven orders of magnitude when compared to direct detection with thermally polarized xenon.[69] In addition, low micromolar hp-xenon concentrations that are realistic for *in vivo* applications, are sufficient to report on the presence of nanomolar xenon host concentrations.[70] The achievable sensitivity therefore fulfills the requirements for the detection of biological relevant targets in modern cell-labeling applications.[43]

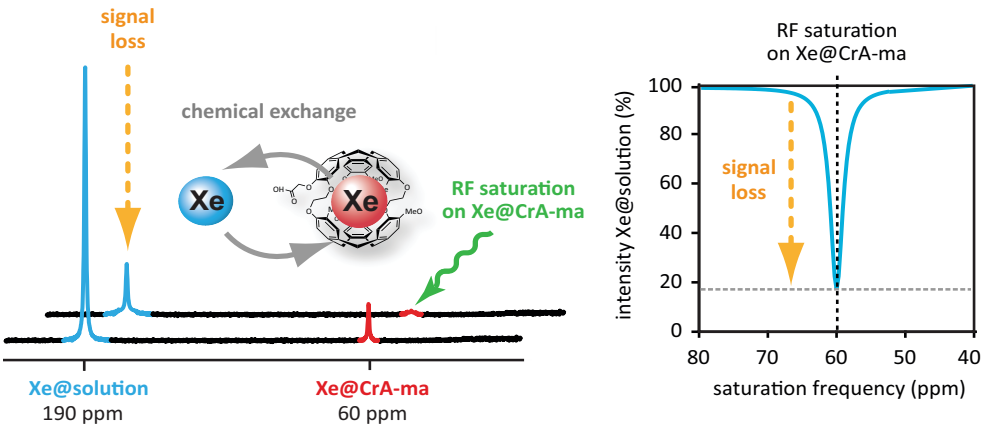

Figure 1.11: Sensitive detection of xenon nanocarriers by hyper-CEST detection illustrated for the xenon host cryptophane-A monoacid (CrA-ma). A schematic xenon NMR spectrum of CrA-ma (ca. 200 µM) dissolved within hp-xenon (2 % xenon, 25 % spin polarization) saturated water is shown. The NMR signal of xenon in solution (Xe@solution, shown in light blue) resonates at 190 ppm while the frequency of xenon entrapped within the cryptophane-cage resonates at 60 ppm (Xe@CrA-ma, shown in red). The magnetization of xenon within cryptophane-A monoacid is selective depolarized by a radiofrequency saturation pulse (green) centered on the frequency of Xe@CrA-ma. As a consequence of the permanent chemical exchange (exchange rate ca. 30 Hz) between hyperpolarized xenon in solution and depolarized xenon within the cage (indicated by grey arrows), the solution signal gets depleted (signal loss shown by yellow arrow) for a saturation pulse of several seconds. The intense solution signal therefore acts as a sensing medium for the presence of the low concentrated xenon nanocarrier by chemical exchange saturation transfer (hyper-CEST, left). The principle can be applied for spectroscopy while the xenon in solution signal is plotted as a function of the applied saturation frequency (right). Saturation at the resonance frequency of xenon entrapped within CrA-ma (RF saturation on Xe@CrA-ma) is indicated by a reduction of the detected solution signal according to saturation transfer.

The hyper-CEST scheme can be applied for NMR spectroscopy[70] resulting in hyper-CEST- or z-spectra. The intensity of xenon in solution is therefore plotted for varying saturation frequency offsets which allows specifying the resonance frequency of a certain xenon nanocarrier. Figure 1.11 (right) shows a schematic hyper-CEST spectrum of CrA-ma in solution. The resonance frequency of xenon in solution (at 190 ppm) is observed while the saturation frequency of the applied rf-pulse is stepwise varied along the typical cryptophane chemical shift range from 80 to 40 ppm. Prior to each individual saturation and acquisition step, fresh hp-xenon has to be delivered while the resolution of the spectrum depends on the saturation frequency step size. A typical hyper-CEST spectrum with a saturation frequency step size of 1 ppm therefore requires 40 individual measurements (from 80 to 40 ppm) each including hp-xenon redelivery followed by rf-saturation and signal acquisition. Other spectroscopic hyper-CEST techniques witch shared initial magnetization just need a single hp-xenon delivery step, while the frequency domain is covered by gradient encoding.[71] Nevertheless such fast hyper-CEST spectroscopy is limited to *in vitro* measurements since the sample needs to show a homogeneous geometry in at least one spatial dimension. The hyper-CEST scheme can be further combined with spatial encoding which allows for

the MRI localization of low concentrated xenon nanocarriers (10^{-8} M) as demonstrated for CrA-ma *in vitro*.[70] The principle of hyper-CEST MRI with CrA-ma as contrast agent is illustrated in figure 1.12.

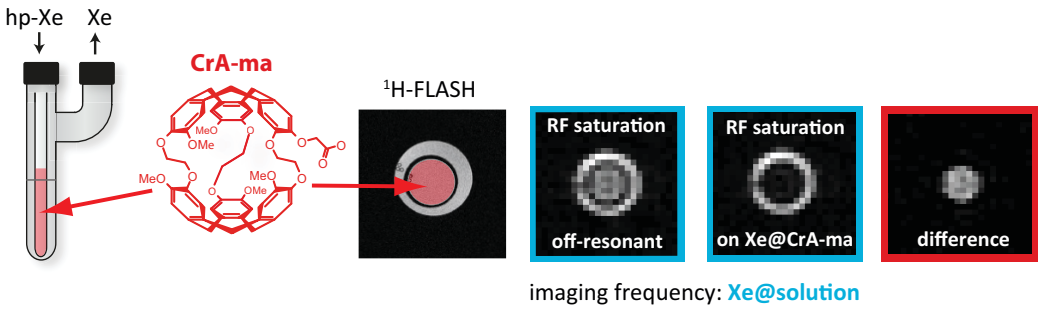

Figure 1.12: Principle of *in vitro* hyper-CEST MRI with cryptophane-A monoacid (CrA-ma) as a xenon based contrast agents. The depicted double compartment phantom (left) consists of a 5 mm NMR tube (inner compartment) that is inserted into a 10 mm NMR tube (outer compartment). Both compartments are filled with water. The inner compartment contains dissolved CrA-ma (shown in red). The sample solution is saturated with hp-xenon. A proton reference image (^{1}H-FLASH) shows a slice through the sample phantom while the localization of CrA-ma in the inner compartment is highlighted in red. The sensitive localization of CrA-ma is achieved within two subsequent hyper-CEST acquisitions. The first scan observes the unaffected distribution of xenon in solution (RF saturation: off-resonant) that is equally distributed within both compartments. In a second scan the saturation pulse is centered on the resonance frequency of xenon in CrA-ma (RF saturation: on Xe@CrA-ma). Due to saturation transfer, the solution signal is depleted within the inner compartment. The difference of both images reveals the localization of CrA-ma within the inner compartment.

The MRI localization of the xenon host needs two independent measurements. At first, a reference scan is necessary that detects the distribution of the sensing medium that is hp-xenon in solution. In a second scan a radiofrequency pulse is centered on the resonance frequency of the xenon host following xenon redelivery. According to the hyper-CEST principle, the signal of xenon in solution gets depleted at the localization of the xenon host by saturation transfer. The distribution of the xenon host is later calculated by subtracting the second image from the reference image followed by pixel wise normalization. In order to consider relaxation effects that occur during saturation, the reference scan has to be combined with a saturation pulse of equal length and pulse strength prior to acquisition. This saturation pulse is centered on a frequency different to the resonance of xenon inside the xenon host. The reference scan is therefore called off-resonant scan while the on-resonant scan (on the resonance of xenon inside the host) achieves CEST weighting. Both scans therefore consist of an initial xenon delivery step, followed by a saturation pulse (on-/off-resonant) and spatial encoded signal acquisition of xenon in solution at the end. In general it has been concluded, that a sufficient MRI contrast for xenon hosts such as cryptophanes is achievable, as soon as the provided concentration of hp-xenon is sufficient to enable xenon MR imaging. Although *in vivo* hyper-CEST detection of xenon nanocarriers has not been demonstrated so far, the requirement is given for lung or brain imaging as mentioned above.

1.3. MRI cell-labeling with xenon nanocarriers

1.3.1. Initial situation

To motivate the objectives of this thesis, this section summarizes achievements related to MRI cell-labeling with xenon nanocarriers at the time when corresponding parts of this study started. Further achievements within the field are discussed within the relevant results part as well as in the conclusion. At first, technical requirements related to *in vitro* xenon-MRI with live cells are described (delivery of hp-xenon) followed by an overview about initial cell-labeling experiments with xenon nanocarriers.

1.3.1.1. Delivery of hp-xenon for in vitro experiments

In vitro experiments with live cells are usually performed with aqueous buffered solutions to maintain the cell viability and to simulate physiologically relevant conditions. Since xenon is hyperpolarized in the gas-phase (see introduction) it has to be efficiently dissolved within the sample solution prior to the NMR measurement. The requirement for the dissolution method of choice is to maintain the xenon spin polarization, to keep the cellular integrity unaffected and to allow for hyper-CEST detection. Two conceptually different principles for the delivery of hp-xenon gas have been described:

In the first one, xenon is hyperpolarized and collected within a cold trap as ice followed by the transfer of a batch of concentrated hp-xenon into gas phase and into the sample phantom. Xenon hyperpolarization and dissolution are two separate procedures (Batch mode).
In the second one, xenon is continuously hyperpolarized and immediately transferred and dissolved within the sample solution (Continuous flow mode) allowing for redelivery throughout the measurement.

Xenon delivery in batch mode:

Hp-xenon gas is provided at high concentration on top of the sample solution within a gas-tight glass tube that has to be evacuated to avoid oxygen driven xenon spin relaxation. The gas is further dissolved within the test solution by gentle shaking followed by signal acquisition. Since hp-xenon gets depolarizes by the creation of transverse magnetization during signal acquisition, the sample phantom has to be removed from the spectrometer and shaken again to allow for new gas dissolution prior to a further acquisition. The number of possible acquisitions is restricted by the volume of the gas reservoir on top of the test solution as well as the xenon gas-phase T_1-relaxation. To compensate for these restrictions high xenon concentrations as well as polarization levels have to be achieved to create

sufficient signal at relatively low scan numbers. The hp-gas is therefore cryogenically extracted and concentrated within a cold-trap at the polarizer outlet. The "shaking method" was used within early studies that reports on the interactions of xenon with inorganic and organic molecules [64,67,72] as well as for initial cell experiments[64,73]. Nevertheless the use of xenon delivery in batch mode imposes restrictions for *in vitro* cell-labeling experiments due to the following limitations:

- A high experimental effort for signal averaging.
- A restricted comparability between measurements since the chemical shift of xenon is sensitive to pressure conditions.
- Cell damage due to sample evacuation and repetitive shaking.
- Limitations for conventional hyper-CEST spectroscopy and –imaging due to variable initial magnetization.

As a major aspect, hyper-CEST detection relies on multiple acquisitions with an identical initial xenon magnetization. A subsequent xenon redelivery with identical magnetization is hard to realize by the shaking approach. Therefore batch mode experiments have been restricted to direct xenon detection with xenon-host concentrations in the high µM range. Especially the development of cell-labeling approaches for molecular imaging applications requires very sensitive spectroscopic characterization of labeled cells to match physiological relevant target concentrations (nM). Therefore batch mode delivery of hp-xenon by shaking is rather unsuited for cell-labeling experiments with hyper-CEST detection.

Xenon delivery in continuous flow mode:

In contrast to batch mode experiments, hyperpolarized xenon can be continuously dissolved within the sample solution. The polarizer is therefore operated in a continuous flow mode which allows for redelivery of fresh hyperpolarized xenon after each acquisition step without the need to remove the sample from the spectrometer. The xenon flow through the polarizer as well as into the sample solution is triggered by gas flow controllers. This allows for stable polarization conditions within the optical pumping cell as well as reproducible initial xenon magnetization.[74] The method therefore allows for nearly unrestricted signal averaging as well as the performance of CEST-detection. Since the gas is not concentrated within a cold-trap after hyperpolarization, as it is typically the case for batch mode operation, the initial xenon fraction (2-5 % xenon) is comparable small after a single xenon delivery step. Nevertheless the possibility to do extensive signal averaging as well the ability to perform CEST-detection compensates for this.

Xenon delivery methods in continuous mode can be further classified with respect to the localization of the gas-liquid exchange devices that are used. The gas-liquid exchange is either located directly within

the NMR reading zone of the sample phantom (direct xenon delivery) or the gas-liquid exchange device and the sample phantom are spatially separated from each other (indirect xenon delivery).

Direct xenon delivery:

Very efficient gas dissolution within the reading zone of the sample phantom can be achieved via a bubble dispenser that consists of a set of multiple small fused silica glass capillaries arranged next to each other.[74] While this method shows good performance for aqueous solutions, it becomes problematic for cell suspensions due to foam formation. Although this could be prevented by the use of antifoam agents, it was assumed that bursting gas bubbles can create strong forces causing cell death and fragmentation of sensitive cell types.[75]

As an alternative, membrane bundles have been used for the continuous dissolution of hp-xenon into test solutions.[76] Since the gas diffuses through membrane pores, the method is minimal invasive and should allow for cell experiments without serious cell damage, although this was not proven. Nevertheless the membrane bundle occupies a relatively large volume within the sample phantom compared to the thin capillaries of a bubble dispenser. It therefore can be problematic to design sample phantoms that consists of two compartments, an important requirement to perform MRI experiments with labeled cells and control cells side by side.

Both described possibilities for continuous and direct dissolution of hp-xenon gas within the reading volume of the sample phantom are expected to be challenging for cell-labeling experiments either due to cell damage (bubble dispenser) or a relative large phantom occupancy (membrane bundles).

Indirect xenon delivery:

Alternative strategies have been described that rely on the continuous infusion of hp-xenon into flowing aqueous solutions. As a main difference to the previous mentioned direct dispersion method this allows for delocalization of the gas-liquid exchange process from the NMR reading volume. The aqueous solution gets first enriched with hyperpolarized xenon within a gas-liquid exchange device and is further transported to the sample located within the NMR reading zone. For gas-liquid exchange, commercially available membrane modules[77] or a bubble dispenser within an additional compartment (bubbling chamber[78]) upstream the sample phantom have been used. While the whole setup is operated under continuous flow of the xenon saturated solution, the sample has to be immobilized within the reading zone.

At the beginning of this study, xenon NMR cell-labeling experiments have been only performed by other laboratories using batch mode delivery of hp-xenon. As explained above, the method is limited for the development of labeling strategies that later requires hyper-CEST detection.

1.3.1.2. Cell-labeling applications

The capability of xenon to sense and report on its chemical environment has been described in various NMR studies ranging from material science[39,40] to experiments with biomolecules[41,42]. All studies capitalize strongly on signal enhancement due to laser induced hyperpolarization. Initial *in vivo* experiments with hp-xenon holds promise for biomedical applications such as void space lung imaging[48,49,79,80]. Further on, the delivery of dissolved hp-xenon to organs like the brain[51,52] has been demonstrated, motivating its use as a sensing medium *in vivo*. The interpretation of xenon signals within complex mixtures of biological samples is complicated due to various unspecific interactions. The information content of such experiments is therefore restricted.

This lack of specificity has been overcome by the use of xenon nanocarriers that are able to form inclusion complexes with xenon atoms via their transient entrapment. The nanocarriers are further characterized by a unique xenon chemical shift that can be related to a specific interaction via the functionalization of the xenon host. The xenon host is therefore conjugated to a targeting unit with specificity for a certain interaction partner.

Very sensitive detection of xenon nanocarriers based on hyper-CEST gave reason for the development of targeted xenon-hosts with the potential to detect disease-associated biomarkers at physiological relevant concentrations (nM).

The most prominent and best characterized xenon host systems are cryptophanes. The targeting concept offers a huge variability since any antibody or ligand can serve as an affinity tag to achieve biochemical specificity. Related ideas were also demonstrated for enzyme-specific or receptor-specific cryptophane conjugates detecting cancer markers[81–83] as well as for cryptophane conjugates revealing DNA hybridization[84] or MHC-antigen interactions[85]. The mentioned experiments were aiming for the design and spectroscopic characterization of targeted cryptophanes by proof of principle studies within test solutions of purified targets but not in cellular environments. Only a few papers related to cell-labeling with cryptophanes have been published prior to this work (but did not necessarily employ Xe MRI detection) and are briefly summarized as follows:

An initial study by Seward et al. (2008)[86] demonstrated enhanced cellular uptake of peptide-functionalized cryptophane molecules in normal and cancer cells. At first unspecific cell-labeling was achieved by coupling cryptophane to cationic cell penetrating peptides leading to enhanced cellular internalization. In addition, specific cell-labeling was demonstrated. To this end, cryptophane was coupled to an integrin specific RGD peptide leading to integrin receptor-mediated cryptophane uptake into cells. While pointing to moderate toxicity of the tested cryptophane-peptide conjugates, intracellular concentrations in the micromolar range have been reported. The study was focused on aspects related to the chemical synthesis of the tested conjugates as well as cell physiological characterizations of the labeling procedure without performing xenon NMR.

The first study that successfully demonstrated the use of cryptophanes for cell-labeling by performing xenon NMR was published by Boutin and coworkers in 2011[87]. The authors grafted cryptophane molecules on transferrin and detected the transferrin-receptor mediated cellular uptake of the cryptophane modified protein into cells. Xenon NMR spectra of labeled cells in solution acquired by batch mode delivery of hp-xenon revealed a characteristic spectroscopic signature for the cell internalized cryptophane conjugate.

The authors further performed cell-labeling experiments with cryptophane-decorated BSA serving as a marker for unspecific cellular uptake. The spectroscopic xenon signature within this labeling experiment was comparable to the signals observed for receptor mediated cell-labeling pointing to unspecific interactions of cryptophane with cellular membranes. In both cases the resonance frequency of the cell related cryptophane-conjugates was shifted by approximately 10 ppm downfield compared to the resonance frequency of cryptophane in aqueous solution. This characteristic frequency shift was first described by Meldrum et al. in 2010[88] and addressed to the embedding of cryptophane molecules into lipid membranes.

Nevertheless, MRI localization of labeled cells was not demonstrated since the cell-related NMR signals were too small. Spatial localization of such cell-related NMR signal would have required either extensive signal averaging or indirect detection based on saturation transfer (hyper-CEST). Both alternatives for MRI detection are hard to achieve in experiments with batch mode delivery of hp-xenon as already explained.

During this thesis another xenon host based on perfluorcarbon (PFC) nanodroplets was investigated as an alternative to cryptophanes.[89] Since the synthesis of supramolecular cryptophanes is time and cost intensive, xenon nanocarrier based on PFC nanodroplets can overcome this limitation. The nanodroplets are formulated out of linear perfluorooctylbromide (PFOB) molecules. Droplet formation is straight forward and can be achieved by high pressure homogenization resulting in emulsions of nanodroplets with uniform and controllable size. As a consequence of a high Ostwald solubility coefficient for xenon gas within PFOB (ca. 1.2 at 37 °C, about 10 times higher than Xe solubility in water) these nanodroplet emulsions have been successfully used for the *in vivo* delivery of dissolved hyperpolarized xenon by injection[90]. Based on this high solubility, a single PFOB droplet with a typical diameter of 200 nm can serve as a host for ca. 15000 xenon atoms, which is much more when compared to cryptophanes with a cavity size optimized to fit exactly one xenon atom. It was also demonstrated, that such nanodroplets can be detected by saturation transfer based xenon NMR spectroscopy. A recent study that has been performed within test solutions of PFOB nanodroplets of different sizes (160-310 nm) confirmed a superior hyper-CEST sensitivity for this xenon host in the sub-picomolar range.[89] The hyper-CEST sensitivity for such nanodroplets is therefore much higher when compared to cryptophanes that have been detected at nanomolar concentrations[70].

The idea to use PFC nanodroplets as hyper-CEST contrast agents strongly benefits from the fact that such nanodroplets are pre-clinically approved contrast agent in ultrasound imaging, computed tomography and ^{19}F-MRI applications.[91] Therefore, their cell-labeling properties are already evaluated in detail which could allow transferring these known clinical application routes to *in vivo* hyper-CEST MRI. In this context, the nanodroplets are favorable when compared to cryptophanes where the *in vivo* behavior is largely unknown so far. PFC nanodroplets have been successfully used within preclinical cell-tracking as well as molecular imaging applications using 19-Fluorine MRI.[92] In this context, three different labeling routes are established that are: (i) *ex vivo* labeling (ii) *in situ* labeling and (iii) *in vivo* labeling. These strategies allow for the following protocols:

(i) Efficient *ex vivo* labeling by cellular uptake of untargeted PFC nanodroplets could be demonstrated for a variety of different cell types. The labeled cells where further re-injected and tracked within animal models. Examples include cell types with huge relevance for immunotherapeutic applications and inflammation studies (dendritic cells, T-cells, stem-cells, lymphocytes) as well as cancer cells. Importantly, the PFC droplets have no negative effect on either the cellular viability or the cellular function. It could even be demonstrated that hematopoietic stem cells retain their pluripotency after PFC labeling. The mentioned publications are summarized by Ahrens and Zhong (2013)[93].

(ii) For *in situ* labeling untargeted PFC nanodroplets are directly injected into the blood stream. The droplets are then taken up by cells of the reticuloendothelial system. These labeled leukocytes (monocytes, macrophages) do further accumulate within regions of inflammation as a result of the normal inflammatory response. To this end, untargeted PFC nanodroplets can be used to indirectly localize inflammation hot spots. This capability has been used to study a variety of disease within mouse models such as: cancer development, multiple sclerosis, ischemia, pulmonary defects as well as organ transplant rejection. The mentioned publications are summarized by Ahrens and Zhong (2013)[93].

(iii) Targeted PFC nanodroplets have also been successfully used to demonstrate molecular imaging by MRI or ultrasound *in vitro* as well as *in vivo*. The technical requirements for such targeting approaches are similar for different perfluorcarbon based nanodroplet types. The hydrophobic perfluorcarbon droplets are therefore decorated with lipid monolayers that bear chemically modified head groups. The modification further allows for a covalent coupling of targeting units. Alternatively the lipid head groups are biotinylated followed by the binding of avidin-bound antibodies in a modular fashion.[94]
The first *in vivo* demonstration of molecular imaging with targeted PFC nanodroplets serving as an ultrasonic contrast agent was done by Lanza and coworkers in 1996.[94] Within this study arterial thrombi were created within dogs and then exposed to antifibrin antibodies that were pre-conjugated to avidin. In a second step biotinylated perfluorodichlorooctane (PFDCO) has been injected leading to nanodroplet binding at the region of thrombosis due to avidin-biotin interaction.

Another study demonstrated targeting of angiogenesis in tumors using integrin-targeted PFOB nanodroplets.[12] Target specificity was achieved by the covalent coupling of an integrin peptidomimetic antagonist to lipids surrounding the nanodroplets. Since integrin is highly expressed on activated neovascular endothelial cells, tumor angiogenesis could be detected by proton MRI. Relaxivity of the nanodroplets was achieved by incorporating lipophilic Gd-chelates into the surfactant commixture surrounding the PFOB core.
A comparable study used integrin-targeted PFOB nanodroplets in a glioblastoma mouse model.[95] The provided data were the first demonstration of the ability of ^{19}F-MRI to detect integrin endothelial expression in brain tumors *in vivo*. Also recently, the accumulation of a folate receptor (FR)-targeted PFCE (Perfluoro-15-crown-5-ether) nanoemulsion in FR-positive tumor sites has been demonstrated.[96] The study is of special interest since a detailed fluorescence based evaluation (microscopy, flow cytometry) of the binding specificity of folate conjugated nanodroplets was performed.

The described demonstrations of cell-tracking as well as molecular imaging with PFC nanodroplets paired with their superior hyper-CEST sensitivity (pM detection limit) motivated the initial characterization of PFOB for xenon based MRI cell-labeling.

1.3.2. Objectives of this study

The development and characterization of MRI cell-labeling approaches based on xenon nanocarriers was conceptual divided into three main objectives. Initially, a bioreactor for hyper-CEST MRI experiments with live cells had to be designed to overcome limitations of direct xenon bubbling (objective I). Following this, strategies for efficient cell-labeling with non-targeted xenon nanocarriers were developed to demonstrate sensitive MRI cell-tracking on live cells *in vitro* (objective II). Finally, *in vitro* molecular MRI with xenon hosts targeting different cell surface epitopes was performed on live cells (objective III).

Objective I: Characterization and optimization of hp-xenon delivery for cell experiments

Methods for the delivery of hp-xenon that have been used so far are restricted for their use in experiments with live cells as explained. Batch mode experiments do not allow for CEST-detection that is necessary for NMR/MRI experiments at desired low labeling concentrations.
An initial objective of this thesis was therefore the evaluation and optimization of methods that allow for the continuous delivery of hp-xenon to samples of live cells to enable sensitive hyper-CEST-detection. While direct bubble dispersion was assumed to be critical for the integrity of sensitive cell types, the method provides a high initial xenon magnetization due to efficient gas-liquid exchange

paired with a comparable low effort with respect to the experimental setup. Therefore, direct xenon delivery by bubble dispersion had to be evaluated in detail with respect to achievable xenon magnetization as well as cell viability.

In order to allow for extended cell experiments under more gentle conditions an alternative setup based on the indirect delivery of hp-xenon to cell samples had to be designed. The dissolution of hp-xenon was spatially separated from the actual sample compartment. Therefore different gas-liquid dissolution devices (hollow fibre membranes, bubbling chamber) were tested while relaxation effects were minimised.

Further on, a suitable sample compartment was designed that allows for immobilization of cell material to prevent sample wash out under continuous liquid flow (bioreactor). Different matrices for efficient immobilisation of cells under high density were tested. The bioreactor-setup was combined with appropriate sensors in order to control pH, temperature and dissolved oxygen while liquid flow and gas delivery was triggered via the NMR spectrometer.

Objective II: MRI cell-tracking with non-targeted xenon hosts

Although unspecific labeling has to be prevented in case of applications with targeted xenon hosts, it is a common labeling approach for preclinical cell-tracking applications. For this purpose cells are typically labeled *ex vivo.* The labeled cells are further injected into an organism of choice which allows studying there *in vivo* behavior. Nonspecific cellular uptake of xenon hosts was demonstrated for cryptophane-conjugates as well as for perfluorcarbon nanodroplets [86,93] but without demonstrating the localization of labeled cells by xenon MRI.

In case of cryptophane-conjugates the cellular uptake was related to the hydrophobicity of the cryptophane-molecule leading to membrane association followed by endocytosis. To capitalize on this property we aimed for unspecific cell-labeling with unmodified, i.e., strongly hydrophobic cryptophane-A monoacid (CrA). The initial objective was therefore to develop and characterize protocols for unspecific cell-labeling with CrA. The aim was to achieve sufficient intracellular concentrations of CrA in order to demonstrate hyper-CEST MRI localization of CrA-labeled cells *in vitro.*

Cell-tracking with PFOB-labeled cells is already preclinical approved for other imaging modalities. Existing cell-labeling protocols were adapted to achieve sufficient intracellular PFOB concentrations by unspecific labeling. Following this, it was tested if hyper-CEST MRI allows for the detection of cell internalized PFOB nanodroplets.

The hyper-CEST-NMR/MRI performance of both xenon hosts was analysed by using different pulse sequences as well as hyper-CEST parameters in order to generate optimal contrast between labelled and unlabelled cells. In addition, both xenon hosts were linked to fluorescence probes to verify the cellular localization as well as to quantify the labelling efficiency and MRI sensitivity.

Further studies were carried out to proof the multiplexing potential of CrA and PFOB labelled cells side by side. Both xenon-hosts are characterized by individual xenon signals. It had to be proven if hyper-

CEST detection allows for host selective MRI localisation in order to generate switchable contrast. All initial spectroscopic hyper-CEST experiments with labelled cells in suspension were carried out by using direct xenon delivery via bubble dispersion. Expected negative effects of this xenon delivery method concerning the cellular viability were neglected. Information from these initial experiments was further used to demonstrate MRI tracking of live cells within the developed bioreactor (objective I).

Objective III: Molecular MRI with targeted xenon hosts (biosensors)

Receptor-mediated cellular internalization of cryptophane conjugates was already described and monitored by xenon-NMR[86,87] but without demonstrating MRI detection of labeled cells. In addition, cryptophanes that are capable to specifically bind purified targets in solution had been developed.[82,85] The final objective of this thesis was therefore to demonstrate molecular MRI with xenon hosts targeted to cell surface epitopes of live cells within the developed bioreactor.
The optimization of the developed bioreactor setup (objective I) by MRI experiments with unspecific labeled cells (objective II) was an important prerequisite for this demonstration since: (i) unspecific cell-labeling is assumed to generate higher labeling rates and therefore stronger NMR signals when compared to specific labeling and (ii) the synthesis of targeted xenon hosts is time- and cost intensive and therefore rather unsuited for technical optimization purposes. Molecular MRI of live cells within the developed bioreactor setup was performed by using three different targeted cryptophane conjugates:

(i) A modular cryptophane biosensor targeting CD14
(ii) A scaffolded cryptophane biosensor targeting the EGF receptor (EGFR)
(iii) A cryptophane biosensor targeting metabolically labeled glycosylation patterns

The design, synthesis as well as the development of labeling protocols for the tested biosensors was performed by colleagues and coworkers and is not part of this thesis. Details can be found within relevant publications given within the corresponding sections.

2. Results and Discussion

2.1. Optimization of hp-xenon delivery for experiments with live cells

2.1.1. Direct xenon delivery by bubble dispersion

Efficient xenon delivery to cells within aqueous solutions could be achieved by using a spectrometer triggered bubble dispenser according to a setup introduced by Han et al. in 2005.[70] The bubble dispenser consists out of 5 silica capillaries connected to the outlet of the xenon polarizer. The silica capillaries were positioned within a custom made sample phantom housing the cell solution (illustrated as a schematic in figure 2.1a). Defined gas flow rates could be achieved by using spectrometer triggered gas flow controllers connected to a gas outlet port at a sidearm of the sample phantom. Details about the used setup for direct xenon delivery can be found within the materials part of this thesis. The formation of foam as a result of direct xenon bubbling into cell solutions was a serious limitation within initial experiments. This foam formation could be suppressed by the addition of an antifoaming agent (0.02-0.1 % pluronic L81, M.Ramirez ENC 2013, USA) allowing for constant flow of hp-xenon for ca. 15 sec followed by a bubble collapse delay of ca. 3 sec prior to the NMR signal acquisition. The used antifoam agent had no effect on the achieved xenon signal intensity as proofed by titration experiments (data not shown).

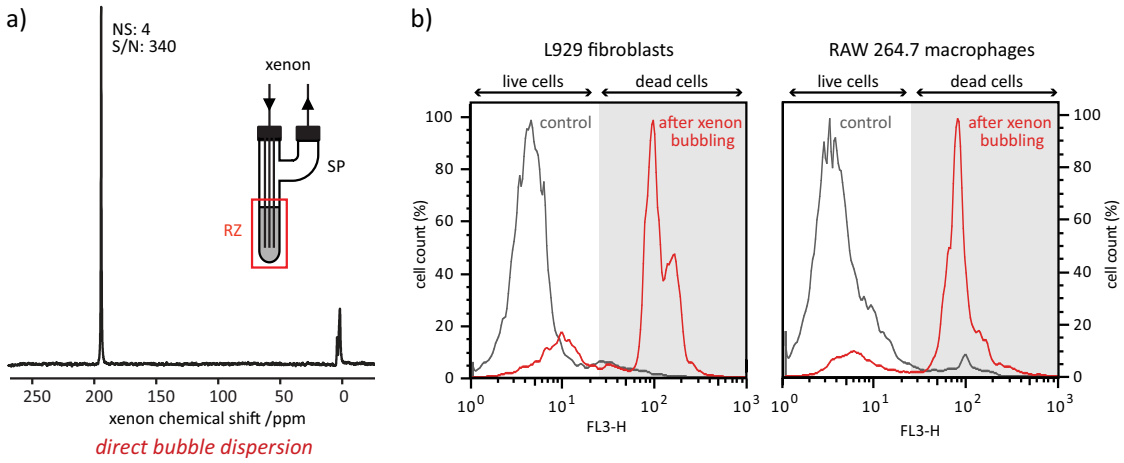

Figure 2.1: (a) NMR spectrum of dissolved hp-xenon (signal at 192 ppm) within a solution of L929 fibroblasts (10 million cells/mL). Gas delivery into the sample phantom (SP) was achieved by using a spectrometer triggered bubble dispenser that is shown as a schematic. The NMR reading zone (RZ) includes a small gas volume of hp-xenon (signal at 0 ppm) on top of the cell solution for spectral referencing. NS: number of scans, S/N: signal to noise. b) The effect of direct xenon delivery on the cellular viability was analyzed by flow cytometry. L929 fibroblasts as well as RAW 264.7 macrophages were tested before (control: grey line) and after 50 xenon delivery steps, each including 10 sec of constant gas bubbling (red line).

The efficiency of xenon delivery to cells in solution at medium density (10 to 30 million cells/mL) was probed by NMR spectroscopy. A representative xenon spectrum (10 million cells/mL, average of 4 scans) is depicted in figure 2.1a. The sharp and intensive peak (signal to noise: 340) from xenon in solution at ca. 192 ppm indicates very efficient dissolution for this gas delivery method. The spectrum was referenced to the signal of xenon in gas phase (to peaks close to each other, at 0 ppm) that comes from remaining gas bubbles within the sample solution as well as xenon gas entrapped within the interior of the bubble dispenser capillaries. Cell densities up to 30 million cells/mL result in spectra of comparable quality without considerable loss of the dissolved xenon signal.
Nevertheless the measurement of hyper-CEST spectra typically requires several xenon redelivery steps to observe saturation transfer effects for varying saturation frequencies.[70] Assuming a hyper-CEST spectrum that covers the relevant xenon chemical shift range from 0 to 250 ppm in 5 ppm steps, 50 xenon redelivery steps are necessary. With an individual bubbling time of ca. 10 sec per single delivery step, this sums up to 500 sec of constant gas bubbling into the cell solution.

To verify the effect of this bubbling procedure on the cell viability, two different cell lines (fibroblasts: L929, macrophages: RAW 264.7, both used later on for cell-labeling studies) were tested by performing viability tests after xenon delivery at the mentioned bubbling conditions. Cell viability was analyzed by flow cytometry, detecting the internalization of a fluorescence dye (7-Aminoactinomycin D). Cell death leads to increased membrane permeability, followed by an uptake of the dye correlated to enhanced fluorescence intensity (flow cytometry was done by Dr. Honor May Rose). After a typical hyper-CEST experiment (50 xenon redeliveries, each with: 10 sec bubbling, 3 sec delay, 10 sec rf-saturation) ca. 80 % of the analyzed cells were found to be dead (figure 2.1b). Cell death is a consequence of bursting gas bubbles that creates strong forces.

Within a recent study, comparable experiments aiming for the characterization of direct xenon delivery to cells in solutions has been presented.[75] The authors used a setup for xenon hyperpolarization and xenon dissolution comparable to the one used within this thesis. They achieved substantial lower xenon signal intensities (signal to noise: 12) within cell solutions of high density (100 million phage labeled cells/mL) most likely as a consequence of T_1 shortening. Such low initial signal intensities for dissolved xenon can lead to baseline instabilities within hyper-CEST spectra making their interpretation more complicated. Cell experiments therefore should be performed at medium cell densities (up to 30 million cells/mL) to avoid such problems, while the possibility to detect labeled cells by hyper-CEST detection is not substantially affected as shown later on. The study also includes viability assessment (done in a comparable way to the experiments shown here) of cells (MDA-MB-231 and Jurkat) that have been bubbled with hp-xenon for up to 140 min (10 sec gas bubbling followed by 10 sec waiting time). The data shows that the viability of certain cell types (such as Jurkat cells) is not affected by the bubbling procedure while MDA-MB-231 cells keeps 80 % viability up to 60 min. This shows that the viability of cells also strongly depends on the studied cell type.

The shown data therefore underline expected restrictions for *in vitro* cell experiments with direct xenon bubbling as well as the need for optimized delivery strategies for prolonged hyper-CEST experiments with sensitive cell types. Nevertheless the shown xenon delivery method is comparable simple and allows achieving high amounts of dissolved hp-xenon within test solutions at medium cell density (up to 30 million cells/mL). It is therefore suitable to evaluate and optimize initial cell-labeling experiments with the aim to detect cell associated xenon hosts while neglecting the cellular integrity as it will be demonstrated later on.

2.1.2. Indirect xenon delivery by perfusion

The need for alternative xenon delivery strategies enabling the demonstration of MRI labeling application with live cells motivated the design of a setup for indirect xenon delivery based on the perfusion of immobilized cells. The development of this setup started with the evaluation of suitable gas exchange devices as well as cell-immobilization strategies and matrices. Following this the individual components have been combined in a NMR compatible bioreactor that allows for long term xenon hyper-CEST experiments with live cells.

2.1.2.1. Evaluation of gas exchange devices

Two gas-liquid exchange devices, a bubbling chamber (figure 2.2a) and a membrane module (figure 2.2 b) have been tested for their potential to continuously dissolve gaseous hp-xenon within flowing aqueous solutions. As illustrated in figure 2.2, the flowing liquid gets enriched with hp-xenon gas within a compartment spatially separated from the MR reading zone.

The bubbling chamber was custom made out of Teflon according to a design adopted from Ref. [78]. The used membrane module (1 x 5.5 MiniModule®) has been purchased from Membrana GmbH (Germany). The signal intensity for dissolved xenon at 192 ppm achieved by using the bubbling chamber device (4 scans, signal to noise: 240) was much higher (factor of 170) when compared to the membrane module (32 scans, signal to noise: 4).

The low signal intensity achieved by the membrane module can be related to relaxation effects at the gas-liquid membrane interface or an inefficient gas-liquid exchange in general. Within a study by Cleveland and coworkers in 2009 a comparable hydrophobic polymer membrane has been used for the dissolution of hp-xenon into flowing aqueous solutions.[77] Although experimental conditions such as xenon spin polarization (10-15 %, here 25 %), geometry of membrane module, NMR/MRI setup were different, the signal to noise achieved for low concentrated xenon (1 %, here 2 %) was comparable (13.5 with 312 scans, here 4 with 32 scans). Nevertheless signal averaging, as it would be necessary for this

gas exchange device, is unsuited for desired hyper-CEST spectroscopy. In this case, the number of scans for each individual xenon delivery step has to be multiplied with the number of saturation frequency offsets requiring very long measurement times.

The signal of dissolved xenon achieved by the bubbling chamber device (4 scans, signal to noise: 240) showed comparable intensity as achieved with direct xenon delivery by bubble dispersion (4 scans, signal to noise: 340, see figure 2.1). The bubbling chamber device therefore allows for a very efficient dissolution of hp-xenon within flowing aqueous solutions as well as a continuous transport of dissolved xenon into the MR reading zone without substantial xenon depolarization.

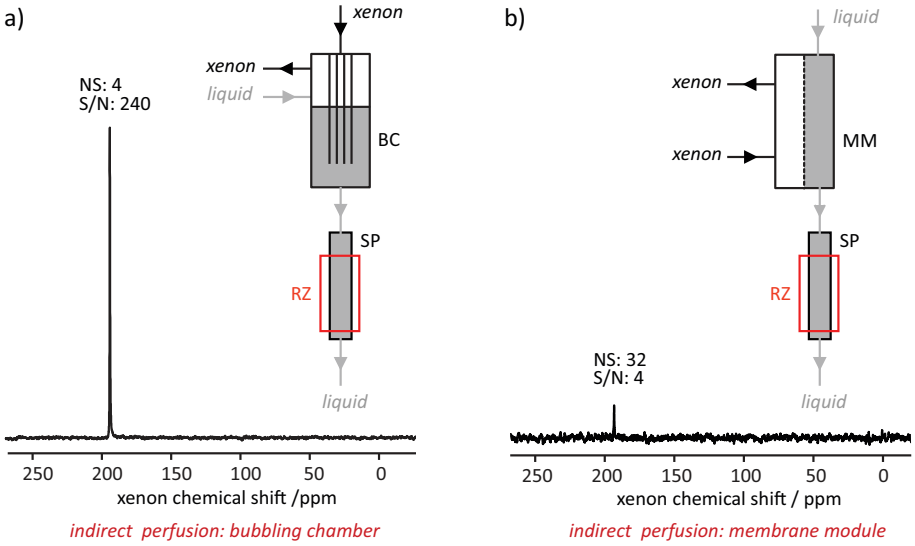

Figure 2.2: Comparison of indirect perfusion systems for the continuous delivery of hp-xenon into flowing aqueous solutions. A bubbling chamber device (a) was compared to a membrane module (b). The efficiency of xenon delivery correlates to the signal intensity of dissolved xenon (at 192 ppm) within the corresponding NMR spectra. The individual perfusion systems are shown as a schematic on top of the corresponding NMR spectra (BC: bubbling chamber, MM: membrane module, SP: sample phantom, RZ: reading zone, NS: number of scans, S/N: signal to noise). For both devises the sample phantom has been perfused at a liquid flow rate of 10 mL/min while the gas flow was set to 0.3 SLM.

2.1.2.2. Evaluation of matrices for cell immobilization

The indirect delivery of hp-xenon into the sample phantom by flowing aqueous solutions requires an immobilization of the cell material within the MR reading zone. This immobilization is necessary to prevents cell wash out during the measurement. The main requirement for the immobilization strategy was the achievement of a high cell density throughout the whole reading volume paired with an undisturbed liquid flow. Therefore cell immobilization matrices suitable for perfusion within a packed bed have been evaluated.

Bead shaped materials are good options because they combine high surface to volume ratios with preferable packing properties. Bead shaped matrices that allowed for cell attachment either at their outer surface (dextran beads: Cytodex 1, GE healthcare and glass beads: VitraPOR, ROBU GmBH) or their inner surface (collagen sponges: Atelocollagen Honeycomb sponge, Cosmobio Co) has been tested. Efficient cell immobilization could be achieved for all of these surface matrices as evaluated by microscopy (see figure 2.3). Nevertheless, their application within a perfused packed bed was limited due to unwanted cell detachment under desired flow rates (10 mL/min), clogging of the outlet filter under operation pressure (3.5 bar) and complicated handling.

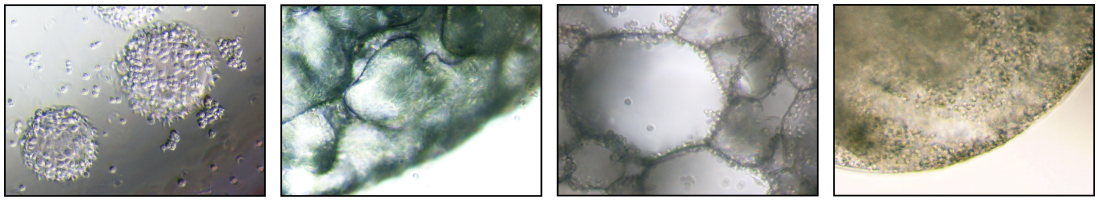

Figure 2.3: Representative overview of tested immobilization matrices. Cell immobilization by surface attachment (dextran beads, glass beads, collagen sponges) or encapsulation (alginate beads) was optimized and confirmed by bright field microscopy.

More suitable immobilization could be achieved by cell encapsulation within solid alginate beads (figure 2.3, right). The encapsulated cells are protected against shear forces that are created by flowing media. The beads can further be easily transferred into the MRI setup after cell culture and cell-labeling. In addition, the encapsulation procedure allows adopting cell density, bead size, bead stiffness as well as alginate diffusion properties for the specific needs of perfusion within a packed bed in combination with the delivery of dissolved hp-xenon. Therefore, cell encapsulation within alginate beads has been optimized and characterized in detail.

2.1.2.3. Characterization of alginate encapsulation

Cell encapsulation was done within a custom-made alginate droplet generator.[97] Details about the optimized encapsulation procedure can be found within the methods part. Bead properties, showing good performance for perfusion within a packed bed bioreactor, were found to be: a diameter of 1 mm, a density of 5000 to 10000 cells per bead (10 to 20 million cells/mL alginate) and a final alginate content of 1 %.

The visualization and characterization of encapsulated cells was enabled by confocal laser scanning microscopy (LSM 510, Carl Zeiss Microimaging GmbH, Jena, Germany) in combination with fluorescence live/dead cell staining using a commercial kit according to the manufactures protocol (PromoCell GmbH, Heidelberg, Germany). Live/dead cell staining utilizes two fluorescent dyes, Calcein-AM and Ethidium homodimer III (EthD-III). Calcein-AM penetrates the cell membrane of living cells and gets hydrolyzed to cell membrane-impermeable, green-fluorescent Calcein (emission maximum at 515 nm). EthD-III only passes through membranes of dead cells and intercalates with DNA (red fluorescence, emission maximum at 620 nm). The produced beads had a uniform size (diameter of ca. 1 mm) and showed a homogeneous distribution of live cells (figure 2.4).

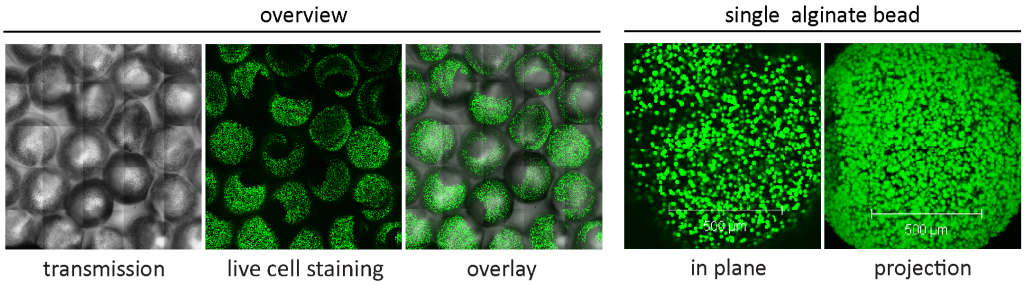

Figure 2.4: Microscopic characterization of solid alginate beads bearing encapsulated cells (L929 fibroblasts). Live cells have been stained with Calcein-AM (green fluorescence) to verify the encapsulation procedure. Shown is an overview image of multiple beads (left) as well as an image of a single bead (right).

The long term viability of L929 fibroblasts encapsulated in alginate beads was proved within a test setup prior to the development of a comparable setup for xenon MRI. A custom made sample phantom was therefore packed with alginate encapsulated cells followed by pump driven continuous perfusion (10 mL/min) with cell culture medium (DMEM) for 24 h at 37 °C. The perfusion system was placed within a standard CO_2 incubator to maintain cell culture conditions. The experiment revealed excellent long term viability for alginate encapsulated cells within a perfused packed bed with around 90 % live cells after 24 h incubation (5 % cell death related to encapsulation). Viability values has been calculated by counting the number of live and dead cells (ImageJ) in single plane fluorescence images of individual alginate beads after encapsulation and after perfusion for 24 h as shown in figure 2.5.

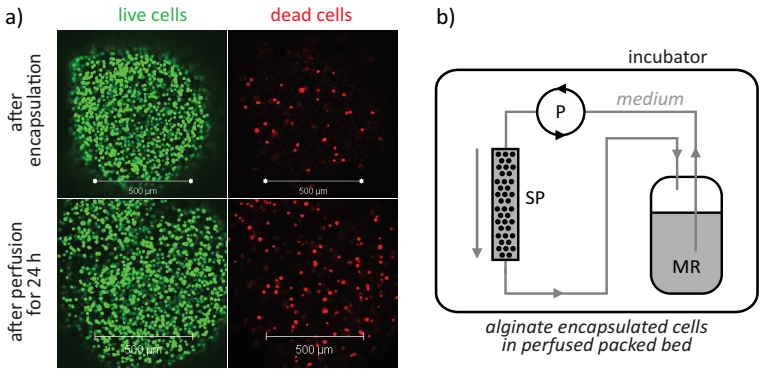

Figure 2.5: Evaluation of the long term viability of alginate encapsulated cells within a continuously perfused packed bed bioreactor. a) Cells were costained with Calcein-AM (green fluorescence) to visualize live cells and Ethidium homodimer III (red fluorescence) to visualize dead cells. Shown are single plane images of representative alginate beads taken after cell encapsulation and after perfusion for 24 h. b) The bioreactor test-setup is shown as a schematic (P: pump, SP: sample phantom, MR: media reservoir).

2.1.2.4. Development of a bioreactor-setup for xenon MRI

Following a successful optimization of the individual bioreactor components, including a bubbling chamber for gas-liquid exchange as well as a sample phantom for perfusion of encapsulated cells, a NMR/MRI compatible bioreactor setup was assembled and tested.

The bioreactor setup was equipped with mass flow controllers, temperature regulators as well as sensors for dissolved oxygen and pH. Spectrometer triggering of all mass flow controllers allowed for regulation of the xenon flow rate into the bubbling chamber as well as the liquid flow rate through the sample phantom in order to optimize xenon delivery to the alginate immobilized cells. More details about individual components of the bioreactor setup can be found within the materials part.

^{1}H-MRI allowed visualizing the individual cell-loaded alginate beads and shows the conducted splitting of the sample phantom in two compartments (figure 2.6). This phantom splitting along the direction of the media flow is an important requirement since cell-labeling studies needs to be done by comparing labeled and unlabeled cells within a single imaging experiment.

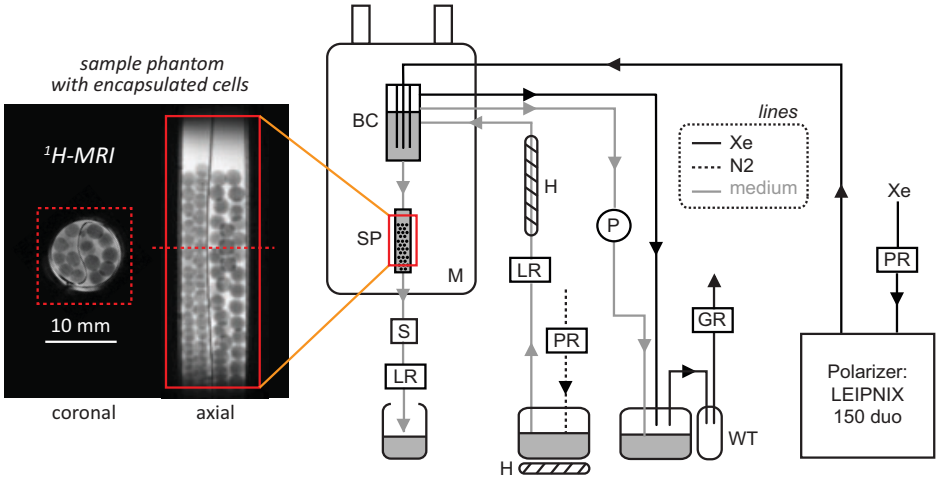

Figure 2.6: Schematic of the custom-made NMR compatible bioreactor setup for xenon NMR/MRI experiments with live cells (BC: bubbling chamber, SP: sample phantom, M: NMR spectrometer, H: heating jacked, P: pump, WT: water trap, S: pH/oxygen sensor, LR: liquid flow regulator, GR: gas flow regulator, PR: pressure regulator). The NMR reading zone is highlighted by a red square and covers the sample phantom bearing alginate encapsulated cells. The sample phantom is divided into two compartments as it is can be seen within the corresponding proton MR-image.

Efficient xenon diffusion into the beads was confirmed by xenon NMR spectroscopy at 37 °C showing a characteristic peak of dissolved xenon in alginate (192.1 ppm) close to the solution peak (191.9 ppm). MRI detection of both xenon solution signals (integrated around 192 ppm) confirmed an equal distribution over the whole sample phantom as shown by the overlay of a ^{1}H- and a ^{129}Xe-MR image (figure 2.7). In addition, the achieved signal intensity and distribution was constant over repeated measurements (data not shown) satisfying the needs for hyper-CEST experiments.

The developed bioreactor setup allows performing long term hyper-CEST MRI experiments without impairing the viability of tested cells as it will be demonstrated later on. Nevertheless, the experimental effort is relatively high when compared to experiments that rely on direct xenon delivery by bubble dispersion. Therefore, initial xenon experiments aiming for the development and optimization of MRI cell-labeling strategies have been performed by direct bubble dispersion accepting a certain percentage of cell death. The bioreactor setup was used later on to verify these optimized MRI cell-labeling approaches under live cell conditions.

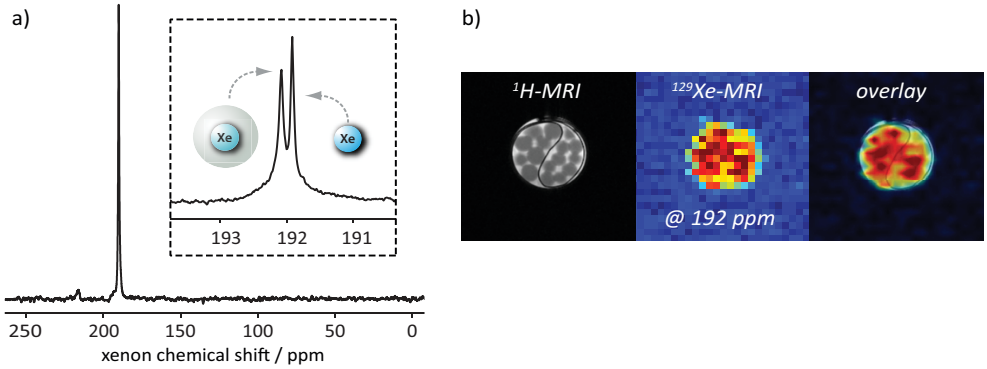

Figure 2.7: Verification of the xenon delivery efficiency within the perfused bioreactor setup loaded with alginate encapsulated cells. (a) The xenon NMR spectrum (4 scans) shows two intense signals for dissolved xenon as magnified within the dotted box (signal region: from 194 ppm to 190 ppm). The left peak corresponds to dissolved xenon within alginate while the right one comes from dissolved xenon in solution as indicated by schematics. (b) Spatial distribution of dissolved xenon (4 scans) along the sample phantom. ^{1}H- and ^{129}Xe-MR images are shown separated and as an overlay. The shown spectroscopic and imaging data has been recorded at 37 °C under optimized bioreactor working conditions.

The shown spectroscopic and imaging (figure 2.7) data has been measured at optimized bioreactor working conditions that can be found in detail within the materials part. In brief, the following conditions were used:

- Perfusion medium: Hanks balanced salt solution/HBSS (H1641, Sigma Aldrich, Taufkirchen, Germany)
  Note: It is important to use a medium that contains a low calcium ion concentration such as HBSS (1.3 mM $CaCl_2$) to avoid de-gelling of the perfused alginate beads (calcium ions are necessary for alginate matrix formation).

- Bubbling chamber: continuous media perfusion with 10 mL/min
  continuous bubbling of hp-xenon (5 %) with 0.4 SLM
  pump rate at overflow: 10 mL/min

- Sample phantom: media perfusion with 7.5 mL/min for 60 sec per scan

2.2. MRI cell-tracking with non-targeted xenon nanocarriers

2.2.1. MRI cell-tracking with Cryptophane-A (CrA)

Cell-tracking applications typically rely on unspecific *ex vivo* cell-labeling strategies using non-targeted versions of a contrast agent. The labeled cells are further injected into appropriate animal models followed by *in vivo* imaging. The applied labeling approaches are optimized to achieve high amounts of cell internalized contrast agents without impairing the viability of the labeled cells.
Initial experiments aiming for an *in vitro* demonstration of MRI cell-tracking with cryptophane based contrast agents therefore focused on the optimization of such unspecific cell-labeling strategies.

2.2.1.1. Cellular internalization and toxicity of CrA

The development and characterization of contrast agents for MR imaging applications requires measures to obtain information about their cellular uptake behavior as well their cellular localization. Fluorescence based techniques (microscopy, flow cytometry) are well suited for this purpose. The MRI contrast agent is therefore coupled to a fluorescence dye resulting in a dual mode imaging probe. For this reason, cryptophane-A monoacid (CrA-ma) was covalently coupled to a fluorescein-unit (FAM) via a three unit PEG-linker resulting in a bimodal conjugate (CrA-FAM) with improved water solubility. The chemical structure of CrA-FAM is shown in figure 2.9a. Chemically synthesis of CrA-FAM was performed by Federica Rosella and Dr. Jabadurai Jayapaul (see methods).
At the beginning, L929 fibroblasts were coincubated with CrA-FAM (75 µM) at different incubation times to validate the unspecific cell-labeling potential of cryptophane. Laser scanning microscopy revealed a localization of CrA-FAM within the cytosol of labeled cells while membrane embedding could be excluded. Maximal cell-labeling was achieved after 20 h incubation at 37 °C (see figure 2.8).
Cellular uptake was active since CrA-FAM internalization could be blocked by lowering the temperature to 4 °C. This observation was in line with previous reports were the internalization of cryptophanes-peptide conjugates was assumed to be due to fluid phase pinocytosis resulting in a cryptophane accumulation within cytosolic vesicles.[87] Interestingly, no uptake could be observed for cells incubated with a conjugate that consists out of the PEG-linker and fluorescein (FAM-PEG) without the cryptophane unit (CrA-ma). This observation underlines the main contribution of CrA-ma to the cellular internalization of CrA-FAM. Unmodified CrA-ma is strongly hydrophobic and has therefore a high tendency for cell association followed by uptake. Therefore a comparable cellular localization of CrA-ma and CrA-FAM was assumed, although this could not be ultimately proven.

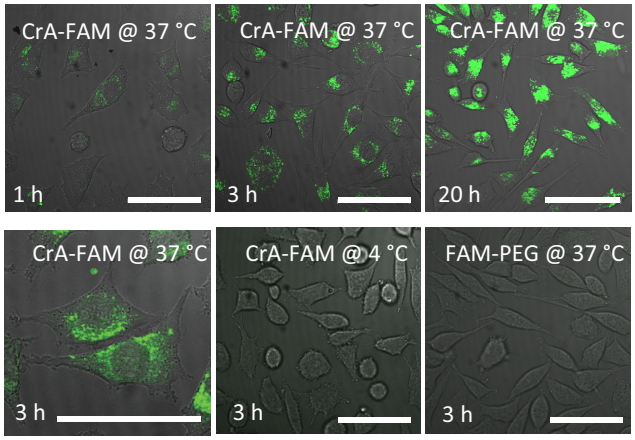

Figure 2.8: Fluorescence microscopy of L929 fibroblasts labeled with 75 µM CrA-FAM or FAM-PEG (green fluorescence). The effect of incubation time (top row), temperature (bottom row) as well as the molecular composition of CrA-FAM (bottom row) onto the cellular uptake has been studied. Incubation conditions including the used compound, incubation temperature as well as incubation time are indicated within the individual images. The length of the white bar represents 50 µm. Figure from Klippel et al. 2014.[98]

After demonstrating the cell-labeling potential of CrA-FAM, the toxicity of CrA-ma and CrA-FAM was tested for 20 h cell-labeling (maximal uptake as shown on top) at increasing concentrations (see figure 2.9b) by using the alamarBlue® cell viability assay. For CrA-FAM only a small viability reduction (down to 80 %) could be observed over the studied concentration range (0 to 100 µM). In comparison, unmodified CrA-ma showed a higher toxicity as indicated by a viability reduction down to 60 % at labeling concentration exceeding 50 µM for L929 fibroblasts (figure 2.9b). The coupling of fluorescein to cryptophane reduces the hydrophobicity of the molecule. Therefore the uptake efficiency is reduced (demonstrated later on) which underlines the reduced toxicity of CrA-FAM compared to CrA-ma. The viability threshold for cell-labeling was set to 80 %. Therefore, the optimal labeling conditions were found to be incubation with 50 µM CrA-FAM/CrA-ma for 20 h at 37 °C.

Further on, L929 fibroblasts were labeled with CrA-FAM under these optimized labeling conditions to quantify the achievable intracellular contrast agent concentration. Experiments have been performed with lysates of labeled cells followed by fluorescence quantification. The intracellular CrA-FAM concentration was estimated to be ca. 15 µM (see methods).

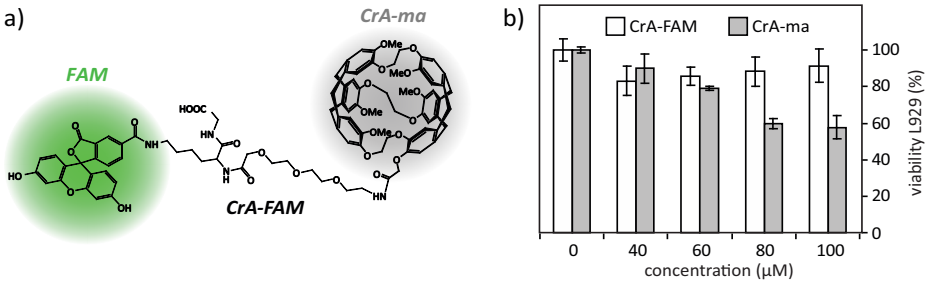

Figure 2.9: a) Chemical structure of a fluorescein (FAM) conjugated cryptophane-A (CrA-ma) molecule resulting in a bimodal contrast agent (CrA-FAM) for combined fluorescence and MR imaging applications. b) Compound toxicity was studied by incubating L929 fibroblasts with increasing concentrations (0 to 100 µM) of either unmodified CrA-ma or CrA-FAM for 20 h followed by cell viability assessment. Figure from Klippel et al. 2014.[98]

Within an independent study performed by Dr. Honor Rose and Federica Rossella, cell type dependence of CrA-FAM uptake has been studied by comparing toxicity and cell uptake for RAW 264.7 macrophages and L929 fibroblasts next to each other (figure 2.10). The cellular uptake for increasing CrA-FAM concentrations was quantified by measuring the fluorescence intensity in lysates of labeled cells. The intracellular concentration of CrA-FAM increases linear with the incubation concentration while the uptake into macrophages is more efficient. Toxicity values are comparable for both tested cell lines as analyzed by using the alamarBlue® cell viability assay.[99]

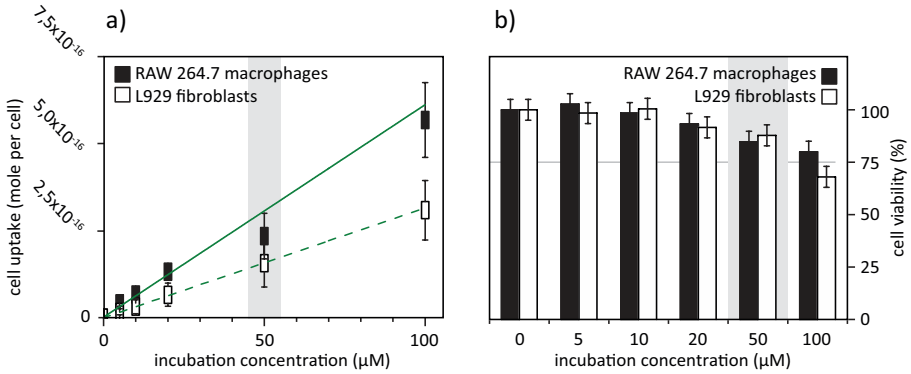

Figure 2.10: Cell uptake quantification (a) and cell viability assessment (b) at increasing CrA-FAM concentrations (0 to 100 µM) following incubation for 20 h at 37 °C. Macrophages (black) and fibroblasts (white) were analyzed in parallel to study cell type influence. The optimal labeling concentration (50 µM) is highlighted by grey boxes while the used viability threshold (here 75 %) is indicated by a grey line. Figure adapted from Ref. [99].

2.2.2.2. Spectroscopic hyper-CEST signature of CrA-labeled cells

Non-specific cell-labeling with cryptophane-A molecules has been demonstrated within the previous section. Following this, it had to be proven that the hyper-CEST principle enables the MRI localization of cryptophane labeled cells. Hyper-CEST MRI detection of cryptophane labeled cells requires a detailed spectroscopic characterization to verify the resonance frequency of xenon within the cell internalized xenon host.

Initial spectroscopic NMR experiments with CrA-ma labeled fibroblast (labeling with 90 µM CrA-ma for 3 h, labeling conditions were not optimized by this time) in solution has been carried out by using direct bubble dispersion due to the low experimental effort (compared to experiments within the bioreactor) of this xenon delivery method. Prior to the NMR measurement, free CrA-ma (100 µM) was added to the solution of labeled cells acting as a reference next to cell internalized CrA-ma (see figure 2.11). The reference signal of free CrA-ma in solution could be detected by direct spectroscopy with notable signal averaging (64 scans) at the typical xenon resonance frequency of ca. 60 ppm. Nevertheless, an additional signal within the cryptophane chemical shift range (ca. 90 to 40 ppm) coming from xenon entrapped in cell internalized CrA-ma could not be observed by direct NMR detection.

The xenon chemical shift range from 300 ppm to 5 ppm was further analyzed by hyper-CEST spectroscopy at a sampling rate of 5 ppm for the applied saturation frequency offsets (cw-saturation for 8 sec with 6.5 µT). Two asymmetric CEST-peaks could be observed centered around 200 ppm and 75 ppm (see figure 2.11c, top). Both peaks could be further resolved into 4 different CEST peaks by reducing the sampling rate to 1 ppm and by reducing the saturation pulse power (cw-saturation for 8 sec with 2.1 µT, see figure 2.11c, bottom). The observed peaks correspond to the following xenon spin pools:

- at 195 ppm: dissolved xenon within cells
- at 192 ppm: xenon in solution (direct saturation)
- at 69 ppm: xenon in cell internalized CrA-ma
- at 58 ppm: xenon in unbound CrA-ma (reference)

Cellular internalization of CrA-ma could be monitored by an 11 ppm xenon chemical shift change into the spectral downfield region at 22°C. The result illustrates the benefits of hyper-CEST for detecting cell internalized cryptophanes when compared to conventional detection.

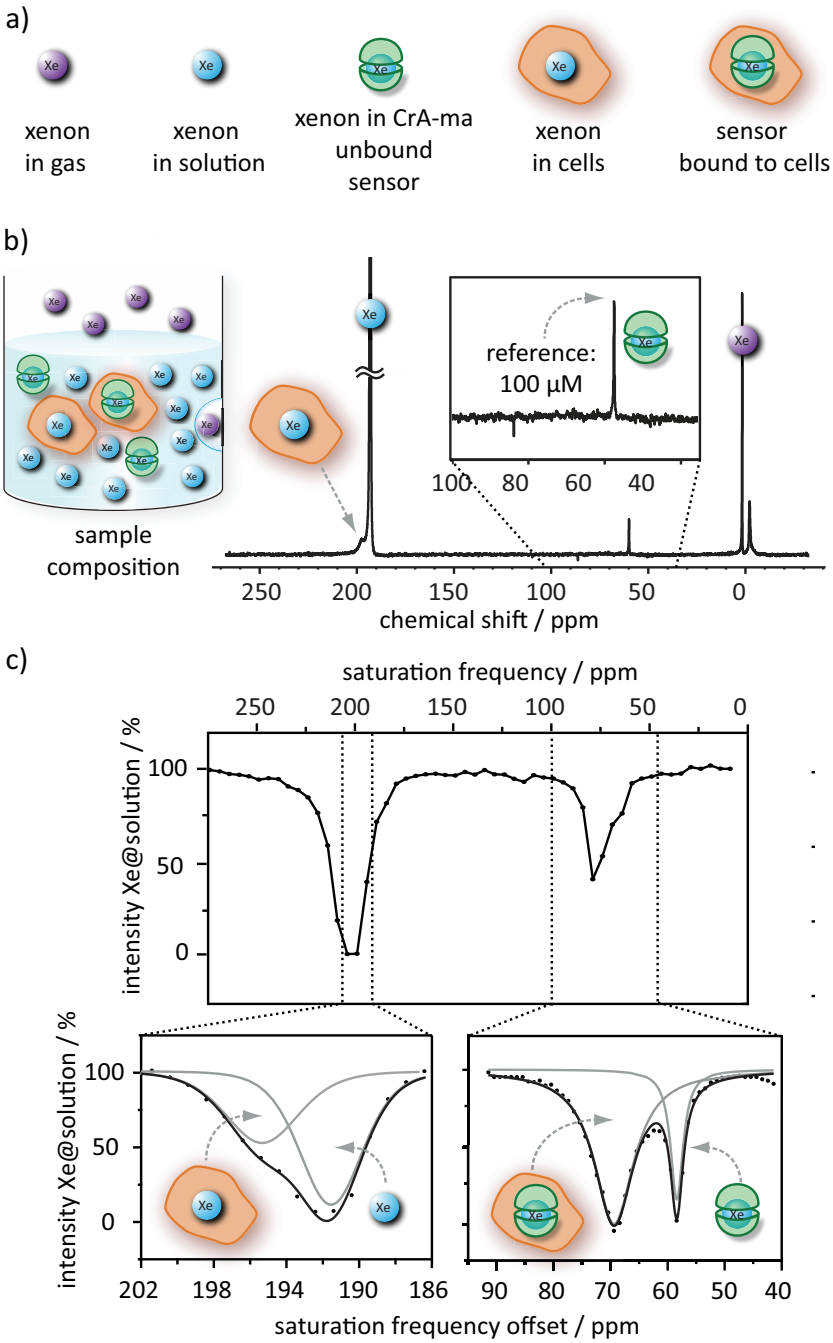

Figure 2.11: Spectroscopic NMR signature of cryptophane (CrA-ma) labeled L929 cells (15 million cells/mL) in solution analyzed by conventional detection and hyper-CEST detection in comparison. a) Schematic of detected xenon pools. b) Sample composition (left) and direct xenon NMR spectrum as an average of 64 scans. The cryptophane chemical shift range (40 to 100 ppm) is enlarged to illustrate the lack of a cell related cryptophane signal next to the intense reference signal of unbound cryptophane in solution at 58 ppm. c) Hyper-CEST spectroscopy allows the sensitive detection of the cell related cryptophane signal at a resonance frequency of 69 ppm. The experiment demonstrates the potential of the hyper-CEST technique to detect low concentrations of cell bound cryptophane molecules. Exponential Lorentzian fits are shown as grey lines, and the corresponding sums are shown as black lines. Figure from Klippel et al. 2014.[98]

The reference signal of xenon within unbound cryptophane (100 µM) was observed by direct detection while the signal of cryptophane in cells was invisible due to a much lower concentration. On the other hand, both unbound and intracellular cryptophane was detected by hyper-CEST with a saturation transfer intensity of 100 % for both spin pools although their concentrations were markedly different. This indicates higher hyper-CEST sensitivity for cell internalized cryptophane compared to free cryptophane in aqueous solutions. Cell or lipid association of cryptophane enhances the chemical exchanges of xenon atoms between the solution and the host molecule. This enhanced chemical exchange increases the saturation transfer effect that is beneficial for hyper-CEST detection.

The shown measurement (figure 2.11) was done at 22°C with a comparable high labeling concentration of CrA-ma (90 µM). Viability studies however revealed considerable toxic effects for CrA-ma exceeding labeling concentrations of 50 µM (see previous section). Therefore a spectroscopic hyper-CEST characterization of CrA-ma labeled fibroblasts was done under physiologically relevant temperature (37 °C) as well as nontoxic labeling conditions (labeling with 30 µM CrA-ma for 2 h, see figure 2.12). These considerations are important since the resonance frequencies of xenon as well as the hyper-CEST effect are both temperature dependent.[100]

In this experiment, the signal of cell internalized CrA-ma was detected at 71 ppm by a hyper-CEST effect of around 75 % (figure 2.12b). Compared to the previous experiment (figure 2.11) the signal was temperature shifted (by 2 ppm) as expected. Surprisingly, once again a signal for unbound CrA-ma in solution was detected at 61 ppm for the solution of labeled cells, although no additional CrA-ma has been added for referencing as it was done in the previous experiment. After centrifugation (3 min, 1000 g) the supernatant of the cell sample was measured again (figure 2.12c). This time the cell related signal at 71 ppm decreased while the peak at 61 ppm is comparable in intensity.

This observation underlines that the peak at 61 ppm corresponds to cell-released CrA-ma in solution rather than to a second cell-associated cryptophane signal. The small chemical shift of unbound CrA-ma for the incubation medium (which contains 1 % DMSO to dissolve the solid cage substance, figure 2.12a) compared to unbound CrA-ma in cell suspension (medium without DMSO, figure 2.12b-d) is due to DMSO leading to a characteristic downfield shift.[70] The remaining peak at 71 ppm in figure 2.12c for the supernatant after centrifugation is most likely due to cell fragmentation caused by bursting gas bubbles since cellular debris carrying CrA-ma could not be completely separated by this simple centrifugation. This interpretation is confirmed by measuring the supernatant of a second cell sample labeled and prepared identically but not measured in the NMR spectrometer (figure 2d, f). Here, centrifugation allows a complete removal of all labeled cell material as illustrated by the absence of the cell related cryptophane signal at 71 ppm.

At physiological temperature cell association of CrA-ma therefore leads to a clear downfield shift of ca. 9 ppm that is in agreement with results for biomembrane[101] or lipid interactions[88]. The centrifugation

experiments further revealed that cell fragmentation occurs as a consequence of direct xenon delivery by bubble dispersion. This observation further motivated the need of a perfused bioreactor setup for experiments with live cells.

Although direct xenon delivery by bubble dispersion causes cell death and fragmentation, the method is suitable to characterize the resonance frequency of cell associated CrA-ma by hyper-CEST detection. It further allows evaluating the efficiency of a certain cell-labeling scheme by using the intensity of the cell related hyper-CEST signal as a marker for the labeling efficiency.

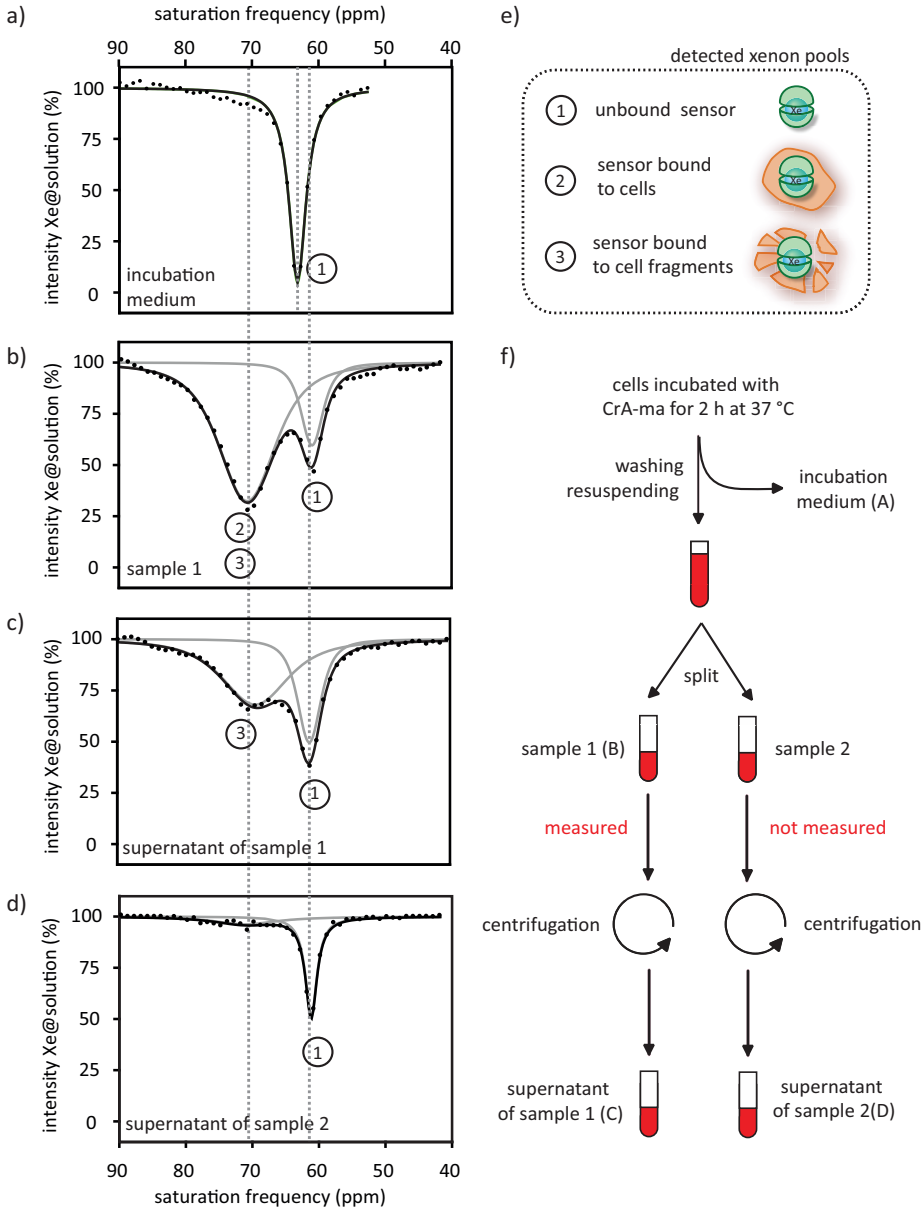

Figure 2.12: Hyper-CEST spectra of cryptophane (CrA-ma) labeled L929 cells (10 million cells/mL) at physiological temperature (37°C) and observation of cell fragmentation due to xenon bubbling. All spectra were measured with an 8 sec saturation pulse with an amplitude of 6.5 µT and a frequency interval of 1 ppm. Exponential Lorentzian fits are shown as grey lines while the corresponding sums are displayed as black lines. a) Incubation medium with 1 % DMSO and 30 µM CrA-ma. b) CrA-ma labeled cells (sample 1) after washing and resuspending. c) Supernatant of sample 1 after centrifugation. d) Supernatant of a second sample prepared under same conditions but not measured before. The detected xenon pools (e) and the experimental procedure (f) are shown as a schematic. Figure and figure caption from Klippel et al. 2014 [98].

2.2.1.3. Selective MRI localization of CrA-labeled cells

The spectral characteristics of cryptophane-A labeled cells have been studied in detail as shown within the previous section. Next to this, the frequency selectivity of hyper-CEST based MRI localization of cryptophane labeled cells was proven.
A two compartment phantom was prepared by inserting a 5 mm NMR tube into a 10 mm NMR tube. Both compartments were filled with 200 µM CrA-ma dissolved in cell culture medium (1 % DMSO). One hour prior to the NMR measurement, the outer compartment was loaded with mouse L929 fibroblasts (15 million cells/mL) to achieve cell association for CrA-ma. For this initial experiment comparable high CrA-ma concentrations have been used since viability studies where not performed to this time.

A series of MR-images detecting the signal of xenon in solution (192 ppm) was recorded (figure 2.13b). A saturation pulse (3 sec, amplitude: 5 µT) with varied frequency offsets (54-77 ppm, 1 ppm frequency interval) was applied before each individual image acquisition to obtain CEST weighting. The signal intensity within the images was analyzed for both compartments individually and plotted over the corresponding saturation frequency offset resulting in a spatial encoded hyper-CEST spectrum (figure 2.13a).
Within the outer compartment a cell related CrA-signal was detected at the characteristic frequency of 70 ppm. At the same saturation frequency no CEST-effect was observed within the inner compartment. The effect can be also observed within the MR-image series. Saturation at 61 ppm causes a saturation transfer effect within both compartments since unbound CrA-ma is present within both of them. Saturation at 70 ppm only depolarizes the xenon signal within the outer compartment where cells are present. The cell localization could be further verified by calculating the difference image from the average of 32 off-resonant images (saturation at 310 ppm) and the average of 32 on-resonant images (saturation at 70 ppm, see figure 2.13c). The data illustrates that hyper-CEST MRI allows for a selective localization of cell associated CrA-ma even in the presence of unbound CrA-ma provided weak saturation pulses can be used as it is the case within test solutions.

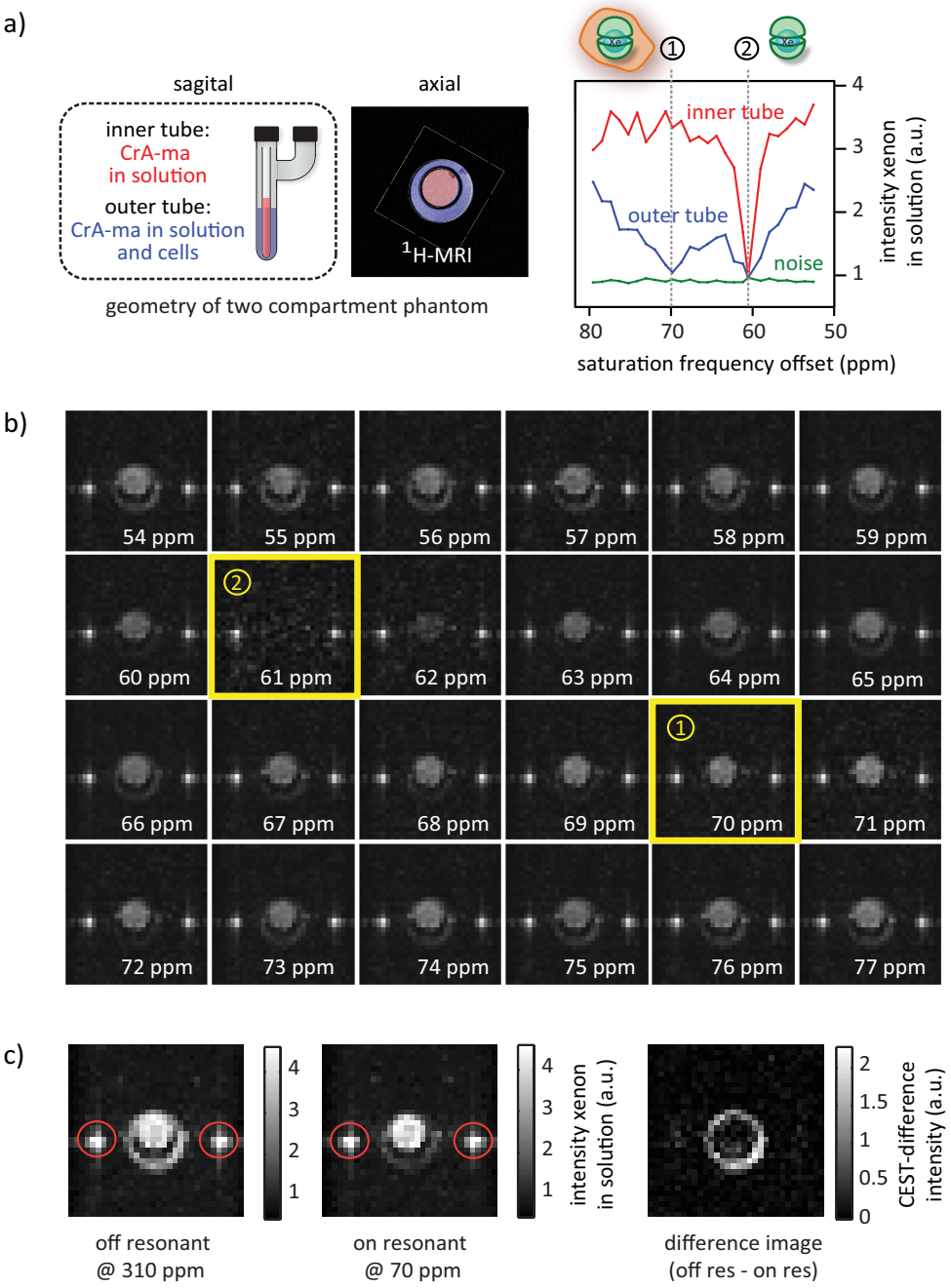

Figure 2.13: Hyper-CEST-MRI of cells resuspended in a CrA-ma solution (200 µM). Measurements were done by direct xenon bubbling at 37 °C. a) Schematic of phantom geometry and hyper-CEST spectrum acquired by spatially encoded read out for the inner and outer tubing separately. Saturation was applied for 3 sec and 5 µT pulse amplitude using saturation frequency steps of 1 ppm. The direct saturation frequencies for xenon in cell associated CrA-ma (1) and free CrA-ma (2) are marked by grey dotted lines. b) EPI scans measured for varying saturation frequencies according to the hyper-CEST spectra. c) Hyper-CEST image showing the average of 32 on-resonant (on Xe@CrA-ma bound to cells: 70 ppm, middle) and 32 off-resonant (310 ppm, left) EPI scans. Localization of cell-associated CrA-ma is given by the difference image (right). Image artifacts are labeled by red circles (artifacts are canceled out in the difference image). Figure caption adapted from Klippel et al. 2014.[98]

Following cell-labeling experiments with unmodified CrA-ma comparable measurements characterizing the hyper-CEST properties of CrA-FAM labeled cells were performed. This is important since the use of the dual mode CrA-FAM construct allows a direct correlation of MRI data to fluorescence microscopy as well as fluorescence based quantification of the achieved labeling efficiency (see previous part).

The hyper-CEST signature of CrA-FAM labeled fibroblasts (labeling with 100 µM CrA-FAM for 3 h, labeling conditions were not optimized at this time) was comparable to the signature obtained by CrA-ma labeling. The CEST-response off cell internalized CrA-FAM was centered at a saturation frequency offset of 71 ppm, while the signal for unbound CrA-FAM was detected at 62 ppm (see figure 2.14a). Hyper-CEST MRI experiments aiming for spatial localization of labeled cells were successful as illustrated by the detection of labeled L929 fibroblasts within the outer compartment of a two compartment phantom (see figure 2.14b). Spillover correction was applied to avoid signal contributions of unbound cryptophane to the hyper-CEST contrast observed for cell internalized CrA-FAM.

Such a correction is important especially at higher saturation pulse strengths (cw-saturation with ca. 10 to 30 µT) that cause an overlap of CEST peaks that are close to each other (chemical shift difference of 10 ppm and less). The off-resonant pulse was therefore placed by mirroring the frequency position of cell internalized CrA-FAM to that of unbound CrA-FAM in solution (see figure 2.14b). By doing so, only the CEST effect for cell internalized CrA-FAM contributes to the calculated contrast within the final difference image (off-resonant minus on-resonant).

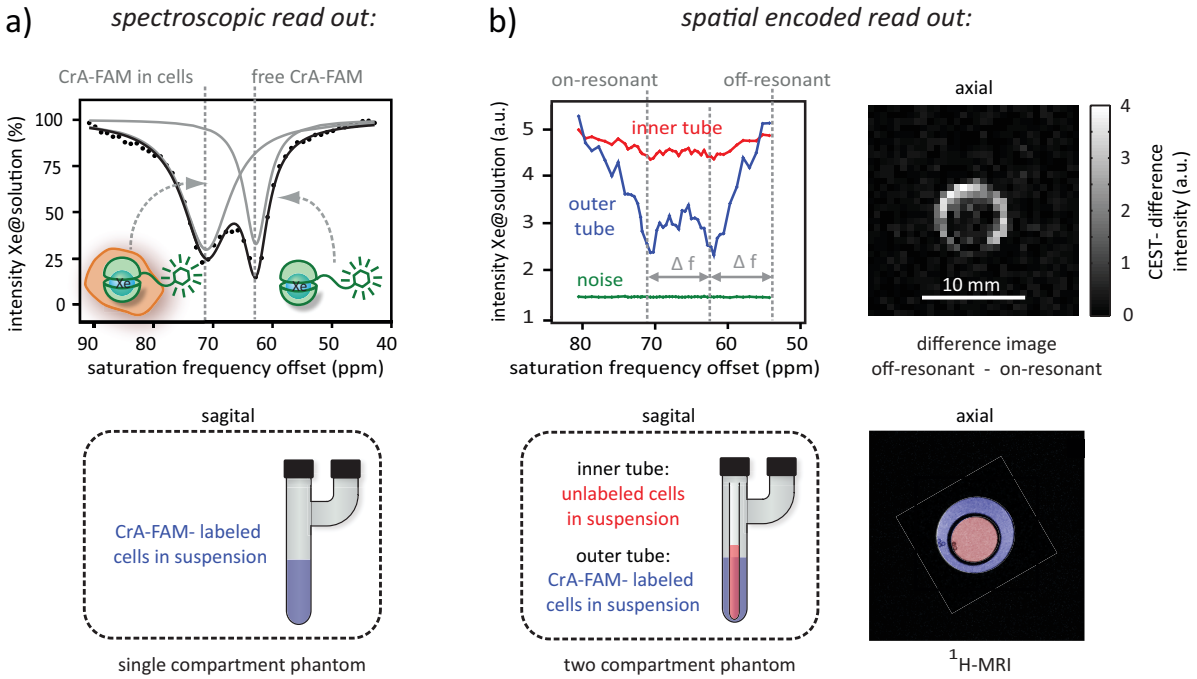

Figure 2.14: Hyper-CEST response of CrA-FAM labeled cells (15 million cells/mL) observed by unlocalized spectroscopy and spatially encoded read out. a) CEST-spectra acquired by spectroscopic read out using a 12 sec saturation pulse of 6.5 µT and 1 ppm frequency interval. Experimental data are represented by black dots. Exponential Lorentzian fits are shown as grey line while the corresponding sums are displayed as a black line. The saturation frequencies for free CrA-FAM and cell internalized CrA-FAM are marked by grey dotted lines. Detected xenon pools and the phantom geometry are shown by schematics. b) CEST-spectra acquired by spatially encoded read out for the inner and outer tube separately. On- and off-resonant saturation frequencies for localization of internalized CrA-FAM are marked by grey dotted lines. Spillover correction is indicated by grey arrows: the off-resonant pulse was placed by mirroring the frequency position of Xe@CrA-FAM in cells to that of free Xe@free CrA-FAM. Saturation was applied for 10 sec with 7 µT using 0.5 ppm saturation frequency steps. A hyper-CEST image (axial cross section through the phantom) shows the averaged difference of 32 on-resonant and 32 off-resonant EPI-scans. The phantom geometry is shown by a schematic as well as a representative axial proton MR-image. The compartments were colored using graphic design software for visualization. The outer compartment was filled with CrA-FAM labeled cells (colored in blue) while cells within the inner compartment were unlabeled (colored in red). Figure and figure caption from Klippel et al. 2014[98].

2.2.1.4. Live-cell-tracking of CrA-labeled cells

The MRI properties of the dual mode fluorescein-cryptophane conjugate (CrA-FAM) have been probed within the developed bioreactor setup on live cells (fibroblasts L929). Unspecific cell-labeling aiming for high intracellular CrA-FAM concentrations was done according to previous optimized incubation conditions (50 µM CrA-FAM, 20 hours, 37 °C). An intracellular CrA-FAM concentration of ca. 15 µM was achieved under these conditions as it was estimated by fluorescence based quantification experiments with cell lysates. Labeled cells and unlabeled cells (control) were further encapsulated within alginate beads (10 million cells/mL) and placed in separated compartments within the perfused bioreactor setup (figure 2.15a).

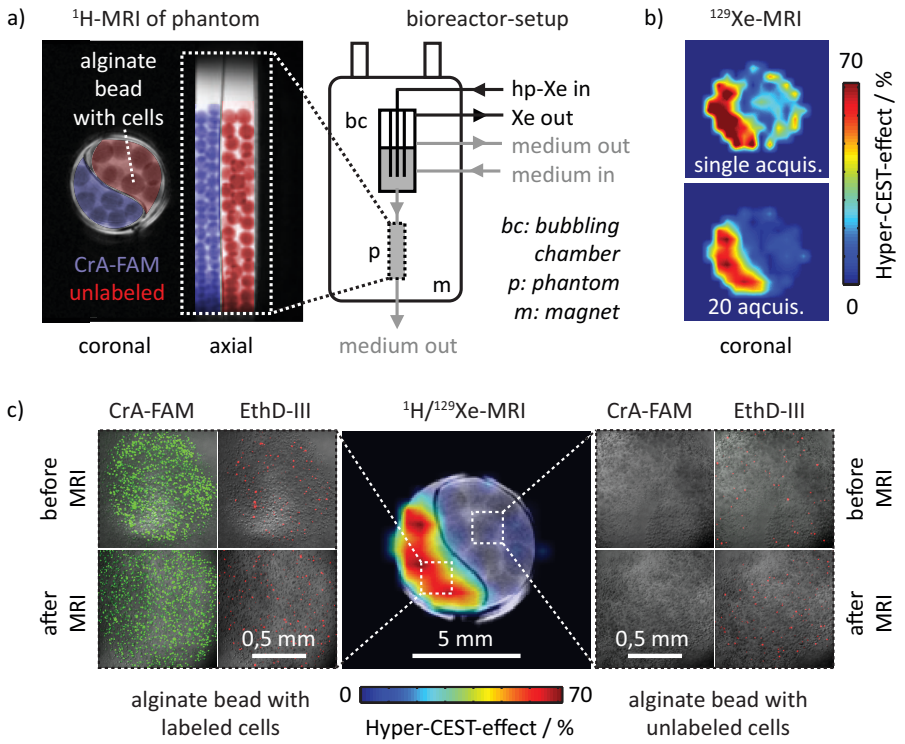

Figure 2.15: *In vitro* live cell-tracking of cryptophane (CrA-FAM) labeled cells (intracellular concentration=15 µM) analyzed within a perfused bioreactor. a) Proton-MRI of a two compartment phantom housing cells encapsulated within alginate beads. The compartments were colored using graphic design software for visualization. One compartment is filled with CrA-FAM labeled cells (blue), whereas cells within the second compartment are unlabeled (red). The sample phantom is perfused with hp-xenon saturated medium. bc=bubbling chamber, m=magnet, p=phantom. b) The localization of the compartment bearing ca. two million labeled cells could be achieved in a single CEST-acquisition (2 min) at the expense of a higher noise level compared to the accumulation of 20 CEST-acquisitions. c) Hyper-CEST-effect as a result of 20 on-resonant/off-resonant RARE-images clearly reveals the localization of labeled cells (center). Laser scanning microscopy (optical section of single alginate beads) done before and after MRI shows CrA-FAM (green) accumulation within encapsulated cells. Dead cells are stained with Ethidium homodimer III (red). Live cells in the control compartment do not give a contrast in either MRI or fluorescence scan. Figure and figure caption from Klippel et al. 2014.[98]

The MRI localization of ca. 2 million CrA-FAM labeled cells could be achieved within a single hyper-CEST acquisition (ca. 2 min) at the expense of a higher noise level compared to the accumulation of 20 CEST-acquisitions (figure 2.15b). The used hyper-CEST parameters were: cw-saturation for 12 sec with 18 µT. The MRI data were complemented with fluorescence microscopic analysis to verify that the observed xenon-MRI contrast of ca. 70 % is indeed correlated to the localization of CrA-FAM labeled cells. In addition staining for dead cells with fluorescence dye EthD-III reveals, that the cellular viability is only affected marginally (ca. 90 % live cells after measurement) by the developed indirect xenon delivery procedure. Viability values were calculated by counting the number of live and dead cells (ImageJ) in single plane fluorescence images of individual alginate beads after encapsulation and after the MRI measurements. Figure 2.16 shows MRI raw data for the performed cell-tracking experiment as well as details for image post processing that was performed using MATLAB (R2012a, MathWorks, Natick, MA). Details about MR imaging, bioreactor settings and hyperpolarization conditions are listed within the materials section.

The experiment demonstrated for the first time the potential of cryptophane to act as a highly sensitive MRI contrast agent that allows for live cell-tracking based on saturation transfer.

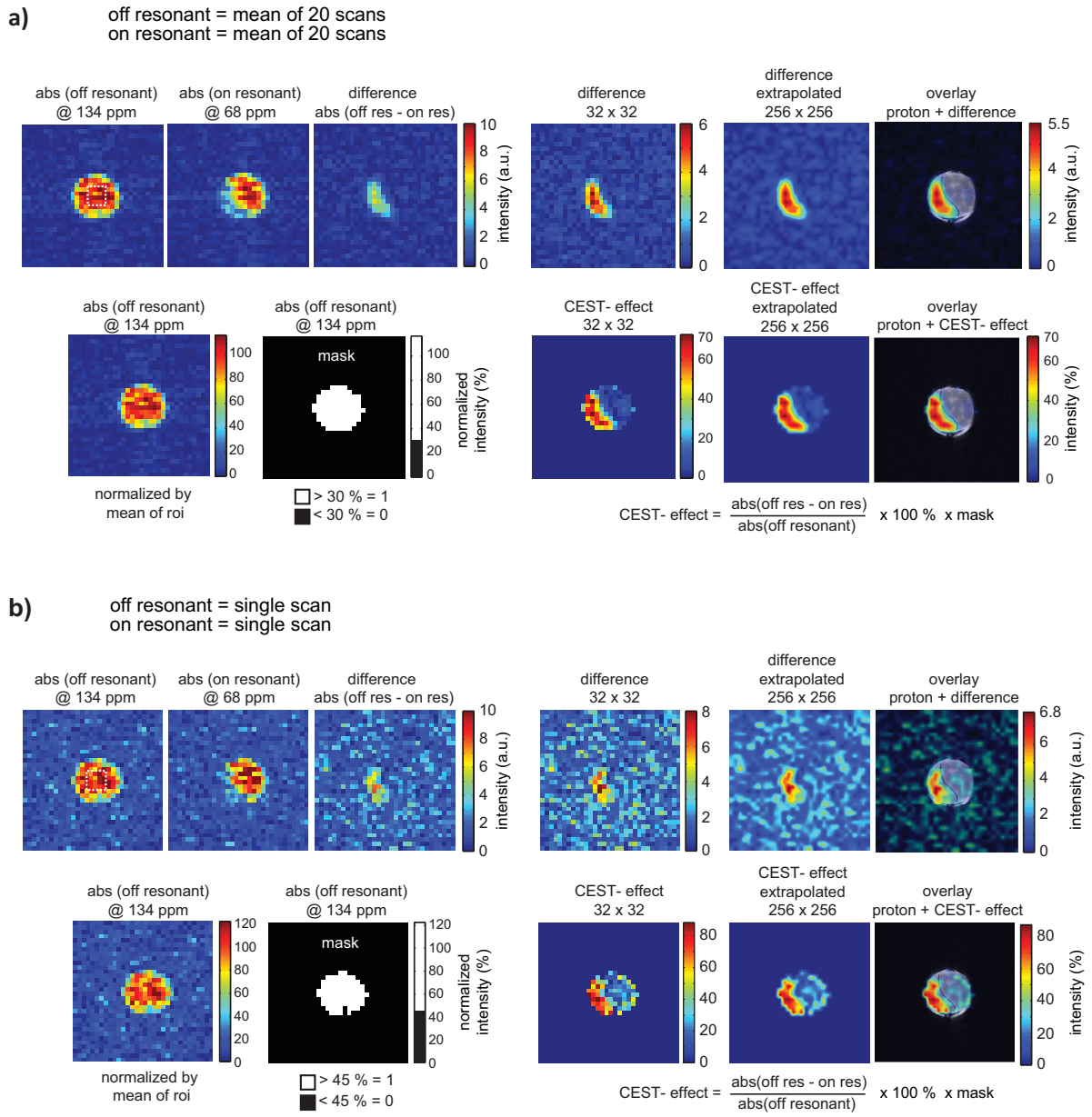

Figure 2.16: Post-processing of hyper-CEST images for: *In vitro* live cell-tracking of cryptophane (CrA-FAM) labeled cells within a perfused bioreactor (see figure 2.15). a) Top row from left to right: The average of 20 magnitude-images detecting xenon in solution is shown for off-resonant saturation (irradiating at 134 ppm) and on-resonant saturation (irradiating at 68 ppm, at the resonance of cell internalized CrA-FAM). The difference image (32 x 32 image matrix) was interpolated to a 256 x 256 image matrix and overlaid with the respective proton image. Bottom row from left to right: The CEST-effect was further evaluated by calculating the percentage reduction of single pixel intensities due to on-resonant saturation. This allows an analysis independent from slightly different xenon delivery throughout the sample phantom. Image areas that do not belong to the sample phantom were masked. The mask covers image areas with less than 30 % normalized signal intensities for off-resonant saturation. Normalization was done using a ROI covering the 4 x 4 center pixels of the phantom (top row, left). The masked CEST-effect image was further interpolated and overlaid with the respective proton image. b) Same as (a) for single shot images. Figure and figure caption from Klippel et al. 2014[98].

2.2.2.5. Hyper-CEST spectroscopy within a perfused bioreactor

The bioreactor setup was primarily developed for the demonstration of hyper-CEST MRI applications. Nevertheless it also allows obtaining spectroscopic information concerning the hyper-CEST signature of labeled cells as it is routinely done by using direct xenon delivery.

Spectroscopy within the bioreactor setup is more time consuming when compared to spectroscopy based on direct xenon delivery. Beside the need for cell immobilization this is related to an extended time for xenon delivery between the individual signal acquisition steps. While efficient xenon delivery by direct bubble dispersion is achieved in ca. 10 sec it takes around 40 sec in case of indirect perfusion while this is mainly caused by the need for xenon diffusion into the cell immobilization matrix. The perfusion time has been optimized within initial bioreactor experiments (data not shown). The measurement time for a typical hyper-CEST spectrum covering the cryptophane chemical shift range (90-40 ppm) at a step size of 1 ppm for the individual frequency offsets is therefore ca. 40 min within the bioreactor while it is ca. 15 min within the direct bubbling setup (including 10 sec saturation per frequency step). On the other hand, direct xenon delivery causes cell fragmentation that leads to the release of cryptophane as it was confirmed by the observation of an additional signal for unbound cryptophane in such experiments next to the signal of labeled cells.

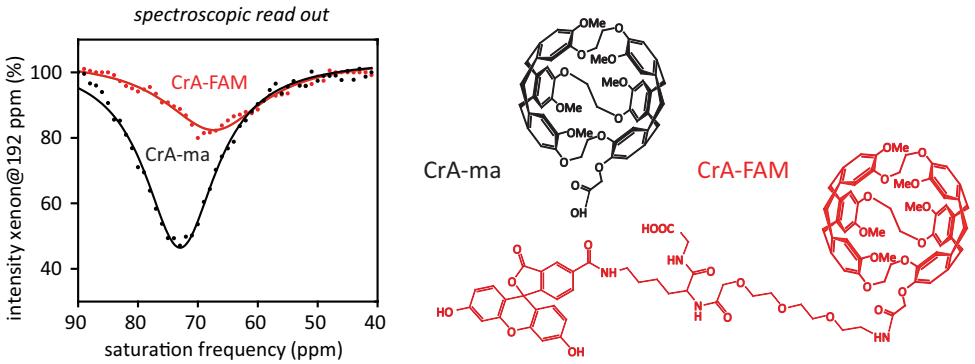

Figure 2.17: Comparison of hyper-CEST response for CrA-FAM and CrA-ma labeled cells. Measurements were done at 32 °C by using the continuous flow bioreactor. Overlay of CEST-spectra measured after labeling cells with CrA-FAM (red line) or CrA-ma (black line). Both spectra were acquired under the same measurement conditions (sample perfusion: 30 sec, saturation pulse: 30 sec with 6.5 µT, frequency interval: 1 ppm). Data points were fitted using an exponential Lorenz function. Structures of the used cryptophane molecules are shown. Figure and figure caption from Klippel et al. 2014[98].

To further illustrate this, hyper-CEST spectra of L929 cells labeled for 20 hours with 50 µM of either unmodified- (CrA-ma) or fluorescence conjugated cryptophane (CrA-FAM) has been measured within the bioreactor setup (figure 2.17). As expected, the spectra revealed the presence of a single signal for cell internalized cryptophane for both constructs while no signal for unbound or cell released cryptophane could be observed.

The CEST-response for cells labeled with CrA-ma was approximately 50 % (at 72 ppm) and approximately 20 % (at 69 ppm) in case of CrA-FAM-labeling. The observed chemical shift difference (ca. 3 ppm) between the cell related signals for CrA-ma and CrA-FAM is most likely due to the different chemical structures of the two xenon hosts as a result of the fluorescein conjugation.

A comparison of the signal intensities for both constructs allows comparing their potential for MRI cell-tracking: The hyper-CEST amplitudes for both cell internalized cryptophane molecules (CrA-ma or CrA-FAM) are influenced by the achieved labeling concentrations, the xenon exchange rates as well as relaxation effects (saturation and measurement conditions were the same).[102] The achieved labeling concentrations depend on the cellular uptake rates for each of the studied constructs. The exchange rate as well as relaxation effects are determined by the structure and the cellular localization of the used construct. Assuming comparable cellular localization and exchange rates for CrA-ma and CrA-FAM the cellular uptake of CrA-ma is ca. 2.5-fold higher compared to the fluorescein-conjugated version. Based on the fluorescence derived intracellular concentration of 15 µM for CrA-FAM the intracellular concentration of unmodified CrA-ma is ca. 40 µM under the given incubation conditions. This conclusion is in line with a higher toxicity for CrA-ma that was related to a higher hydrophobicity of the construct when compared to CrA-FAM causing more efficient uptake due to fluid phase endocytosis.

Although, as shown, hyper-CEST based cell-tracking is possible for CrA-FAM-labeled cells, unmodified CrA-ma is favored due to its better cellular uptake.

The results for *MRI cell-tracking with Cryptophane-A (CrA)* can be also found within the following publication:

Klippel S., Döpfert J., Jayapaul J., Kunth M., Rossella F., Schnurr M., Freund C., & Schröder L. (2014). Cell-tracking with Caged Xenon: Using Cryptophanes as MRI Reporters upon Cellular Internalization. *Angewandte Chemie International Edition,* 53(2), 493–496. [98]

Author contributions: S.K, C.W. and L.S. designed research; S.K., C.W., J.D., J.J. and F.R. performed research; S.K., J.D., M.K. and M.S. analyzed data, S.K., C.W., C.F., and L.S. wrote the paper.

2.2.2. Multi-channel MRI cell-tracking with cryptophane-A and PFOB nanodroplets

During this thesis a new type of xenon host, namely PFOB nanodroplets, has been described and the chemical shift of xenon within the nanodroplets was reported to be ca. 120 ppm.[89] The big chemical shift difference for xenon within either CrA (60 ppm) or PFOB nanodroplets (120 ppm) motivated the combined use of both xenon hosts for cell-labeling applications with frequency selected (multi-channel) detection.

2.2.2.1. Cell-labeling properties of CrA and PFOB

Cell labelling and sensitive MRI cell-tracking was successfully demonstrated for supramolecular xenon nanocarriers of the cryptophane-A type (figure 2.18) as it is described within the previous part of this thesis. The chemical shift of cell internalized cryptophane-A was determined to be ca. 70 ppm under physiological conditions while intracellular concentrations of ca. 40 µM (estimation) could be achieved by unspecific labeling within mouse fibroblasts.

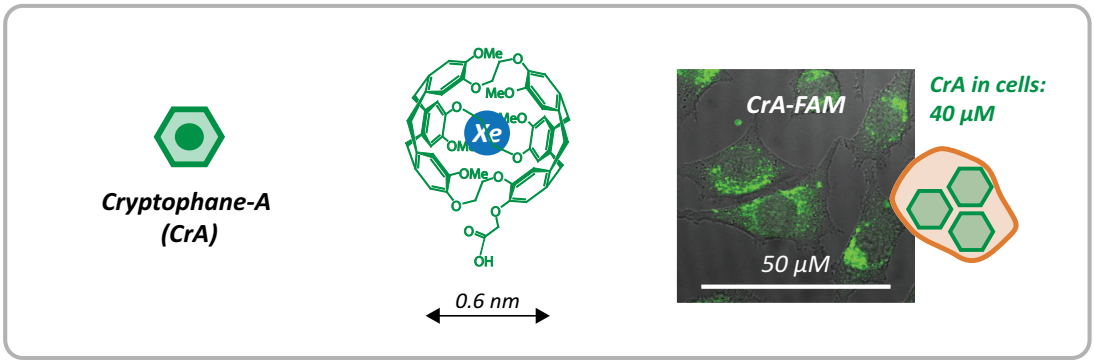

Figure 2.18: Supramolecular xenon hosts of the cryptophane-A type (shown as a schematic, left) has been used for unspecific cell-labeling. Cell uptake was demonstrated by labeling L929 fibroblasts with fluorescence labeled cryptophane molecules (CrA-FAM: green fluorescence), leading to intracellular CrA concentrations in the µM range (right). The CrA molecules (cavity volume: ca. 90 Å^3) are tailor made to serve as a temporal host for one xenon atom (center).

Following this, the cell-labeling properties of PFOB nanodroplets have been proofed and optimized in a comparable manner. Experiments were performed with mouse fibroblasts (L929) since this cell type was already characterized in detail for cryptophane based cell-labeling.

The PFOB cell-labeling procedure was optimized with the aim: a) to generate a high intracellular PFOB concentration without impairing the cellular viability b) to achieve a comparable MRI contrast intensity

as for CrA based cell-labeling. This was motivated since comparable contrast intensities for both contrast agents allows for comparing their individual sensitivity with respect to the achieved intracellular concentrations.

PFOB-nanodroplets with a uniform diameter of 200 nm were prepared by high pressure homogenization according to a protocol used by Stevens et al. (2013)[89] within their initial demonstration of hyper-CEST detection for such nanodroplets (see methods).
The cellular uptake of the PFOB nanodroplets was validated by incorporating the fluorescence dye DiI into the nanodroplet formulation by simple coincubation. This allowed for studying the cellular localization of the labeled nanodroplets (PFOB-DiI) by fluorescence microscopy as well as for uptake quantification by experiments with cell lysates (figure 2.19). DiI is a lipophilic membrane stain that can be used as a long-term fluorescence cell tracer. Nevertheless, it has also been used for fluorescence staining of perfluorcarbon (PFC) nanodroplets such as PFOB to verify cell-labeling in Fluor-19 based MRI cell-tracking application. [103–105] Leakage of the dye from labeled PFC nanodroplets is not reported.

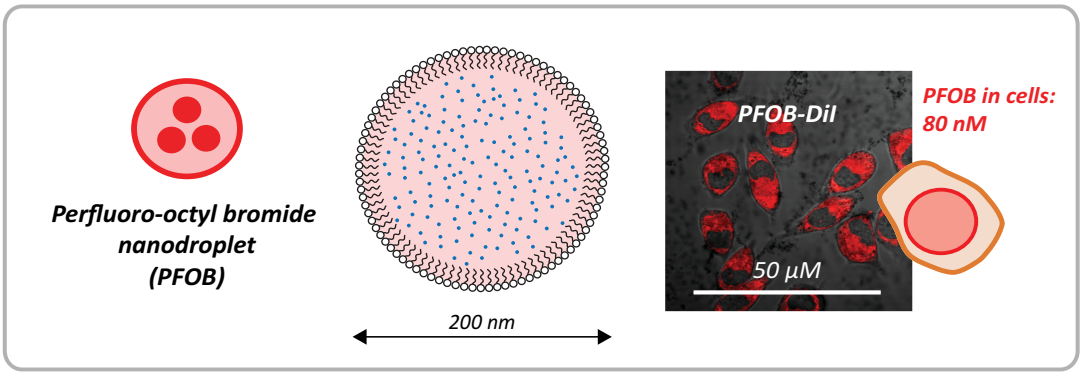

Figure 2.19: Emulsions of PFOB nanodroplets (shown as a schematic, left) has been used for unspecific cell-labeling. Cell uptake was demonstrated by labeling L929 fibroblasts with fluorescence labeled nanodroplets (PFOB-DiI: red fluorescence). Intracellular PFOB concentrations in the nM range could be achieved (right). The nanodroplets are produced by high pressure homogenization resulting in beads with a uniform diameter of ca 200 nm. The droplets (cavity volume: ca. 4×10^9 Å^3) can serve as a temporal host for multiple xenon atoms (center).

A PFOB stock solution (16 nM) was prepared according to the protocol used by Pines and coworkers[89]. The cell incubation time was set to 18 h for PFOB labeling in order to use the identical incubation time as used for CrA labeling. This time frame is in accordance with other *ex vivo* labeling of cells with nanoemulsions including PFOB [93,105,106]. The stock solution was diluted within cell culture medium. It was found that a 1:10 dilution (resulting in an incubation concentration of 1.6 nM PFOB) had no toxic effect on cells (checked by Trypan blue staining) while the cellular uptake of PFOB achieved for this incubation condition gave a contrast intensity that was comparable to cell-labeling with CrA (shown later).

Under the optimized incubation conditions (1.6 nM PFOB, 18 hours, 37°C) intracellular PFOB concentrations of ca. 80 nm could be achieved within L929 mouse fibroblasts as verified by fluorescence quantification in cell lysates (see methods). The cellular viability was not affected by the chosen labeling conditions as it was analyzed by simple Trypan blue staining. The dye is excluded from live cells while it gets accumulated within dead cells due to increased membrane permeability. More complex viability studies (such as alamarBlue® cell viability assessment) that have been performed for cryptophane based cell-labeling were not necessary since the nontoxic effect of PFC nanodroplets onto cells was already well known (see introduction) and studied in detail.[107]

2.2.2.2. Spectroscopic hyper-CEST signature of co-labeled cells

Very sensitive hyper-CEST detection of PFOB nanodroplets has been already demonstrated within test solutions by pines and coworkers.[89] Nevertheless it was not clear if: a) Hyper-CEST allows for sensitive detection of cell internalized PFOB nanodroplets and b) it is possible to selectively detect CrA molecules and PFOB nanodroplets in cellular environments next to each other.

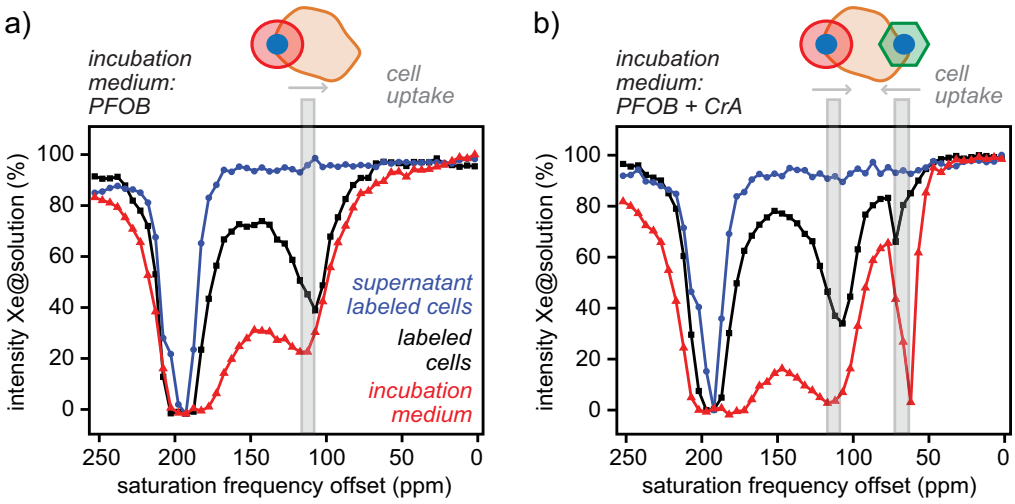

Figure 2.20:. Cellular uptake of xenon inclusion complexes can be monitored by hyper-CEST-spectroscopy. The intensity of xenon in solution was observed following a 5 sec, 8 µT cw saturation at varying frequency offsets. (a) The CEST response of Xe@PFOB shifts upfield after cellular internalization while the spectral resolution is improved. (b) Co-incubation of cells (10 million cells/mL) with PFOB and CrA reveals a xenon chemical shift separation of approximately 40 ppm between both cell-internalized xenon hosts. Chemical shift changes related to cellular uptake of the respective MRI tracers are indicated by gray bars. Schematics are used according to figure 2.21. Figure and figure caption from Klippel et al. 2014.[108]

Initially, the spectroscopic hyper-CEST signature of PFOB labeled cells has been analyzed. The data demonstrates that the nanodroplet uptake into cells can be monitored by hyper-CEST spectroscopy as shown in figure 2.20a. Cells were labeled with PFOB under the optimized incubation conditions described above. The labeled cells were further suspended within fresh cell culture medium (10 million cells/mL) and analyzed by hyper-CEST spectroscopy with direct xenon delivery. The signal of PFOB within the incubation medium (centered at 120 ppm) was shifted by 10 ppm upfield when compared to the signal of PFOB in a cellular environment (centered at 110 ppm) at physiological temperature. In addition, the CEST-peak for xenon within the nanodroplets was better resolved from the CEST-peak for direct xenon saturation (centered at 192 ppm) after cellular internalization. This observation can be related to a change within the PFOB droplet size or the xenon exchange dynamics following cellular uptake. The data therefore illustrates for the first time the feasibility to detect nanomolar concentrations of cell internalized perfluorcarbon nanodroplets by saturation transfer based detection.

Nevertheless, a comparable chemical shift change into the opposite direction was already confirmed for the cell uptake of cryptophane-A (see previous section). The labeling experiment was therefore repeated while the PFOB incubation medium was blended with CrA (50 µM). Botch xenon nanocarriers were internalized by cells while their individual signals could be discriminated by a chemical shift difference of ca. 40 ppm in between them (figure 2.20b).

Further more, the CEST-peaks of both cell internalized xenon nanocarriers showed only minor spectral overlap under the used saturation conditions (cw-saturation for 5 sec with 8 µT) motivating their use for multi-channel cell-labeling applications with frequency selective detection. Since cells have been co-labeled with both xenon hosts at the same time, the data also illustrates that the achieved chemical shift difference of 40 ppm is only caused by the chemical properties of the used xenon host rather than by biological variations within the labeled cells.

2.2.2.3. Concept for multi-channel MRI cell-tracking

The possibility to detect sufficiently separated NMR signals for both xenon nanocarriers within cellular environments has been demonstrated. This enables the sensitive NMR localization of individually labeled cells by multi-channel hyper-CEST MRI

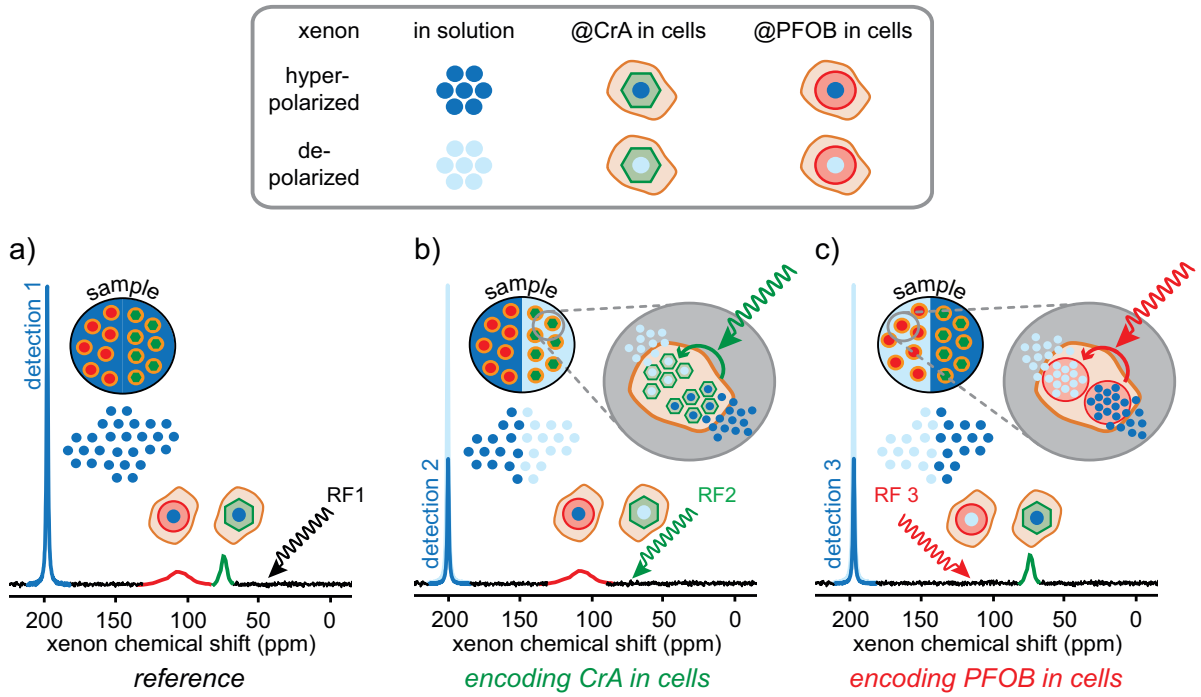

Figure 2.21: Principle of multi-channel hyper-CEST detection for cell-labeling. The MRI signal of hyperpolarized xenon in bulk solution acts as a sensing medium. It reports on the spatial distribution of two distinct cell-internalized xenon inclusion complexes (CrA and PFOB) both characterized by a unique xenon chemical shift. A reference scan visualizes the unaffected distribution of xenon in solution ((a) off-resonant saturation). The localization of cells either labeled with CrA ((b) on-resonant saturation for xenon@CrA in cells) or PFOB ((c) on-resonant saturation for xenon@ PFOB in cells) is encoded within the sensing medium by a frequency-specific saturation transfer acting on xenon atoms temporarily entrapped within the respective cell-internalized nanocarrier. Schematic spectra are shown for clarification as are participating xenon pools on top. Peak widths differ due to different exchange conditions. Figure and figure caption from Klippel et al. 2014.[108]

The localization of cells that have been labeled with either CrA or PFOB can be achieved within three subsequent MRI acquisitions as conceptually illustrated within figure 2.21. A first reference scan visualizes the distribution of xenon in solution that is acting as a sensing medium. The rf-saturation pulse is therefore centered off-resonant. A second scan encodes the localization of CrA labeled cells by a signal depletion within the sensing medium while the saturation pulse is centered at the frequency of cell-internalized CrA (ca. 70 ppm). The localization of PFOB labeled cells is achieved in a comparable manner by a third scan. The saturation pulse has to be centered at the frequency of cell-internalized PFOB (ca. 110 ppm). This causes a localized depletion of the xenon in solution signal in spatial proximity to PFOB labeled cells.

2.2.2.4. Multi-channel MRI localization of PFOB and CrA labeled cells

The frequency selective localization of cells that has been either labeled with PFOB or CrA was demonstrated by direct xenon delivery with cells in solution. Cell-labeling was done according to the incubation conditions optimized earlier (for CrA: 50 µM, for PBOB: 1.6 nm, incubation for 18 hours at 37 °C).

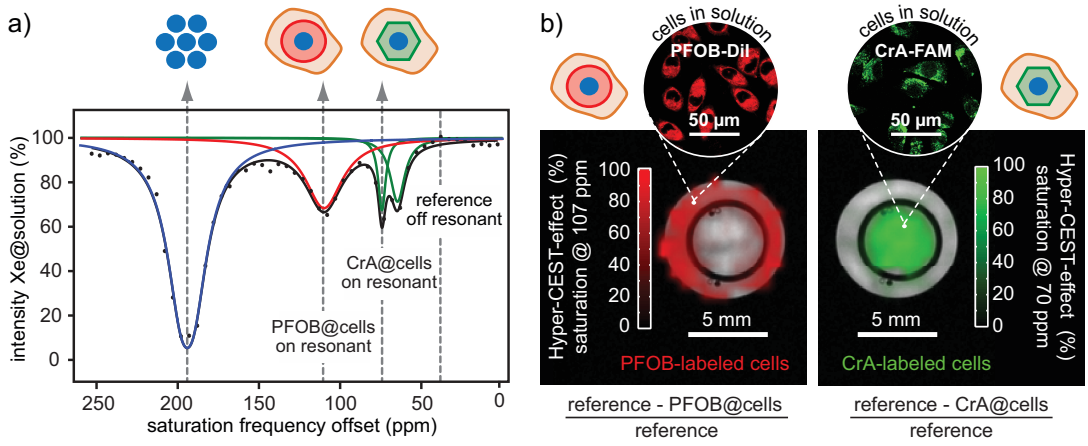

Figure 2.22: PFOB- and CrA-labeled L929 cells (10 million cells/mL) can be selectively localized by multi-channel xenon-MRI as demonstrated for a two compartment phantom (outer compartment, PFOB-labeled cells; inner compartment, CrA-labeled cells). a) The saturation frequency offsets used for hyper-CEST imaging are indicated within the associated CEST-spectrum (8 sec, 10 µT cw saturation) by gray dotted lines. Exponential Lorentzian fits are shown as solid lines. Schematics are used according to Figure 1. b) 1H-MR-Images are shown in overlay with pseudo-colored hyper-CEST-effects derived for both contrast agent-specific saturation conditions. Cell-labeling was confirmed by laser scanning microscopy with fluorescence labeled versions of both hyper-CEST agents as depicted within the circular insets (labeling with the fluorescence probes was done under the same incubation conditions as the NMR experiments). Figure and figure caption from Klippel et al. 2014.[108]

A double compartment phantom with PFOB-labeled cells in the inner and CrA-labeled cells in the outer compartment was used to verify the spatial selectivity. Prior to the MRI experiment a hyper-CEST spectrum has been recorded to verify the resonance frequencies of each of the individual cell internalized xenon nanocarriers (figure 2.22a). The localization of labeled cells could further be clearly restricted to the respective phantom compartments with a mean hyper-CEST effect of ca. 80 % for both nanocarriers as illustrated within figure 2.22b.

Figure 2.23 gives an overview about post processing routines that have been applied to the MRI raw of the given experiment. The average of 20 magnitude-images detecting xenon in solution is shown for off-resonant saturation (irradiating at 23 ppm) and on-resonant saturation (xenon@PFOB in cells: irradiating at 107 ppm or xenon@CrA in cells: irradiating at 70 ppm; cw saturation for 8 sec with 10 µT).

The CEST effect was evaluated by calculating the percentage reduction of single-pixel intensities due to on-resonant saturation for both applied on-resonant frequencies individually. This allows an analysis independent from slightly different xenon delivery throughout the sample phantom.

Areas within the calculated CEST-effect images that do not belong to the sample phantom were masked as shown within the figures. The masked CEST-effect images (32 x 32 pixels) were resized by cubic spline interpolation to the resolution of the underlying proton MR-images (256 x 256 pixels). The contrast within the resulting difference images is false-color coded with respect to the frequency of the applied on-resonance scans which is related to the individual cell tracers (red: on-resonant saturation at 107 ppm, green: on-resonant saturation at 70 ppm).

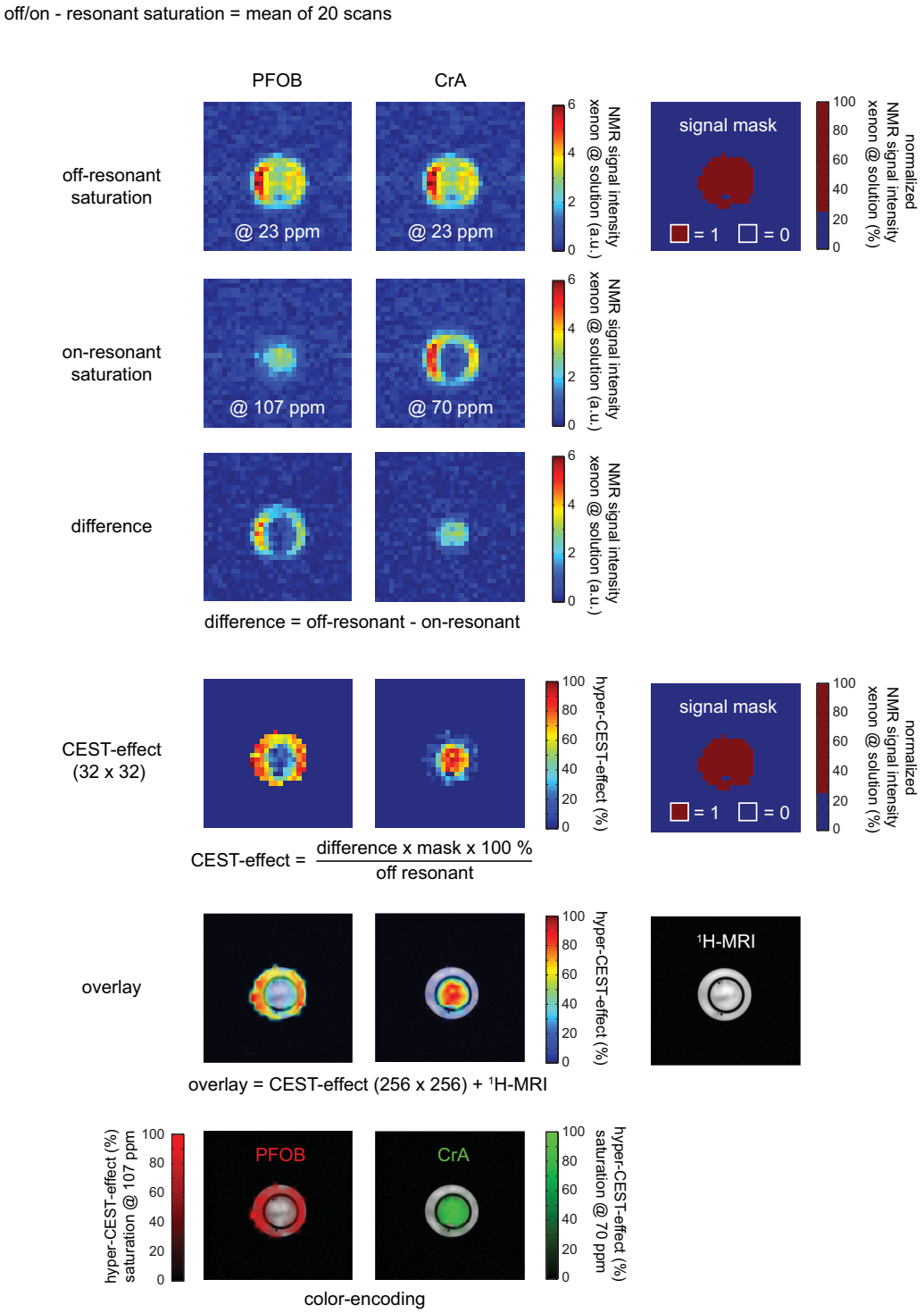

Figure 2.23: Post-processing of MR-images shown in figure 2.22 (cw saturation for 8 sec with 10 µT).

2.2.2.5 Multi-channel live-cell-tracking

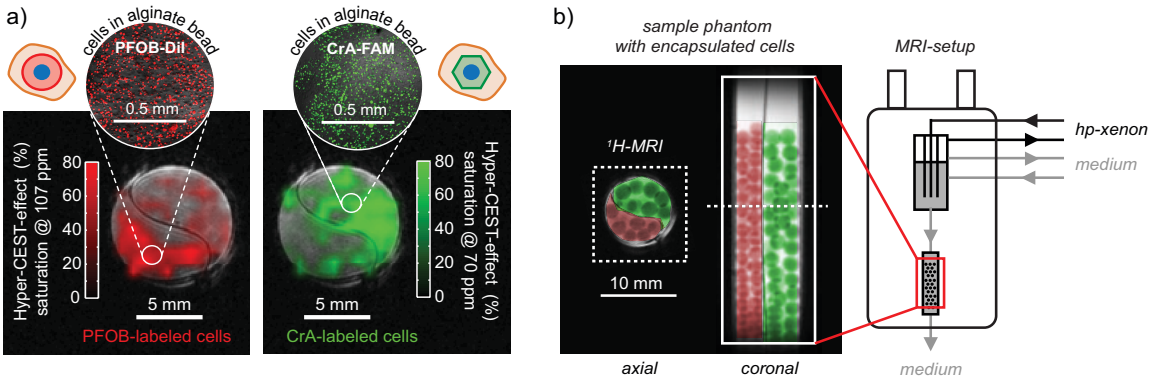

Figure 2.24: Live cell multi-channel xenon-MRI within a perfused bioreactor system. b) Alginate-immobilized cells, labeled with either PFOB (intracellular concentration, 80 nM) or CrA (intracellular concentration, 40 µM) has been perfused with xenon-saturated medium. a) Selective cell-tracking could be achieved within 2 hyper-CEST acquisitions per contrast agent. Cell-labeling of alginate encapsulated cells was confirmed by laser scanning microscopy with fluorescence-labeled versions of both hyper-CEST agents as depicted within the circular inlets. Schematics are used according to figure 2.21. Figure caption adopted from Klippel et al. 2014.[108]

Following the demonstration of multi-channel MRI cell-labeling by the use of direct xenon delivery, the concept was also verified within the developed bioreactor setup on live cells (fibroblasts L929). Cells have been labeled with either CrA or PFOB according to the incubation conditions optimized earlier (for CrA: 50 µM, for PBOB: 1.6 nm, incubation for 18 hours) resulting in intracellular concentrations of 40 µM for CrA and 80 nM for PFOB (for quantification see methods).

The frequency selective MRI localization of ca. 5 million labeled cells could be achieved within two hyper-CEST acquisitions (4 min) per contrast agent (figure 2.24). The maximal achieved saturation transfer effect for CrA- and for PFOB labeled cells was 80 % in both cases under identical saturation conditions. The live-cell experiment therefore verifies the expected higher sensitivity for cell internalized PFOB nanodroplets and demonstrates the potential of multi-channel MRI cell-tracking under *in vivo* like xenon delivery conditions.

Figure 2.25 gives a detailed overview about post processing routines that have been applied to the MRI raw data of the given experiment. The average of 2 magnitude-images detecting xenon in solution is shown for off-resonant saturation (irradiating at 23 ppm) and on-resonant saturation (xenon@PFOB in cells: irradiating at 107 ppm or xenon@CrA in cells: irradiating at 70 ppm; cw saturation for 10 sec with 10 µT). The CEST effect was evaluated by calculating the percentage reduction of single-pixel intensities due to on-resonant saturation for both applied on-resonant frequencies individually. This allows an analysis independent from slightly different xenon delivery throughout the sample phantom. Areas

within the calculated CEST-effect images that do not belong to the sample phantom were masked as shown within the figures. The masked CEST-effect images (32 x 32 pixels) were resized by cubic spline interpolation to the resolution of the underlying proton MR-images (256 x 256 pixels).
The contrast within the resulting difference images is false-color coded with respect to the frequency of the applied on-resonance scans which is related to the individual cell tracers (red: on-resonant saturation at 107 ppm, green: on-resonant saturation at 70 ppm).

The results for *Multi-channel MRI cell-tracking with cryptophane-A and PFOB nanodroplets* can be also found within the following publication:

Klippel S., Freund C., & Schröder, L (2014).
Multichannel MRI Labeling of Mammalian Cells by Switchable Nanocarriers for Hyperpolarized Xenon.
Nano Letters, 14(10), 5721–5726.[108]

Author contributions: S.K. designed research, performed research and analyzed data, S.K., C.F., and L.S. wrote the paper.

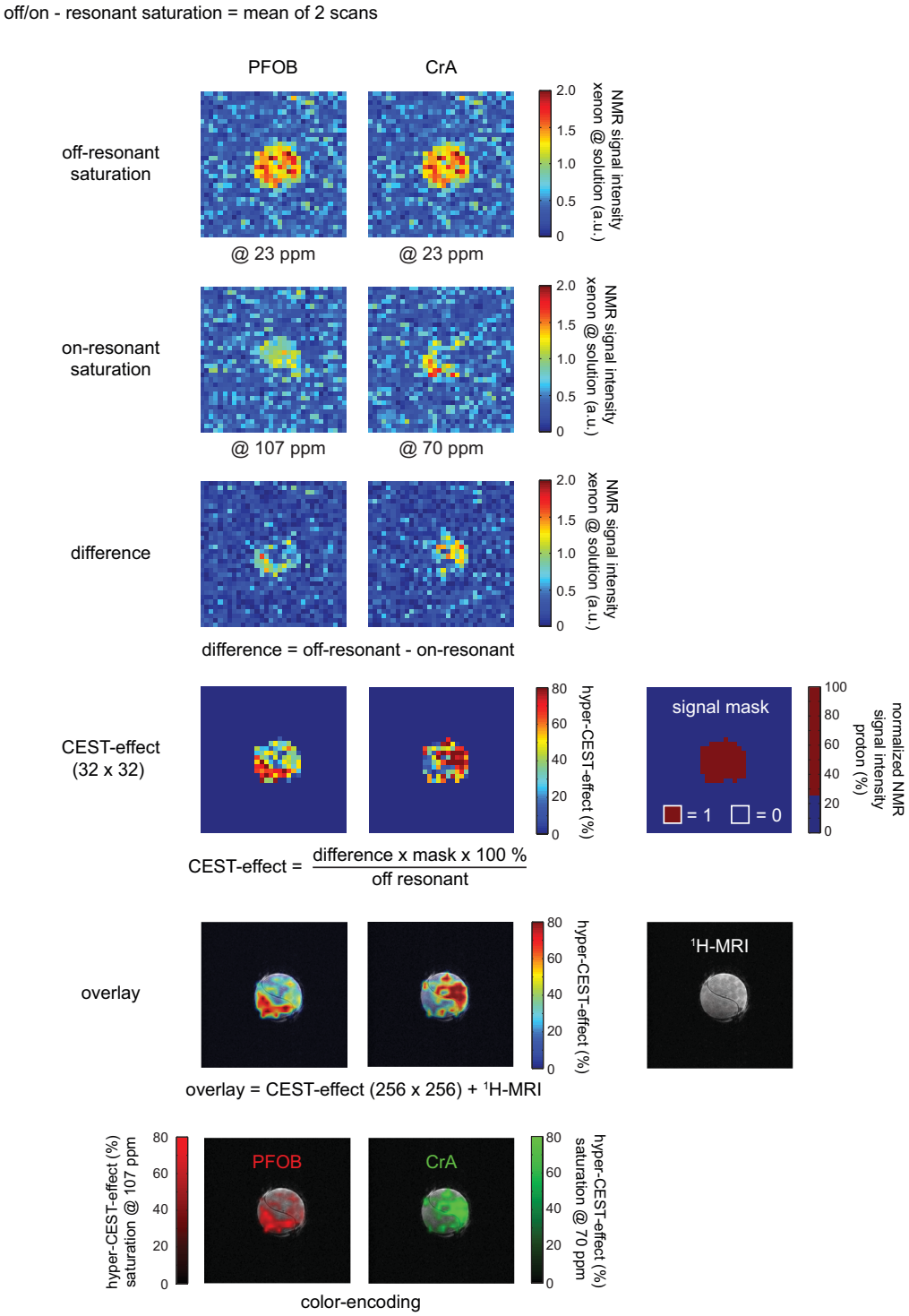

Figure 2.25: Post-processing of MR-images shown in figure 2.24 (cw saturation for 10 sec with 10 µT).

2.3. Molecular MRI with targeted xenon nanocarriers

The focus of the previous section was on the development and demonstration of unspecific cell-labeling schemes for cell-tracking applications with non-targeted xenon hosts.
Next to cell-tracking, a quite important subfield of cell-labeling comprises the specific labeling of disease related cell markers such as cell surface receptors or glycosylation patterns. Specific cell-labeling requires a pairing of the contrast agent to a targeting unit that is capable to interact with the cell marker of choice. Constructs that consist of a targeting unit and a suitable read out module for imaging are called biosensors. Appropriate targeting units for cell surface receptors are for example peptides or antibodies that allows for specific binding events leading to either cell surface labeling or receptor mediated cellular internalization of the contrast agent. In contrast to unspecific cell-labeling which is typically done *ex vivo,* such specific cell-labeling allows for *in vivo* labeling applications off disease associated biomarkers, an approach that is called molecular imaging.
The aim was to demonstrate molecular imaging within the developed live-cell bioreactor for three different types of targeted cryptophane biosensors. The biosensors as well as labeling schemes have been developed by colleagues and collaboration partners as cited.

(i) At first, a modular biosensor was developed that allows for the coupling of several cryptophane molecules to an antibody via an avidin-biotin bridge. Specific cell-labeling and detection is demonstrated for a CD14-specific version of this modular biosensor by hyper-CEST experiments with direct xenon delivery.

(ii) Following this, initial results for a scaffolded biosensor are shown. The scaffolding approach increases the number of cryptophane cages per targeting unit by two orders of magnitude, therefore further increasing the sensitivity of hyper-CEST MRI. Live-cell molecular imaging within the bioreactor setup is demonstrated for an EGFR-specific version of the scaffolded biosensor.

(iii) Finally, molecular imaging off cell surface glycosylation patterns is demonstrated by live-cell experiments within the developed bioreactor setup. The used biosensor consists of a cryptophane unit connected to a bioorthogonal group and enables the MRI detection of metabolically modified cellular glycan structures.

2.3.1. A modular cryptophane biosensor targeting CD14

The first tested biosensor was synthesized in a modular fashion. The design enables the coupling of several cryptophane molecules to an exchangeable antibody via avidin-biotin interactions. The biosensor concept was developed and demonstrated by Dr. Honor May Rose, Dr. Christopher Witte and Federica Rossella. Specific cell-labeling and MRI detection has been demonstrated for a CD14-specific version of this biosensor by hyper-CEST experiments with direct xenon delivery.[109]

In brief: An anti-CD14 IgG2b monoclonal antibody has been conjugated to avidin molecules via lysine side chain coupling (targeting module). Next to this, CrA-ma and fluorescein were each coupled to biotin via a PEG linker (read out modules). The read out modules were grafted onto the targeting module by avidin-biotin interactions. Each antibody-coupled avidin molecule was conjugated to 3 cryptophane-biotin molecules (xenon-MRI) and 1 fluorescein-biotin molecule (fluorescence microscopy and flow cytometry) resulting in a dual mode biosensor that is shown in figure 2.26 (left) as a schematic. The target specificity of the biosensor was confirmed by comparing the labeling efficiency for cells with a low CD14 expression level (3T3 cells) to cells with a high CD14 expression level (RAW 264.7 cells). The successful MRI localization of RAW cells was achieved by a hyper-CEST effect of ca. 80 % while the hyper-CEST effect for the 3T3 control cells was comparably small (ca. 20 %). The xenon-MRI data were complemented by spatial localized hyper-CEST spectroscopy and confirmed by fluorescence based quantification of the labeling efficiency as shown within figure 2.26 (middle and right). Details about biosensor synthesis and cell-labeling can be found within the methods section.

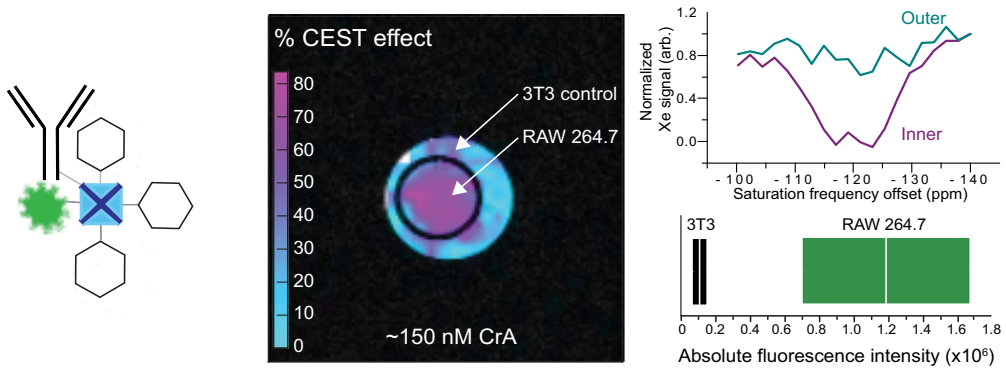

Figure 2.26: Molecular imaging of CD14 expression levels on cells by hyper-CEST MRI. Left: Schematic of the used modular cryptophane-antibody conjugate. Cryptophane and fluorescein molecules were coupled to an anti-CD14 antibody via biotin-avidin interactions. Middle: The CD14 expression level was correlated to the observed CEST-effect witch allowed to differentiate between 3T3 cells with a low CD14 expression level (outer compartment) and RAW 264.7 cells with a high CD14 expression level (inner compartment). The MR-image was calculated by subtracting the accumulation of 10 on-/off-resonance images each (cw-saturation with 30 µT for 26 sec). Right: The xenon MRI data has been complemented by spatial localized CEST spectroscopy obtained for the inner and outer compartment separately (top). Flow cytometry was used to quantify the cellular labeling efficiency for both cell types. The fluorescence data are in line with the NMR/MRI results (bottom). Figures from Ref. [109].

The RAW cells have been detected by xenon-MRI based on a cryptophane concentration of ca. 150 nM, thus demonstrating the potential of targeted xenon biosensors for molecular imaging applications. Importantly, the targeting unit can be easily exchanged for other antibodies. This allows labeling and detection of a variety of different cell surface markers in a modular and sensitive manner. As already mentioned the MRI experiments have been performed by direct xenon delivery causing cell death and fragmentation.

Therefore experiments with biosensor labeled cells have been performed within the developed bioreactor setup. Nevertheless, these experiments were not successful due to initial problems with the used labeling and cell encapsulation scheme:

MRI experiments within the bioreactor setup require cell encapsulation within alginate beads to prevent cell washout in a media-perfused system. For cell-labeling with unmodified cryptophanes, it is possible to label the cells after alginate encapsulation since the cryptophane molecules are small enough (diameter: ca 0.6 nm) to diffuse into the pores of the alginate matrix (diameter: ca 17 nm, [110]). Such cell-labeling after cell encapsulation is not possible with comparable large cryptophane-antibody conjugates such as the modular biosensor (molecular weight ca. 160 kDa). It has been shown that alginate hydrogels of comparable composition are lowering the diffusion of proteins (155 kDa) to 100-fold as compared to their diffusion in water.[110] For this reason cells have to be labeled first with the biosensor followed by an alginate-encapsulation of the pre-labeled cell material. For alginate encapsulation, the cell-alginate mixture is trickled into a solution containing 1.5 % $CaCl_2$ (55 mM). The divalent calcium-ions within this solution serve as cross linkers between the polysaccharide building blocks of alginate acid. This crosslinking causes an immediate alginate polymerization and therefore the formation of stable alginate droplets. The beads are kept within the calcium solution for 30 min to complete the crosslinking procedure before they are transferred into DMEM.

It turned out that that the high calcium-ion concentrations within the formed alginate beads are problematic for hyper-CEST experiments with encapsulated and cryptophane labeled cells when directly (ca. 1 to 2 hours) performed after the encapsulation procedure. NMR experiments showed that certain ions can interact with cryptophane molecules while this interaction hampers the xenon-cryptophane exchange and therefore the hyper-CEST effect.[111]

It was found that an additional equilibration step for ca. 18 hours within Dulbecco's Modified Eagle's Medium/DMEM with a low calcium ion concentration of 1.8 mM allows to overcome the mentioned problems most likely by reducing the calcium ion concentration within the alginate matrix. The mechanical properties of the alginate beads were not negatively influenced. The labeling/encapsulation scheme therefore has to be performed in the order: (1) cell-labeling with biosensor, (2) encapsulation of labeled cells in alginate beads, (3) equilibration of encapsulated cells for ca. 18 hours in DMEM. The optimized protocol can be found in detail within the methods section.

It has to be noted, that such an additional equilibration step was not necessary for experiments with unmodified CrA. Here cells are encapsulated firsts followed by cryptophane labeling in DMEM for 18 hours, which already reduces the calcium ion concentration within the alginate matrix.
Although this optimized protocol was not applied to the discussed modular biosensor so far, it has been successfully used for the two other biosensors studied within this thesis (see below). Further experiments therefore should aim for a repetition of the initial bioreactor experiments under the optimized encapsulation/labeling conditions.

Further information's and results including a detailed characterization of the biosensor labeling procedure by fluorescence microscopy and flow cytometry can be found within the following publication:

Rose H. M., Witte C., Rossella F., **Klippel S.**, Freund C., & Schröder L. (2014).
Development of an antibody-based, modular biosensor for 129Xe NMR molecular imaging of cells at nanomolar concentrations.[109]
Proceedings of the National Academy of Sciences of the United States of America. 111(32), 11697–702.

Author contributions H.M.R., C.W., and L.S. designed research; H.M.R., C.W., F.R., and S.K. performed research; H.M.R., C.W., S.K., and L.S. analyzed data; and H.M.R., C.W., F.R., C.F., and L.S. wrote the paper.

2.3.2. A scaffolded cryptophane biosensor targeting EGFR

An alternative biosensor approach relies on the coupling of many cryptophane molecules onto targeted scaffold structures in order to further increase the sensitivity of hyper-CEST MRI. Different scaffolds that allows for such cryptophane conjugations have been proposed and studied including branched dendrimers[112], viral capsids [113] or filamentous bacteriophages[114].
In a recent publication inactivated fd-bacteriophages have been engineered by phage display to achieve binding specificity for EGF receptors (EGFR) on cancer cells.[75] The phages were conjugated to cryptophane molecules (ca. 300 per phage) which enabled hyper-CEST detection of this scaffolded biosensors (figure 2.27a) at picomolar concentrations. Although specific binding of the biosensor to MDA-MB 231 cells (EGFR-positive) was demonstrated, the achieved hyper-CEST contrast (15%, CEST-parameter: saturation for 10 sec with 30 µT) was comparably small and MRI localization was not achieved. Next to the low contrast, successful MRI experiments were probably constrained by

comparable low xenon intensities (SNR=12) achieved as a result of high cell densities (100 million cells/mL).

The scaffolded biosensor was resynthesized (M13-phages were used instead of fd-phages, see methods) by Dr. Jabadurai Jayapaul in collaboration with Prof. Matthew Francis and Prof. David Wemmer (UCSF Berkley) to further evaluate and optimize the cell-labeling concept and to demonstrate sensitive molecular imaging of live cells within the developed bioreactor setup.

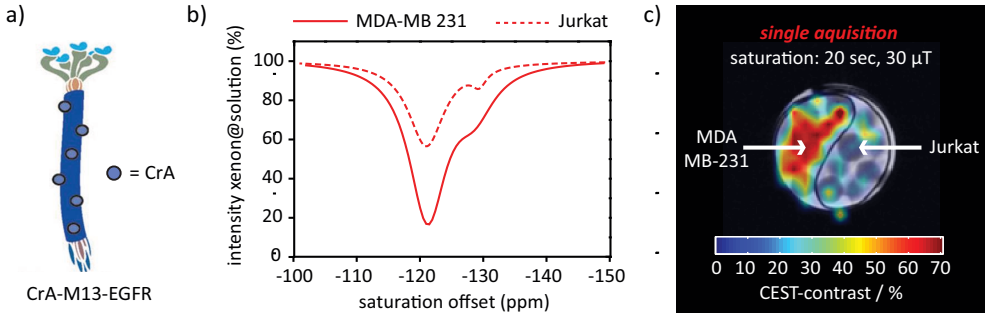

Figure 2.27: Hyper-CEST performance of a scaffolded cryptophane biosensor targeting cellular EGF-receptors. a) A schematic of the biosensor construct illustrates the distribution of multiple cryptophane molecules (CrA) along a filamentous bacteriophage scaffold (dark blue). The EGFR specific single-chain antibody fragments are depicted on the upper part of the phagestructure (light blue). The figure is adapted from Ref. [75]. b) Hyper-CEST spectrum of labeled MDA-MB 231 cells (EGFR-positive, solid line) and Jurkat cells (EGFR-negative, dotted line) as an overlay. c) Live cell molecular imaging within the perfused bioreactor setup. The localization of labeled MDA-MB 231 cells within the left compartment could be achieved by an average CEST-effect of ca. 60 %. Only weak contrast was observed for control cells. Hyper-CEST MRI parameters are given within the figure.

By optimizing the cell-labeling procedure (incubation with 5 nM biosensor for 1 hour instead of 0.8 nM biosensor for 2 hours) it was possible to demonstrate EGFR-specific binding of the scaffolded biosensor by hyper-CEST spectroscopy with direct xenon delivery. The observed CEST-effect for biosensor labeled MDA-MB 231 cells was ca. 80 % and for Jurkat cells ca. 40 % (see figure 2.27b, cw-saturation with 6 µT for 10 sec). MDA-MB 231 cells could therefore been detected by a contrast difference of ca. 40 % at a cell density of 10 million cells/mL. Following this, the scaffolding approach has been successfully demonstrated by hyper-CEST MRI on live cells (15 million cells/mL) within the perfused bioreactor setup. In this context the localization of labeled MDA-MB 231 cells (EGFR-positive) next to Jurkat cells (EGFR-negative) could be achieved within a single hyper-CEST acquisition (cw-saturation for 20 sec with 30 µT) by a CEST- effect of ca. 60 % while for control cells only low contrast has been observed (figure 2.27c). Although the shown data are quite promising, additional experiments have to be performed to further validate the biosensor by fluorescence based quantification such as flow cytometry.

2.3.3. A cryptophane biosensor targeting glycosylation

A biosensor targeting approach quite differed to antibody-receptor interactions (shown for the two biosensors mentioned previously) relies on the covalent interaction between two bioorthogonal groups. Such bioorthogonal groups are able to react with each other under physiological conditions while reactions with other biomolecules do not occur. The principle was used to build a cryptophane based biosensor that is capable to detect metabolically labeled glycan structures on cell surfaces as it is illustrated within figure 2.28. Biosensor development and synthesis was done by Dr. Vera Martos in collaboration with Dr. Honor May Rose and Dr. Christopher Witte. Details about biosensor synthesis, cell-labeling and sample preparation can be found within the methods section.

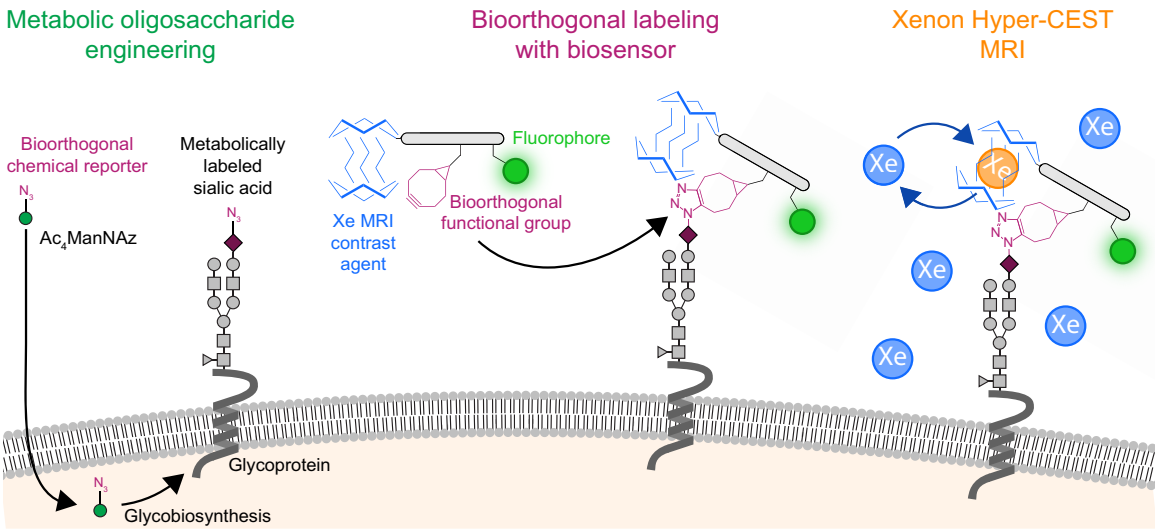

Figure 2.28: Xenon hyper-CEST biosensors targeted to metabolically labelled glycans. Cells are treated with synthetic sugars bearing bioorthogonal functional groups. The sugars are processed through natural metabolic pathways, eventually presenting the bioorthogonal functional group on cell surface glycoproteins and glycolipids. In the next step, cells are treated with the multimodal (xenon MRI/fluorescence) biosensor bearing a complimentary bioorthogonal targeting unit, xenon contrast agent and fluorophore. These two bioorthogonal functional groups undergo a chemical reaction, covalently binding the biosensor to the target glycan. In the final step hyperpolarised xenon is delivered to the sample immediately before measurement. Xenon hyper-CEST MRI uses the reversible binding of xenon to the contrast agent to amplify the biosensor signal. Figure and figure caption adapted from Ref. [115].

The performance of the build biosensor could be successfully demonstrated within the developed bioreactor setup on live cells as shown within figure 2.29. Hyper-CEST MRI allowed the localizing of metabolically labeled cells by a higher hyper-CEST effect (ca. 50 %) when compared to unlabeled cells (ca. 20 %). The image was recorded by using used a 30-µT, 26 second saturation pulse and 10 averages for each on- and off-resonant image. The data therefore illustrates for the first time the possibility to specifically target the cellular glycom of metabolically labeled cells by MRI contrast agents.

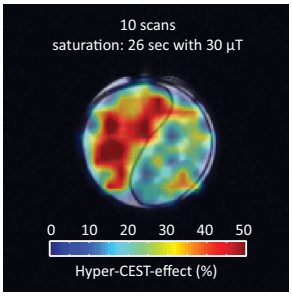

Figure 2.29: Live-cell molecular imaging of metabolically labeled human embryonic kidney (HEK) 293 cells. Cells within the left compartment have been labeled with the modified sugar ($Ac_4ManNAz$) while cells within the right compartment were not labeled (10 million cells/mL, each). Following biosensor incubation of both cell populations, the metabolically labeled cells could be detected by a hyper-CEST effect of ca. 50 % compared to a hyper-CEST effect of ca. 20 % for unlabeled cells. The CEST effect is displayed in percent (pseudo color) overlaid on proton MRI for reference. Xenon CEST images used a 30-µT 26-sec saturation pulse and 10 averages for each on- and off-resonant image.

Further informations and results including a detailed characterization of the labeling procedure by fluorescence microscopy and flow cytometry can be found within the following publication:

Witte C., Martos V., Rose H. M., Reinke S., **Klippel S.**, Schröder L. & Hackenberger C. (2015).
Live-cell MRI of xenon Hyper-CEST biosensors targeted to metabolically-labeled cell-surface glycans.
Angewandte Chemie International Edition, in press, DOI: 10.1002/anie.201410573R1.

Author contributions: C.W., V.M., L.S. and C.H. designed research; C.W., V.M., H.M.R., S.R. and S.K. performed research; C.W., V.M., H.M.R., S.R. and S.K. analyzed data; and C.W. L.S. and C.H. wrote the paper.

3. Conclusion and Perspectives

The following section summarizes achievements for MRI cell-labeling with xenon nanocarriers that have been made within this doctoral thesis. These are discussed in the context of recent achievements within the field. Current limitations of the demonstrated MRI concept are addressed and discussed with respect to a desired *in vivo* translation.

Within this study, substantial progress for cell-labeling with xenon nanocarriers (cryptophanes and perfluorcarbon nanodroplets) could be achieved. This includes unspecific labeling schemes as well as specific labeling approaches. It was demonstrated for the first time that the achievable labeling concentrations (nm to µM) are sufficient for the spatial MRI localization of labeled cells by exploiting the signal amplification of indirect hyper-CEST detection. Further on, the frequency selectivity of the hyper-CEST principle could be used for the multiplexed detection of conceptually different xenon inclusion complexes in cellular environments. The multiplexing concept was demonstrated for unspecifically labeled cells and can be translated to specific labeling demonstrations in the future.
The *in vitro* experiments have been performed in an advanced imaging setup under physiological conditions (bioreactor) with live cells. The setup simulates for *in vivo*-like xenon delivery by indirect cell perfusion with xenon saturated liquids. The thesis therefore provides the basis for a detailed *in vitro* characterization of MRI cell-labeling with xenon nanocarriers as a fundamental need for a successful translation of the concept to preclinical applications.

3.1. Cell-labeling properties of xenon nanocarriers

3.1.1. Cell-labeling with cryptophanes

3.1.1.1. Unspecific cell-labeling through cellular internalization

Unspecific cell-labeling with unmodified and fluorescence-labeled cryptophane-A has been demonstrated for L929 fibroblasts as well as RAW 264.7 macrophages, both derived from mice. These cell lines were chosen since further experiments were aiming to study specific labeling with targeted cryptophane conjugates for both of them (L929: overexpression of MHC2, RAW 264.7: overexpression of CD14). Intracellular cryptophane concentrations in the low µM range could be achieved followed by a successful localization of ca. 5 million labeled L929 fibroblasts by hyper-CEST MRI with high contrast.

In order to further improve the sensitivity for potential cell-tracking applications, one possibility would be to increase the amount of cryptophane cages per cell. This can be achieved by coupling cryptophanes to cationic cell penetrating peptides. By doing so, intracellular cryptophane concentrations ranging from 100 to 160 µM can be achieved within different human cells including two cancer cell lines (AsPC-1, CAPAN-2) and lung fibroblast (HFL-1).[86] The reported labeling concentrations are ca. 10 fold higher when compared to unspecific cell-labeling with unmodified cryptophane achieved in this thesis. Other techniques for efficient unspecific cell-labeling include electroporation[116] or the use of transfection reagents[117], two methods that could also be evaluated in the future.

The cellular internalization of cryptophane-A was related to fluid phase pinocytosis as originally claimed by Boutin and coworkers.[118] Since this uptake mechanism is common for all eukaryotic cells[119], is very likely that virtually all cell types can be labeled with CrA in an unspecific manner with comparable intracellular labeling concentrations, although this has to be proven in further experiments. In this context, the focus for experiments should be on cell lines with relevance for preclinical cell-tracking applications such as immune cells, tumor cells and stem cells.

So far, the characterization of cryptophane labeled cells only relies on a comparably simple viability assessment such as Trypan blue staining, MTT or alamar blue assays. Such methods evaluate the cellular viability based on membrane integrity or metabolic activity. For immune cells a more detailed cellular characterization should also include parameters such as: maturation phenotype, cytokine production, T-cell stimulatory capacity and chemotaxis. Such a characterization ensures that CrA-labeled cells retain their potential to function in immunotherapeutic applications, which is the main reason to track them. Appropriate tests are described in Ref. [120]. For stem cells it has to be ensured that their pluripotency is not affected by CrA-labeling. This is important for desired therapeutic applications including immune reconstitution, enzyme replacement, regenerative medicine, and immunomodulation. Experimental procedures for such cell characterizations can be found in Ref. [107].

3.1.1.2. Specific functionalization of cryptophanes for cell surface epitopes

Specific cell surface labeling with targeted cryptophane-A conjugates (also called biosensors) has been successfully demonstrated for three conceptually different biosensor types:

(i) A modular cryptophane biosensor targeting CD14 (CrA-CD14)
(ii) A scaffolded cryptophane biosensor targeting EGFR (CrA-M13-EGFR)
(iii) A cryptophane biosensor targeting glycosylation patterns (CrA-BCN)

(i) The modular design of the first biosensor type was achieved by connecting an exchangeable antibody (targeting unit) to cryptophane-A molecules (read out module) via an avidin-biotin bridge (see materials section). This modular design allows for an exchange of the targeting unit which enables a high flexibility for different cellular epitopes. As a proof of principle the CD14-receptor has been chosen as a target. CD14 is a well-characterized macrophage marker that can been used to image pathologies such as atherosclerosis[121] as well as cancer [122]. Specific labeling of CD14-positive cells was successfully confirmed by flow cytometry also revealing low unspecific binding of the biosensor to CD-14 negative control cells. Optimal labeling could be achieved with a pre-conjugated biosensor instead of sequential incubation (first: targeting module, second: read out module) resulting in a cryptophane concentration of ca. 150 nM (within NMR read out volume) for CD14-positive cells as determined by fluorescence based quantification. Labeling of control cells resulted in low unspecific binding (ca. 20 nM). This illustrates, that the hydrophobic character of cryptophane-A molecules, which causes a tendency for unspecific cell interactions, can be reduced by the conjugation of hydrophilic counterparts such as antibody targeting units.

(ii) The second tested biosensor design allows further increasing the ratio of cryptophane molecules per targeting unit. This is an important consideration in order to increase the detection sensitivity per cellular target epitope. Within the previously mentioned modular design, each avidin modified lysine side chain of the chosen antibody was coupled to up to 4 cryptophane molecules. Assuming an average number of 4 bound avidin molecules per antibody (coupling ratio was 4:1) it is likely that the number of cryptophane units per antibody is less than 20.
An alternative design approach has been realized that relies on the coupling of up to 300 cryptophane-A molecules onto a bacteriophage scaffolds with antigen specificity. The antigen specificity of the phage scaffold can be engineered by phage display strategies.[123] The scaffolded biosensor can therefore be adapted to different cellular targets as the modular biosensor, although the phage display strategy is more time consuming.

The scaffolded biosensor used within this study was specific for EGF receptors (design adapted from Ref. [75]), a common cell surface marker for several cancer types. The localization of labeled MDA-MB 231 cells (EGFR-positive) next to Jurkat cells (EGFR-negative) could be achieved within a single hyper-CEST acquisition by a CEST- effect up to 70 %. Quantification of the achieved labeling concentration was not done so far. Importantly, the MRI experiment has been performed within the developed bioreactor setup on live cells. The performed experiment was therefore the first demonstration of a targeted biosensor that has been performed in such an advanced cell culture system.

Nevertheless, the used scaffolded biosensor showed aggregation over time. It is assumed that this is consequence of some aging since the sample had been previously prepared at UC Berkeley by Dr. Jabadurai Jayapaul and subsequent shipping and storage could have affected the sensor integrity. Therefore, additional experiments with fresh biosensor batches have to be performed to evaluate the promising initial results.

Further tests, including fluorescence based labeling quantification, are necessary in order to verify the cage labeling efficiency of the scaffolded biosensor. An appropriate method would be quantitative hyper-CEST to reveal the cage pool size for a known concentration of phages in a sample.[124] These quantification experiments are important in order to verify the sensitivity gain that is made by the scaffolding approach in comparison to the modular biosensor design that is easier to realize in terms of synthesis effort as well as target versatility.

Comparable scaffolding approaches can be realized by using other scaffolds such as viral capsids.[114] Specific cell-labeling with such a capsid-based cryptophane biosensor was recently demonstrated by hyper-CEST MRI using aptamers for cell surface labeling instead of antibodies (initial results by Keunhong Jeong et al., presented at ENC 2014).

Nevertheless, it has to be considered, that all antibody-based cell surface labeling experiments performed in this study, were done at an unphysiological temperature of 4 °C. This temperature conditions leads to a breakdown of the cellular activity which also drastically reduces the potential for unspecific binding or cellular internalization of the biosensors. It therefore has to be evaluated in further *in vitro* studies, how the binding specificity of antibody-conjugated xenon hosts gets changed, when cell-labeling is performed at physiological relevant temperature of 37 °C.

Another interesting route aiming for the achievement of high cryptophane amounts per targeting unit is the use of liposomes instead of protein scaffolds. Liposomes can serve as a carrier system for hydrophobic cryptophane-A molecules as they are embedded within lipid bilayers.[101] The liposomes can further be targeted for example by the integration of biotinylated phospholipids, followed by the coupling of antibodies via biotin-avidin interactions. A summary about design strategies for targeted liposomes as well as challenges related to this approach can be found in Ref. [125]. The liposome concept therefore provides a high flexibility for different targets paired with a high cryptophane payload. It is likely that the liposome concept allows for higher cryptophane concentrations per targeting unit when

compared to protein scaffolds. Fist estimation suggested the potential to load approximately 2000 CrA molecules per liposome[118] (calculations based on fluorescence quantification) which is ca. 10 fold more when compared to numbers achieved for protein scaffolds (ca. 300 per bacteriophage unit [75]).
In addition, liposomes are well characterized particles that are suitable for localized drug delivery[126] that may also have preferable *in vivo* characteristics in combination with PEGylation[127]. Therefore, clinically approved (targeted) liposome formulations[128] should be evaluated for their cryptophane loading potential followed by a demonstration of specific cell-labeling with subsequent hyper-CEST detection.

(iii) The last studied biosensor type was designed for imaging of metabolically labeled glycan's based on a bioorthogonal targeting strategy. Glycan's are interesting cell surface targets that are involved in many processes such as cell-cell interactions, embryo development, cancer progression as well as regulation of the immune system.[129–131]
Antibody based labeling of cell surface epitopes such as CD14 (biosensor i) or the EGF receptor (biosensor ii) is a well characterized strategy that has been already used for the successful MRI localization of such targets by using conventional contrast agents.[132] This is not the case for MRI contrast agents aiming for the localization of metabolically labeled glycans. Early as well as more recent MRI studies were not successful[133] therefore raising the question, if molecular imaging of metabolically labeled glycans is achievable with MRI[134].
The biosensor that has been studied along this thesis consists of CrA, fluorescein and a bioorthogonal targeting unit (bicyclo[6.1.0]nonyne) all conjugated to a hydrophilic peptide that serves as a scaffold. Metabolic cell-labeling was achieved by treating cells with Ac_4ManNAz that causes labeling of terminal sialic acids with a functional bioothogonal group (azido-glycans). The biosensor was covalently bound to modified azido glycans via covalent interactions between both bioothogonal groups formed at physiological temperature.
The performance of the new biosensor could be successfully demonstrated within the developed bioreactor setup on live cells. Hyper-CEST MRI allowed the localizing of metabolically labeled cells by a higher hyper-CEST effect (ca. 50 %) when compared to unlabeled cells (ca. 20 %). The data therefore underlines for the first time the potential of hyper-CEST MRI contrast agents to localize molecular targets that are at the moment inaccessible for conventional MRI contrast agents.

3.1.1.3. Specific cell-labeling by cellular internalization

Cell targeting by specific cellular internalization of cryptophane molecules is another route for molecular imaging next to cell surface labeling. For this purpose the cryptophane molecules are connected to targeting units such as peptides or proteins. The targeting unit further cause receptor mediated endocytosis leading to an efficient accumulation of cryptophane within cells. Since each receptor is capable to internalize several cryptophane conjugates, this approach should allow for high labeling efficiency. So far 3 publications (see below) have described such labeling schemes for cryptophane conjugates:

Within the first study, cryptophane has been coupled to an integrin specific RGD peptide leading to integrin receptor mediated cryptophane uptake into NCI-H1975, HFL-1, and CAPAN-2 cells (all integrin-positive).[86] The study was focused on aspects related to the chemical synthesis of the tested conjugates as well as cell physiological characterizations of the labeling procedure. Xenon NMR was not performed since the authors described problems with achieving high cell densities of labeled cells.

Within another study, cryptophane molecules have been grafted on transferrin-proteins. The estimated cryptophane per transferrin ratio was 20 therefore showing the scaffolding potential of such biosensor designs. The transferrin-receptor (TfR) mediated cellular uptake of the cryptophane modified protein into K562-cells (TfR-positive) could be further monitored by xenon NMR spectroscopy.[87] However, MRI localization of labeled cells was not performed.

A recent study demonstrated the use of targeted and cryptophane loaded liposomes, a concept introduced within the previous section.[118] In this context, human brain microvascular endothelial cells (HBMECs) have been specifically labeled with cryptophane loaded liposomes followed by hyper-CEST MRI localization. Cell specificity was achieved by incorporating arginine-rich lipopeptides into the liposome formulation that mediates the liposome uptake into HBME cells.

Importantly, all cell-labeling applications that demonstrated a specific cellular internalization of cryptophane-conjugates have been performed at physiological temperature of 37°C. The approaches are therefore better characterized with respect to there *in vivo* performance when compared to strategies aiming for cell surface labeling with antibodies (not performed at 37 °C so far). Nevertheless, antibody-based cell surface labeling for the purpose of molecular imaging is a promising strategy as demonstrated *in vivo* for MRI and other imaging modalities.[132,135]

3.1.2. Cell-labeling with PFC nanodroplets

Perfluorocarbon (PFC) nanodroplets of the PFOB type have been evaluated as an alternative xenon nanocarrier for cell-labeling applications. This was motivated by affordable synthesis, a higher hyper-CEST sensitivity as well as a different detection frequency for this xenon host when compared to cryptophane-A.[89]

Importantly, PFC nanodroplets are well characterized and clinically approved as contrast agent in ultrasounds, computer tomography as well as ^{19}F-MRI applications.[91] Therefore, cell-labeling properties are already evaluated in detail which allows transferring these known clinical application routes to hyper-CEST MRI. A basis for the transfer of known imaging applications was the demonstration of hyper-CEST detection for PFOB nanodroplets within cellular environments, as it could be achieved as part of this thesis.

3.1.2.1. Unspecific cell-labeling through cellular internalization

Unspecific cell-labeling with intracellular PFOB concentrations in the nM range was demonstrated for L929 fibroblasts followed by the detection of labeled cells by hyper-CEST MRI. Further *in vitro* experiments should aim for comparable demonstrations with cell types that are more relevant for cell-tracking applications such as stem cells and T-cells. Labeling of such non-phagocytic cell types is normally more complicated to achieve and relies on the use of cationic transfection agents.[105]

Within this thesis, a relative simple formulation has been used for the production of the PFOB nanodroplet emulsion.[89] One drawback of this formulation is the instability of the nanodroplet size (increase) over time due to Ostwald ripening.[136] More advanced nanodroplet formulations made of perfluoropolyether (PFPE) mixed with linear polyethyleneimine (PEI) can overcome this size instability.[137] The mentioned nanodroplets had an average size of ca. 200 nm and were stable for more than 100 days. In addition, the produced PFPE nanodroplets have shown to achieve high labeling rates within short incubation times (3 hours) also for non-phagocytic cell lines without the need of transfection agents. Since hyper-CEST detection was so far only demonstrated for PFC nanodroplets formulated from PFOB molecules, it has to be proven whether the same holds true for PFPE based nanodroplets.

In this context, different nanodroplet formulations (including different PFC types and emulsifiers) have to be tested with respect to their droplet stability as well as their cell-labeling efficiency.[10] Further more, it has to be evaluated if such modifications could have any effect on the xenon exchange dynamics and therefore on the hyper-CEST sensitivity. Stevens et al. (2013) suggested “that slowing the xenon exchange rate will enhance contrast on a per agent basis. This may be achieved by incorporating different surfactants such as cross-linking phospholipids or fluorine-containing block copolymers.” [89]

3.1.2.2. Specific functionalization of PFC nanodroplets for cell surface epitopes

Next to cryptophane-A also PFC nanodroplets have to be evaluated upon their targeting potential in combination with hyper-CEST MRI. The technical requirements as well as *in vivo* demonstrations for such targeting approaches are described within several studies and are common for different perfluorcarbon based nanodroplet types such as PFOB, PFDCO (perfluoro-dichlorooctane) and PFCE (perfluoro-15crown-5-ether).[12,94,95,138]

The hydrophobic perfluorcarbon droplets can be decorated with chemically modified lipids such as lipid-conjugated receptor-antagonists or biotinylated phosphatidyl-ethanolamine. Biotinylation enables modular targeting as already demonstrated for cryptophanes. The biotinylated nanodroplets are therefore further conjugated to avidin labeled antibodies for the purpose of cell surface labeling.

Along this thesis initial cell-labeling experiments have been performed with antibody (anti-CD14) modified PFOB nanodroplets (data not shown). Antibody functionalization of the PFOB nanodroplets was done via avidin-biotin interactions as described in Ref. [94]. At first, biotinylated nanodroplets has been produced. Therefore PFOB, lecithin and biotinylated/fluorescence-labeled phosphatidyl-ethanolamine (head groups were modified) has been premixed followed by high pressure homogenization for ca. 15 cycles. The biotinylated nanodroplets were later coupled to avidin conjugated antibodies (anti CD14). Avidin conjugation to anti-CD14 antibodies, biotin-avidin coupling and cell-labeling was done as described for the modular cryptophane biosensors.[109]

Nevertheless, it was not possible to achieve specific binding of the targeted nanodroplets (labeling concentration: 1.6 nM) as evaluated by fluorescence microscopy and flow cytometry (data not shown). CD14-positive RAW 264.7 cells and CD14-negative control cells (3T3) showed comparable labeling intensities. Potential reasons for the lack of specificity are an insufficient nanodroplet functionalization as well as a not optimized cell-labeling and washing procedure.

Therefore, further experiments have to be done to characterize the efficiency of the nanodroplet functionalization in detail. Subsequently, cell-labeling and washing protocols have to be established. In this context it's important to ensure the separation of cell bound and unbound nanodroplets after cell-labeling. This washing step turned out to be crucial within the performed initial experiments and can potentially explain the observation of strong unspecific labeling effects. The mentioned labeling and washing procedures needs to be optimized and compared for surface attached cells (fluorescence microscopy) as well as cells in suspension (flow cytometry) followed by NMR experiments.

In case that specific cell-labeling can be achieved, it should be further evaluated if cell surface labeling with targeted PFOB nanodroplets is more efficient for droplets larger than 200 nm. For large PFOB nanodroplets a higher hyper-CEST sensitivity is expected due to a more efficient saturation transfer.[89]

3.1.3. Cell-labeling with bacterial gas vesicles

Recently, a new xenon host structure gained interest for MRI cell-labeling applications. The xenon host is based on gas vesicles (GV) formed by proteins that are genetically encoded by bacterial gene clusters.[55] The gas vesicles (50–500 nm in size) are formed in several species of waterborne halobacteria and cyanobacteria. Each individual vesicle consists out of multiple copies of the highly conserved protein GvpA while their biosynthesis requires at least eight genes that are contained in GV gene clusters.

Within their study, the authors could demonstrate that xenon diffuses into such purified gas vesicles where it forms a gaseous phase with a distinct chemical shift. Due to a rapid exchange between xenon from within the vesicles and xenon in solution such host structures could be detected by hyper-CEST MRI at picomolar concentrations.

The authors further showed quantitative hyper-CEST imaging of heterologous gene expression in *E.coli* by using a GV gene cluster as MRI reporter gene. "Reporter genes are molecularly engineered tools that enable assessment of location, duration and extent of transcriptional activity of a specific promoter within living cells and whole organisms. Reporter constructs can be used to probe signaling pathways, post-transcriptional modifications, protein-protein interactions, protein stability, translocation and cell trafficking."[139]

The gas vesicles are therefore a quite interesting alternative to synthetic xenon hosts such as cryptophanes or PFC nanodroplets that cannot be genetically encoded. A disadvantage of synthetic cell trackers is a dilution of the cell-internalized contrast agents as a result of ongoing cell division cycles. Their application for long term cell-tracking applications such as the observation of tumor progression or stem cell integration/differentiation is therefore limited. Reporter genes allow overcoming this limitation since the contrast agent can be continuously resynthesized within the cells of interest. For this purpose, the gas vesicle gene cluster has to be stable integrated into the genome of mammalian cells. Although this was not shown so far, the authors claim that the size of the GV gene cluster (6 kilobases) allows for gene transfection and cell-labeling by viral transfection strategies.[140]

Next to the exciting possibility of genetic cell-labeling also conventional strategies such as unspecific and target specific cell-labeling can potentially be achieved with this new type of xenon host. Unspecific cell-labeling can for example be achieved by electroporation although this has not been proven so far.

Nevertheless, the targeting potential of the gas vesicles has been demonstrated within the mentioned study.[55] For this purpose gas vesicles have been expressed, purified and further conjugated onto antibodies via biotin-streptavidin interactions. *In vitro* molecular imaging of HER2 expressing breast cancer cells (SKBR3) has been demonstrated for gas vesicles conjugated to a anti-HER2-antibodys by using hyper-CEST MRI.

It was also recently demonstrated that such gas vesicles can be detected *in vivo* by using ultrasound.[141] The authors performed subcutaneous and intravenous injections of Halo gas vesicles into live

anaesthetized mice and observed no acute toxicity immediately or 48 h after vesicle administration. The vesicles were found to be taken up and cleared by the liver. Although further test concerning the *in vivo* behavior of such gas vesicles are necessary, this shows the potential to inject targeted gas vesicles for molecular imaging applications.

3.1.4. General considerations for cell-labeling

As summarized within this paragraph, unspecific as well as targeted cell-labeling can be achieved with either synthetic (cryptophane-A, PFOB nanodroplets) or genetically encoded (gas vesicles) xenon nanocarriers. The individual xenon hosts show different cell-labeling characteristics (uptake behavior, cell viability) due to their individual chemical composition and size. It is also likely that the *in vivo* behavior (toxicity, body retention, clearance rate, tissue and organ penetration, immune response) of the xenon hosts is different, although this is speculative since detailed *in vivo* studies for cryptophanes and gas vesicles are still pending.

So far PFOB nanodroplets are probably the most promising host structures since they are already well characterized for *in vivo imaging* by different modalities. In addition such nanodroplets can be loaded with drugs which allows for combined therapeutic applications.[142]

For cryptophanes the lack of a detailed *in vivo* characterization can be probably overcome by using liposomes as cryptophane carriers. A recent *in vitro* study showed that cell-labeling with liposome embedded cryptophane-A has no negative effect onto the cellular viability of brain endothelia cells, even at relatively high cryptophane concentrations up to 100 µM.[118] On the other hand, cell-labeling with naked cryptophane-A showed moderate toxicity on L929 cells at lower concentrations (60 µM, shown within this thesis). Although both studies have been performed under different labeling conditions and with different cell types, it's likely that liposome embedding of cryptophane-A masks potential toxic effect and that the *in vivo* behavior will be dominated by the liposomes. The *in vivo* characteristics of PEGylated liposomes are well studied, making them ideal candidates as a cryptophane carrier. In addition such liposome carriers can be loaded with drugs and other contrast agents enabling therapeutic applications paired with the potential for multimodal detection.[143]

The gas vesicles have the outstanding potential to act as genetically encoded reporters, although synthetic nanocarriers may be beneficial for unspecific labeling approaches that are based on simple coincubation. In this context, the type of xenon nanocarrier has to be adapted to the specific needs of potential *in vivo* applications. Moreover, the synthesis effort for the individual hosts has to be considered. Given this, PFOB nanodroplets are preferable since they are cheap and need no time intensive chemical synthesis such as cryptophanes or heterologous expression and purification such as gas vesicles.

3.2. *In vitro* hyper-CEST detection of labeled cells

3.2.1. Single-type cell-labeling

An important issue next to the demonstrated possibility to label cells with xenon nanocarriers is the achievable MRI contrast per labeled cell. The hyper-CEST sensitivity for the detection of labeled cells is determined by a combination of:

(i) The number of xenon nanocarriers per cell that can be achieved by a certain labeling scheme.
(ii) The hyper-CEST sensitivity of the used xenon nanocarriers within a specific cellular environment.

hyper-CEST contrast agent	cell type (pos./neg.)	labeling efficiency (pos./neg.)	cell density [mill/mL]	saturation chem. shift [ppm]	saturation parameter [µT, sec]	contrast (pos./neg.) [%]	Xe del.
			Cell-tracking				
CrA	L929	40/- µM	20	70	10, 10	80/0	P
CrA-FAM	L929	15/- µM	10	71	18, 20	70/0	P
PFOB	L929	80/- nM	20	107	10, 10	80/0	P
			Targeted molecular imaging				
CrA-M13-EGFR	MDA-MB/Jurkat	-	15	70	30, 20	70/10	P
CrA-BCN	HEK293	120/40 nM	10	68	30, 26	50/15	P
CrA-CD14	RAW/3T3	150/20 nM	5	70	30, 26	80/20	D
CrA-li-P2Rn*	HBMEC/HEoEC	4/1 µM	0.8	71	15, 20	70/25	D
GV-HER2*	SKBR3/Jurkat	-	80	31	23, 6.5	80/0	D

Table 1: Hyper-CEST MRI characteristics of *in vitro* cell-labeling studies with xenon nanocarriers (hyper-CEST contrast agents). The cell-labeling studies were classified into cell-tracking experiments with untargeted contrast agents and targeted molecular imaging experiments with functionalized contrast agents. Contrast agents are abbreviated as introduced within this thesis or given within the main text below. Constructs that were not studied along this thesis are labeled (*) Xe del.: used xenon delivery strategy, P: indirect perfusion/bioreactor setup, D: direct bubbling.

Table 1 summarizes the hyper-CEST MRI characteristics of *in vitro* cell-labeling studies with xenon nanocarriers that have been performed. Successful MRI detection was achieved for cells that have been unspecifically labeled with either CrA or PFOB as an example for cell-tracking applications.
MRI detection of specifically labeled cells as an example for targeted molecular imaging applications was achieved for 3 different biosensors (CrA-M13-EGFR, CrA-BCN and CrA-CD14) that are all based on cryptophane conjugates. Additionally, 2 biosensors are listed that were not studied within this thesis (a liposome-cryptophane biosensor targeting HBMEC cells: CrA-li-P2Rn[118] and a gas vesicle based biosensor targeting HER2 receptors on SKBR3 cells: GV-HER2[55]) to summarize all achievements within the field so far.

In case of unspecific cell-labeling, high contrast (ca. 80 % CEST effect) could be achieved for L929 cells that have been labeled with either CrA or PFOB at comparable high cell densities (20 million cells/mL). Unlabeled cells gave no contrast at all.
The individual hyper-CEST sensitivities for both contrast agents are quite different (nM for CrA, pM for PFOB) as demonstrated by spectroscopy within test solutions without performing cell-labeling. [89],[70] On the other hand, cryptophane based cell-labeling achieves much higher intracellular concentration (µM) when compared to PFOB (nM) therefore compensating for the lower sensitivity per xenon hosts. Systematic studies are necessary to further evaluate the hyper-CEST contrast for PFOB and CrA labeled cells at different saturation conditions. It has to be evaluated if one of the xenon hosts shows preferable saturation behavior in cellular environments, especially at short saturation times (1-4 sec). Such short saturation times are necessary for *in vivo* experiments with expected short hyperpolarization lifetimes for xenon (T_1-values) ranging from 4 to 16 seconds.[144,145]
Such experiments have to be performed with stem or immune cells with relevance for clinical cell-tracking applications while considering improved labeling schemes as mentioned earlier. In addition, these experiments have to be performed within perfused bioreactor setups as developed within this thesis since stem/immune cells are very sensitive and most likely not suitable for experiments with direct xenon delivery.

In case of specific cell-labeling with targeted biosensors the performed studies are quite versatile. The studies include: cell surface labeling with antibody conjugated cryptophanes (CrA-CD14) or gas vesicles (GV-HER2), bioorthogonal cell surface labeling with cryptophanes (CrA-BCN) as well as examples for scaffolded cryptophane biosensors using either liposomes (CrA-li-P2Rn) or bacteriophages (CrA-M13-EGFR). Comparing the sensitivity performance of the studied labeling approaches is complicated because:

(i) The studied cell types and therefore the number of targets per cell are different.
(ii) The used cell densities are not comparable (ranging from 0.8 to 80 million cells/mL).
(iii) The applied saturation parameters are different.
(iv) For some examples labeling quantification could not be achieved.

Nevertheless, high contrast for target-positive cells (50-80 % CEST effect) was achieved within all experiments while control cells gave only low contrast (0-25 %) as a result of unspecific binding. Further studies should aim for a comparison of the mentioned biosensor approaches (including targeted PFC nanodroplets) by keeping the listed parameters (cell-/target type, cell density, saturation parameters, xenon delivery strategy) constant. The aim in this context is to verify the biosensor approach that produce the highest hyper-CEST contrast per cellular target for single-type labeling applications while keeping the synthesis effort as well as the biocompatibility in mind.

Further experiments including targeted as well as unspecific labeling should also aim to characterize the minimal amount of labeled cells that can be detected under *in vivo* like hyper-CEST conditions. The following considerations are important:

(i) The saturation parameters should include a pulse strength that is at the maximum tolerable *in vivo* value (ca. 50 µT continuous wave irradiation[89]), as well as saturation times that are shorter than the T_1 of hp-xenon *in vivo* (< 4 sec).

(ii) The experiments should be performed in a bioreactor setups working under perfusion with xenon saturated liquids to maintain the viability of sensitive cell types.

While keeping this in mind, the density of labeled cells has to be subsequently reduced until a MRI contrast threshold of ca. 30 % is reached. For biosensor applications with expected unspecific binding to control cells the contrast should be calculated as the difference between the contrast for positive and negative cells. The determination of the minimal detectable cell number is important to further motivate the hyper-CEST technique with respect to other imaging modalities that do not rely on comparable complicated hyperpolarization procedures.

3.2.2. Multi-channel cell-labeling

The simultaneous detection of multiple contrast agents (multi-channel/multiplexed detection) is a challenging goal for imaging modalities with clinical relevance including PET, SPECT and MRI. The application range for multi-channel detection includes the simultaneous tracking of different *ex vivo* labeled cell lines with relevance for studying cellular immunotherapy [146] as well as tumor profiling with targeted tracers [6].

In contrast, optical imaging easily allows for sensitive multi-channel detection of several tracers at different wave lengths but its use is constrained to preclinical experiments with small animals since light within the required spectral range is strongly scattered by tissue.[147,148] MRI overcomes this limitation by using radio waves with unlimited penetration depth. While conventional relaxivity-based MRI contrast agents are restricted to the detection of a single type of tracer molecules, it is possible to encode multiple tracers within the chemical shift dimension when using saturation transfer based detection such as hyper-CEST.[149] Encoding within the chemical shift dimension requires a sufficient chemical shift difference of xenon within the used xenon host structures (ca. 30 ppm) to allow for a host-specific saturation transfer without spillover effects. This is an important consideration due to the expected broadening of each CEST peak as a consequence of relaxation effects, magnetic field inhomogeneity as well as the use of strong saturation pulses likely to occur *in vivo.*[102]

Within this thesis such multi-channel MRI detection of L929 fibroblasts that have been unspecifically labeled with either CrA or PFOB could be demonstrated as a proof of principle.

The multi-channel concept can be translated to experiments with relevance for cell-tracking or molecular imaging applications. In case of multi-channel cell-tracking such a translation would require the labeling and detection of two different cell types.

Importantly, the chemical shift for cell internalized CrA (ca. 70 ppm) is independent from the cell type as it has been shown for fibroblasts (L929), macrophages (RAW) or brain endothelial cells (HBMEC).[99,118] This observation is underlined by the fact that the same chemical shift is observed for CrA in phospholipid membranes that serve as cellular model systems.[88,101] Although this was not proven so far, it is likely that the chemical shift for cell internalized PFOB (ca. 107 ppm for L929 fibroblasts) is also cell type independent. Since practically all cell types can be labeled with either PFOB or CrA the concept can be used to perform multi-channel cell-tracking of variable cell type combinations.

The demonstrated concept can be also translated to molecular imaging applications with targeted CrA and PFOB. As it can be seen in table 1, the chemical shift for cell surface-bound CrA is ca. 70 ppm independent from the applied biosensor concept (scaffolding, liposome embedding). Once again, it is likely that the same holds true for PFOB nanodroplets despite no experimental validation has been performed.

Further experiments therefore should aim to verify this proposed translation by performing comparable *in vitro* experiments aiming for the multi-channel detection of:

(i) Two different cell types based on unspecicically labeling with PFOB and CrA.
(ii) Two different cellular targets based on specific labeling with PFOB- and CrA biosensors.

While the chemical shift of entrapped xenon for nanoemulsion droplets is so far only reported for PFOB (120 ppm), various cryptophane-types are known that cover a broad chemical range of ca. 30 ppm.[57] A detailed characterization of their individual cell-labeling capabilities as well as hyper-CEST properties could allow expanding the repertoire of available cryptophane based cell-trackers or biosensors. Importantly, multi-channel MRI labeling of mammalian cells can probably also be realized by combining other xenon hosts that have the potential to label cells. One example was recently given by Shapiro and coworkers (2014).[55] In the already mentioned work, the authors could show that bacterial gas vesicles derived from different bacterial species are characterized by unique resonance frequencies for entrapped xenon as a consequence of differences within vesicle size and shape. They further performed multiplexed MRI detection of three different gas vesicle types that were characterized by resonance frequencies of ca: 15 (GV from *E.coli*), 30 (GV from *Microcystis*) and 50 ppm (GV from *Halobacteria*). Although this multiplexing concept could not be demonstrated for labeled mammalian cells, it offers the possibility for such applications by either using gene transfection or active targeting as explained within the previous section. The multiplexed detection of different gas vesicles types can be further paired with the multiplexed detection of cryptophane-A and PFOB nanodroplets. Such a combination would already allow for the multiplexed hyper-CEST detection of 5 different xenon hosts next to each other, since their individual resonance frequencies are well dispersed along the xenon chemical shift range.

3.3. Translation of the concept to preclinical *in vivo* studies

The presented work was motivated by the need for novel medical imaging techniques that help to improve the early detection and treatment of widespread diseases such as cancer. While modern clinically approved techniques such as combined PET/CT scans allow for the applications of sensitive and cell-specific contrast agents, they come with limitations due to the health risks related to nuclear medicine itself.

MRI as an alternative imaging technique that suffered for a long time from the inherent low sensitivity of conventional contrast agents. This restricts especially molecular imaging applications which hold promise for the early detection of abnormal cellular structures in the future. Hyperpolarized xenon MRI is one possibility to overcome this limitation while xenon nanocarriers are ideal contrast agents since their indirect detection by hyper-CEST combines high sensitivity (nano- to picomolar concentrations) with the potential for functionalization, multiplexed detection and even genetically encoding. The *in vitro* characterization of the MRI cell-labeling potential of xenon based contrast agents has emerged rapidly within the last years as demonstrated and summarized within this work.

Although the recent developments are quite promising, a major challenge within the field will be to translate the concept of hyper-CEST based MRI cell-labeling to initial preclinical experiments with small animals. To date, two of the three prerequisites for a successful *in vivo* demonstration are given, which are: *in vivo* MRI of dissolved hp- xenon as a sensing medium for xenon nanocarriers and the *in vitro* characterization of the cell-labeling and sensitivity potential of xenon nanocarriers.

The demonstration of the hyper-CEST detection of xenon nanocarriers *in vivo* is still elusive. Within a recent publication by Shapiro and coworkers[55] the feasibility of such *in vivo* detection has been simulated based on a combination of data concerning the achievable concentration of hp-xenon within mouse brain, the sensitivity for xenon nanocarriers of the gas vesicle type as well as hyper-CEST and MRI parameters that are consistent with the relaxation behavior of hp-xenon *in vivo*. Based on this simulation, it has been suggested, that xenon nanocarriers of the gas vesicle type can be detected at 400 pM in brain tissue by a 75 % hyper-CEST effect. Considering the higher hyper-CEST sensitivity of the gas vesicles when compared to PFC nanodroplets or scaffolded cryptophanes, it is likely that the *in vivo* detection of such synthetic nanocarriers at nanomolar concentrations is feasible.

An initial experimental validation of *in vivo* hyper-CEST MRI can for example be done for untargeted xenon nanocarrier that are injected into the mouse brain in order to validate the achievable sensitivity for the known nanocarrier types. More advanced test should aim for first cell-tracking experiments with *ex vivo* labeled cells in brain. In parallel, the feasibility for molecular imaging should be tested by the administration of targeted and fluorescence labeled xenon nanocarriers, while first experiments can for example characterize the achievable *in vivo* specificity and labeling concentration by *in vitro* tests with extracted tissue or organs. Next to this, detailed toxicological animal studies should be performed to exclude potential side effects for different application routes of the contrast agents. Finally, *in vivo* molecular imaging with targeted xenon nanocarriers should be demonstrated which is

probably the most critical step based on the low concentrations of disease relevant targets such as cell surface epitopes. A successful demonstration of molecular imaging *in vivo* is essential in this context in order to meet the requirements of a potential new medical imaging concept. The challenges related to such an *in vivo* translation requires the pairing of different scientific disciplines including medicine, physics, chemistry and biochemistry as well as the collaboration of laboratories worldwide. The field of MRI with hyperpolarized xenon therefore goes into an exciting future.

4. Methods and Materials

4.1. Delivery of hp-xenon for *in vitro* cell experiments

4.1.1. Xenon hyperpolarization

A custom-designed continuous-flow xenon hyperpolarizer was used to produce hp-^{129}Xe by spin-exchange optical pumping.[46] The xenon hyperpolarizer works with active cooling of the pumping cell for an efficient prevention of rubidium runaway.[150] Detailed information about the hyperpolarizer design as well as the optimization of polarization conditions can be found in Ref. [45]. The used gas mixture consists of 5 % Xe (26.4 % natural abundance of ^{129}Xe), 10 % N_2 and 85 % He while the achieved ^{129}Xe spin polarization was approximately 25 % at a gas flow rate of 0.1 SLM.

Using the pressure from the polarizer (3.5 bar overpressure), the mix was either directly bubbled into the sample solution by using a spectrometer triggered bubble dispenser[74] or it was delivered indirectly by means of an NMR/MRI compatible bioreactor setup working under continuous perfusion with hp-xenon saturated medium[78].

4.1.2. Strategies for the delivery of hp-xenon

4.1.2.1. Direct xenon delivery

Hyperpolarized xenon was directly bubbled into cell suspensions/media via fused silica capillaries (Polymicro Technologies, Molex Incorporated, Caudebec les Elbeuf, France) while foam formation was reduced by the addition of 0.02-0.1 % anti-foam agent as suggested by Matt Ramirez (pluronic® L81, BASF corporation, Ludwigshafen, Germany). By using spectrometer-triggered gas flow regulators (mass flow controllers, Omega Newport, Deckenpfronn, Germany) hyperpolarized xenon was either bubbled into the sample solution (0.1 SLM) or it was guided through a bypass line during signal acquisition (0.25 SLM) (figure 4.1). Detailed information about the used bypass design can be found in Ref. [45]. For each scan xenon was bubbled for 8-15 sec followed by a 2 sec delay to allow remaining bubbles to collapse before signal acquisition. The bubbling time was optimized for each experiment individually according to the foaming behaviour of the sample solution.

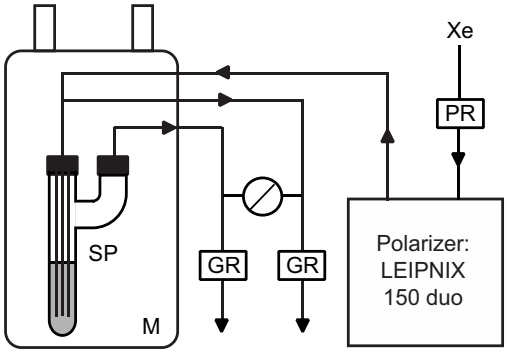

Figure 4.1: Setup for direct delivery of hp-xenon by gas dispersion. SP: sample phantom; M: magnet; PR: pressure regulator; GR: gas flow regulator.

The effect of the bubbling procedure onto the cellular viability of L929 fibroblasts and RAW 264.7 macrophages was studied by Dr. Honor May Rose. Experimental details can be found in Ref. [99]. In brief: Samples of both cell lines (10 million cells/mL) were transferred into the NMR phantom followed by xenon delivery at characteristic experimental conditions (50 xenon redelivery steps with 10 sec bubbling each). Samples of 1 million cells were taken at the beginning of the experiment (control) and after xenon delivery. Cells have been stained with 7-AAD (7-Aminoactinomycin D) (Life Technologies) viability dye prior to analysis by flow cytometry. The median fluorescence intensity of 7-AAD was measured on the FL3 channel and compared under identical acquisition parameters for each cell line. Flow cytometry for 10,000 events was performed on a BD FACSCalibur flow cytometer using BD CellQuest Pro Acquisition software. Data were then analyzed with FlowJo analysis software.

4.1.2.2. Indirect xenon delivery (bioreactor)

An NMR/MRI compatible packed-bed bioreactor was designed to overcome limitations of direct xenon bubbling. Xenon leaving the polarizer (3.5 bar overpressure) was bubbled continuously (0.56 SLM) into a home-built chamber made of Teflon sitting upstream of the sample phantom (figure 4.2). This chamber was continuously perfused (10 mL/min) with cell culture medium (Hanks balanced salt solution/HBSS, H1641, Sigma Aldrich, Taufkirchen, Germany) while the inflow was regulated by a liquid flow controller (mass flow controllers, Omega Newport, Deckenpfronn, Germany) connected to a medium reservoir pressurized to 4.5 bar. It is important to use a medium that contains a low calcium ion concentration such as HBSS (1.3 mM $CaCl_2$) to avoid de-gelling of the perfused alginate beads (calcium ions are necessary for alginate matrix formation).

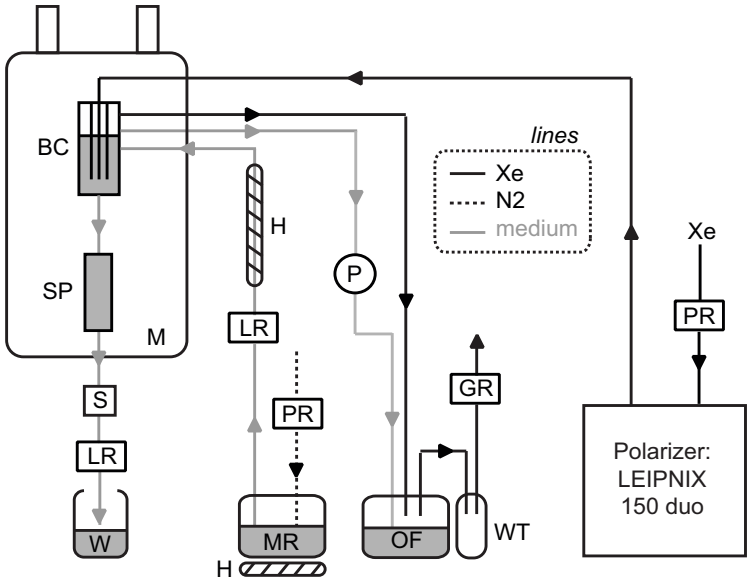

Figure 4.2: Continuous-flow bioreactor setup for indirect delivery of hp-xenon. The sample phantom gets perfused with hp-xenon enriched medium. The dissolution of xenon takes place within a bubbling chamber sitting upstream the sample phantom. BC: bubbling chamber; SP: sample phantom; M: magnet; S: in-line sensors for temperature, pH and dissolved oxygen; LR: liquid flow regulator; W: waste tank; H: heating device; MR: medium reservoir; PR: pressure regulator; P: high pressure pump; GR: gas flow regulator; WT: water trap; OF: overflow tank.

A high pressure pump (Masterflex L/S: 77250-62, 07523-80, Novodirect GmbH, Kehl/Rhein, Germany) keeps the liquid level into the bubbling chamber constant (pumping rate: 10 mL/min). The xenon gas flow was regulated by a mass flow controller connected to the overflow tank. Temperature, dissolved oxygen content as well as pH of the medium were monitored via in line sensors sitting downstream of the sample phantom (VISIFERM DO 120, EASYFERM Plus ARC 120, Hamilton Messtechnik GmbH, Höchst, Germany). Temperature regulation within the phantom was realized via a heated tubing close

to the inlet of the bubbling chamber (MIL-HPG-100S, DN04 PTFE, MiL Heating Systems GmbH, Ubstadt-Weiher, Germany). Medium flow through the sample was regulated by an additional mass flow controller at the medium outlet that was triggered by TTL signals from the NMR spectrometer.
For each scan the sample was perfused with xenon saturated medium for 60 sec at a flow rate of 7.5 mL/min. After xenon delivery the medium flow through the sample was temporally stopped for NMR saturation (in case of hyper-CEST) and signal acquisition.

4.2. Synthesis and preparation of xenon nanocarriers

4.2.1. Cryptophanes-A and conjugates

Cryptophane-A monoacid (CrA or CrA-ma) has been purchased from Kangyuan Jiyi Inc. All cryptophane conjugates have been synthesized by colleagues or collaboration partners (see below) starting from CrA as a building block.

Cryptophane-A-Fluorescein (CrA-FAM):
CrA-FAM has been synthesized by Federica Rossella and Dr. Jabadurai Jayapaul by utilizing Fmoc-solid phase peptide synthesis technique as described in Ref. [99].
In brief: The construct was synthesized starting from H-Gly-ClTrt resin (0.63 mmol/g glycine loading (1 mol.eq, Merck Millipore KGaA, Schwalbach, Germany)), which was conjugated to the fluorescent building block (Fmoc-Lys (5-FAM)-OH (2 mol.eq), Mobitec GmbH, Göttingen, Germany) using COMU (2 mol.eq)/DIPEA (4 mol.eq) as coupling agents (Sigma Aldrich). To increase hydrophilicity of the construct and to avoid undesired interaction with the Cryptophane-A, Fmoc-NH-PEG3-COOH (2 mol.eq, ChemPep Inc. Wellington, USA) was used as a spacer and coupled to the sequence as described above. The Fmoc groups on the peptide were removed using 25 % piperidine in DMF during intermediate steps and prior to cleavage from resin. The as-synthesized peptide sequence was cleaved from resin by treating them overnight with TFA/TIS/H_2O (95/2.5/2.5 v/v %) mixture, followed by purification using a reverse-phase HPLC (varitide RPC, 200 Å, 6 µm, 10 x 250 mm) and H_2O/CH_3CN with 0.1 % TFA as gradients. As a final step, the sequence was conjugated to the carboxylic unit of the CrA-ma in solution. The final fluorescent construct was purified using reverse-phase HPLC technique as shown above and structure was confirmed by MALDI-TOF spectrometry.

Cryptophane-A-M13-EGF (CrA-M13-EGFR):

CrA-M13-EGFR has been synthesized by Dr. Jabadurai Jayapaul in cooperation with Prof. David Wemmer and Prof. Matthew Francis from University of California, Berkeley.

CrA coupling onto M13-bacteriophages with binding specificity for EGF receptors (M13-EGFR) was done according to a modified protocol published in Ref. [114]. The protocol described the coupling of CrA onto EGF-specific fd-bacteriophages. The same coupling strategy has been applied for EGF-specific M13-bacteriophages. In brief, the protocol is as follows:

M13-bacteriophages with EGFR binding specificity (M13-EGFR) were generated by standard phage display techniques and provided by Prof. Jim Marks, University of California, San Franciso. The major coat proteins (p8) of M13-EGFR were ketone-labeled by transamination of their N-termini by using pyridoxal 5′-phosphate. Ketone-labeled M13-EGFR were purified and conjugated to aminooxy-functionalized CrA-peptides by using oxime ligation (for 24 hours at RT). The final biosensors (CrA-M13-EGFR) were purified by gel filtration. Synthesis quality has been analyzed by reverse-phase HPLC and MALDI-TOF.

Cryptophane-A-biotin-avidin-anti-CD14 (CrA-CD14):

CrA-CD14 was synthesized by Federica Rossella and Dr. Honor May Rose. All details can be found in Ref. [109]. In brief, the following protocol was applied:

Monoclonal anti-CD14 specific antibody (ABIN 1176993; antibodies-online GmbH) was conjugated to avidin using the EasyLink Avidin Conjugation Kit (ab102860; Abcam) according to manufacturer's instructions. Unbound avidin was removed by size exclusion using an Amicon Ultra 15, 100-kDa concentrator (Merck Millipore). The CrA–biotin module was synthesized using microwave)-assisted acylation to connect CrA monoacid (provided by Kangyuan Jiyi Inc.) with Biotin-PEG3-amine (ChemPrep). The avidin-antibody conjugate was incubated with a 40-fold mole excess of biotin conjugates (ratio of fluorescein–biotin (Thermo Scientific) to CrA–biotin was 1:4) for 30 min at room temperature. The final biosensor (CrA-CD14) was purified from unbound biotin-conjugates by size exclusion (Amicon Ultra 15, 100-kDa concentrator).

Cryptophane-A-bicyclo[6.1.0]nonyne (CrA-BCN):

CrA-BCN has been synthesized by Dr. Vera Martos. Details about the synthesis can be found in Ref. [115]. In brief, the protocol reads as follows:

The CrA-BCN biosensor consists of CrA, fluorescein and a bioorthogonal targeting unit (bicyclo[6.1.0]nonyne/BCN, SynAffix) all conjugated to a hydrophilic peptidic scaffold. The used synthetic strategy was based on the acid labile Sieber amide resin, orthogonal protecting groups and sequential modular couplings. 5,6-carboxyfluorescein, was attached on solid support. The peptide was elongated and terminated with a short PEG-linker. Peptide cleavage under mild acidic conditions generated a free N-terminus, to which CrA was coupled in solution. Finally succinimidylactivated BCN was attached to a unique free lysine side chain of the peptide scaffold.

4.2.2. PFOB nanodroplets

The PFOB nanoemulsion has been prepared similar to the procedure described by Pines and co-workers.[89] In brief, 420 µL PFOB (Sigma-Aldrich) and 315 µL Pluronic F-68 (100 mg/mL, Sigma-Aldrich) have been mixed within 10 mL of purified, deionised water. The mixture was emulsified by high-pressure homogenisation (EF-C3 Avestin Emulsiflex) at a working pressure of 1500 bar (sample was kept in an ice bath while being processed). The nanoemulsion was finally sterile filtrated (0.2 µm syringe filter) and stored undiluted at 4 °C prior to use. After preparation the mean nanodroplets diameter was around 200 nm as analyzed by dynamic light scattering (droplet concentration: 16 nM).

PFOB nanodroplets were fluorescence labelled (PFOB-DiI) by incubation with lipophilic dialkyl-carbocyanine (Vybrant® DiI, life technology's) for 1 h at 37 °C under agitation (10 µL DiI / 1 mL PFOB nanoemulsion).[104] Unbound dialkylcarboxycyanine was removed from the nanoemulsion by centrifugation (1500 g, 20 min).

4.3. MRI cell-tracking with non-targeted xenon nanocarriers

4.3.1. Cell culture, cell-labeling and sample preparation

Mouse fibroblasts (L929) were cultivated as monolayers in DMEM (Sigma Aldrich, Taufkirchen, Germany) supplemented with 10 % FBS (Sigma Aldrich, Taufkirchen, Germany) under standard cell culture conditions (37 °C, 5 % CO_2). The cells were unspecifically labeled with the tested contrast agents (CrA/CrA-FAM, PFOB/PFOB-DiI) by coincubation. The tested contrast agents were diluted in DMEM (10 % FCS, 1 % DMSO).

Experiments with cell suspensions:

For NMR/MRI experiments with cells in suspension, L929 fibroblasts were labeled as monolayers (incubation conditions given within the results section) after reaching 30-40 % confluency. After labeling, the incubation medium has been removed. Cells were washed in PBS (3 times) before they were harvested by standard trypsination. The labeled cells were further resuspended in 2 mL of fresh DMEM without FCS (final cell concentrations are given within the results section). The cell suspension was kept on ice prior to the NMR/MRI experiments.

Experiments with encapsulated cells:

For NMR/MRI experiments with alginate-encapsulated cells, the labeling scheme differs for each of the tested contrast agents:

In case of CrA and CrA-FAM, cells were immobilized within alginate beads prior to labeling. After encapsulation the cells were transferred into spinner vessels (stirring speed: 30 rpm) and incubated with 50 µM CrA/CrA-FAM for 18 hours.

In case of PFOB, fibroblasts were first labeled as monolayers with 1.6 nM of a PFOB nanoemulsion for 18 h (diameter: 200 nm). After PFOB-labeling, the incubation medium has been removed. Cells were washed in PBS (3 times) before they were harvested by standard trypsination. The labeled cells were further resuspended in 2 mL of fresh DMEM without FCS (final cell concentrations are given within the results section) before alginate encapsulation.

4.3.2. Cell immobilization by alginate encapsulation

Cell encapsulation was done as described in Ref. [151]. Cells (10 to 20 million) have been washed (3 times) and re-suspended in 1 mL modified Hank's Balanced Salt Solution without $CaCl_2$ and $MgSO_4$ (modified HBSS, H4641, Sigma Aldrich). The suspension of cells was further mixed with 1 mL of modified HBBS containing 2 % alginate (alginic acid sodium salt from brown algae, Sigma Aldrich) and 2 % mannitol. The cell-alginate solution (10 to 20 million cells/ mL, 1 % alginate, 1 % mannitol in modified HBBS) was trickled into a solution containing 1.5 % $CaCl_2$ and 1 % mannitol by the use of a custom made droplet generator[97]. Polymerization was done for ca. 30 min under agitation at 4° C. The beads size (diameter of 1 mm) was controlled by the gas pressure at the droplet generator (ca. 1.5 bar). The alginate beads were washed (3 times) and resuspended in HBBS, 1 % mannitol and stored at 4°C before they were further used.

4.3.3. Verification of cell-labeling

4.3.3.1. Fluorescence microscopy

Fluorescence microscopy of surface-attached cells:

L929 cells (400000) were grown for 18 h on 30 mm glass coverslips (pretreated with 100 µg/mL poly-L-lysine) in 6-well plates. The immobilized cells were incubated with the respective fluorescence probe (CrA-FAM, FAM-PEG, PFOB-DiI) dissolved in DMEM, 10 % FCS, 1 % DMSO. Labeling conditions (temperature, concentration, incubation time) are given within the results section. After labeling, the incubation medium has been removed. Cells were washed with PBS (3 times) and supplied with fresh DMEM.

Fluorescence microscopy of encapsulated cells:

Cell encapsulation and labeling with either CrA-FAM or PFOB-DiI was done as described within the previous section. For microscopy, alginate beads were transferred into 6-well plates and resuspended in fresh DMEM. Dead cell staining was done by using Ethidium homodimer III (PromoCell GmbH, Heidelberg, Germany) according to manufactures instructions.

Imaging was done on a LSM 510 (Carl Zeiss Microimaging GmbH, Jena, Germany) microscope using an x 100/1.3 numerical aperture oil objective or an 63/1.2 numerical aperture water objective for static cells. For encapsulated cells, an x 10/0.3 numerical aperture water objective has been used. Fluorescence signals were recorded using the following lasers: a 488 nm argon laser/ BP 505-550 nm for CrA-FAM/FAM-PEG or a 543 nm HeNe laser/LP 560 nm for PFOB-DiI/EthD-III. Images were processed using ZEN 2009 light Edition (Carl Zeiss Microimaging GmbH).

4.3.3.2. Uptake quantification

The achieved intracellular concentrations of both studied contrast agents (CrA, PFOB) within L929 fibroblasts was determined by measuring their fluorescence intensity in cell lysates.[86] To do so, L929 cells have been incubated with fluorescence-labeled versions of both contrast agents under the optimized incubation conditions (18 h, 37 °C) identical to the respective MRI experiment (CrA-FAM: 50 µM, PFOB-DiI: 1.6 nM / diameter: 200 nM). Cells were incubated as monolayers with either PFOB-DiI or CrA-FAM dissolved in DMEM, 10 % FCS, 1% DMSO. Cell lysates were made by suspending cells in Lysation-buffer (1 % Triton, 2 % SDS in PBS) for 30 min at 4 °C. A calibration curve (fluorescence intensity vs. concentration) for CrA-FAM and PFOB-DiI in Lysation buffer was used for quantification. Fluorescence measurements were performed on a Safire Micro plate reader (TECAN Deutschland GmbH, Crailskirchen, Germany).

For calculations, several simplifications have been made: The cell-averaged concentration of both contrast agents was estimated for a cell volume that was measured to be 3300 fL for spherical L929 fibroblasts in alginate. As shown within results part: "Hyper-CEST spectroscopy within a perfused bioreactor" the uptake of unmodified CrA is ca. 2.5 fold higher compared to the fluorescence labeled construct CrA-FAM due to a higher hydrophobicity. Based on a measured intracellular CrA-FAM concentration of 15 µM, the concentration of CrA is ca. 40 µM. For PFOB, a stable droplet size of 200 nm following cellular internalization was assumed. It has been further implied that labeling of PFOB with fluorescence dye DiI has no effect on the uptake of the nanodroplets. The intracellular concentration of PFOB is 80 nM in this case. The given concentrations are the mean value of three independent experiments.

4.3.3.3. Viability assessment

The cellular viability of L929 fibroblasts at increasing CrA/CrA-FAM concentrations was probed using the alamarBlue® Cell Viability Assay (Life Technologies, Darmstadt, Germany) according to the manufacturer's protocol. In brief, L929 cells were grown in 96 well plates (2000 cells/well) for 48 h followed by 20 h incubation with CrA-FAM (0-100 µM) or CrA (0-100 µM) at 37 °C. Both probes were dissolved in DMEM, 10 % FCS, 1 % DMSO. After CrA/CrA-FAM incubation, alamarBlue® was added (1:10) and incubated for further 3 h. Fluorescence intensity was measured using a Safire Micro plate reader (TECAN Deutschland GmbH, Crailskirchen, Germany).

Additional cell uptake quantification and cell viability assessment at increasing CrA-FAM concentrations (0 to 100 µM) following incubation for 20 h at 37 °C has been performed for macrophages and fibroblasts in parallel to study cell type influence. The data were generated by Federica Rossella and Dr. Honor May Rose. Detailed experimental procedures can be found in Ref. [99]. In brief: Mouse L929 fibroblasts were grown in VLE/Dulbecco's modified eagle medium (VLE-DMEM) with stable glutamine (FG 1445, Biochrom AG) and 10 % fetal bovine serum (FBS) (S0615, Biochrom AG). Mouse RAW 264.7 macrophages were grown in Roswell Park Memorial Institute medium (RPMI) 1640 with stable glutamine (FG1215, Biochrom AG) supplemented with 10 % FBS (S0615, Biochrom AG). Both cell lines were cultivated under standard conditions (5 % Co2, 37°C). Uptake quantification was done by fluorescence quantification of cell lysates (labeled cells) as described before. Viability assessment was done using the alamarBlue® Cell Viability Assay (Life Technologies, Darmstadt, Germany) according to the manufacturer's protocol as already described.

The cellular viability of L929 fibroblasts at increasing PFOB/PFOB-DiI concentrations (8 nM, 3 nM, 1.6 nM, 0.8 nM) was probed by Trypan Blue staining. Cells were incubated with the nanodroplets dissolved within cell culture medium (DMEM, 10 % FCS) for 20 hours under standard incubation conditions (37 °C, 5 % CO_2). Following incubation cells were harvested, stained with 0.5 % Trypan Blue (Biochrom AG) and analyzed on a TC20™ Automated Cell Counter (Bio-Rad) according the manufactures protocol.

4.4. Molecular MRI with targeted xenon nanocarriers

4.4.1. A modular cryptophane biosensor targeting CD14

Cell culture, cell-labeling and fluorescence quantification (flow cytometry) was done by Dr. Honor May Rose as described in Ref. [109]. In brief, the following protocols are:

Cell culture:

NIH/3T3 fibroblasts (ATCC CRL-1658) were grown in low endotoxin-DMEM with stable gluatmine (Biochrom AG) and 10 % (vol/vol) FBS (Biochrom AG). RAW 264.7 macrophages (Sigma-Aldrich) were grown in RPMI 1640 with stable glutamine (Biochrom AG) supplemented with 10 % (vol/vol) FBS. Both cell lines were grown under standard cell culture conditions (37°C, 5 % CO2). RAW 264.7 macrophages (ca. 70 % confluency) were stimulated for 18 h with 100 ng/mL LPS from Escherichia coli 0111:B4 (Sigma-Aldrich) in RPMI 1640 with stable glutamine and 10 % (vol/vol) FBS.

Cell-labeling and sample preparation:

Ca. 10 million cells were harvested washed and resuspended within a labeling solution of DPBS (Biochrom AG) containing 3 % (wt/vol) BSA and 20 µg of the CD14 biosensor construct. Incubation was done for 1 h in the dark at 4 °C. Following the incubation, the cells were pelleted by centrifugation (400 × g for 4 min at 25 °C) and washed twice with ice-cold DPBS containing 3 % (wt/vol) BSA. Cells used for further experiments had >95 % viability as assessed by Trypan Blue staining (Biochrom AG) using a TC20 Automated Cell Counter (Bio-Rad). The labeled cells were resuspended in PBS (5 million cells/mL). The cell suspension was transferred to an NMR double compartment phantom (a 5 mm NMR tube inserted into a 10 mm NMR tube) and analyzed by hyper-CEST NMR/MRI with direct xenon delivery. The RAW 264.7 cell suspension was filled into the inner tubing while the 3T3 cell suspension was filled into the outer compartment.

Flow cytometry:

After cell-labeling, the absolute fluorescence intensity of fluorescein (part of the biosensor) was measured on the FL1 channel and compared for aliquots of both labeled cell line under identical acquisition parameters (BD FACSCalibur flow cytometer with BD CellQuest Pro Acquisition software). The data were analyzed using FlowJo analysis software. The absolute fluorescence from triplicate experiments is shown.

4.4.2. A scaffolded cryptophane biosensor targeting EGFR

Cell culture and cell-labeling was done by Dr. Jabadurai Jayapaul according to a modified protocol published by Palaniappan and coworkers.[75] The brief version of the protocol reads:

Cell culture:

Cells have been cultured under standard conditions (37 °C, 5 % CO_2, humidified atmosphere) as monolayers. Jurkat cells were grown in RPMI medium 1640. MDA-MB-231 cells were grown in DMEM/High glucose. Cell culture media has been supplemented with 10 % FBS.

Cell-labeling and sample preparation:

Cells (Jurkat and MDA-MB-231) were washed with DPBS and harvested by standard trypsination. Per labeling batch ca. 20 million cells were washed once with PBS buffer followed by incubation within 4000 µL of biosensor solution (5 nM CrA-M13-EGFR in blocking buffer: 1 % FCS in PBS). Biosensor incubation was done for 1 h at 4 °C under agitation. After labeling cells were washed with 4 mL of blocking buffer (3 times).

For NMR experiments with cells in solution 20 million labeled cells (Jurkat and MDA-MB-231) were resuspended within 2 mL of PBS buffer and transferred into the NMR sample phantom.

For MRI experiments within the bioreactor, 15 million labeled cells were washed with modified HBBS (three times) and encapsulated within alginate beads (15 mill/1 mL alginate solution) followed by bioreactor loading.

All media and reagents were purchased from Biochrom AG (Berlin, Germany).

4.4.3. A cryptophane biosensors targeting glycosylation

Cell culture and cell-labeling was done by Dr. Stefan Reinke and Dr. Honor May Rose as described in Ref. [115]. In brief, the following protocol was applied:

Cell culture and metabolic labeling (Ac_4ManNAz treatment):

DMEM, FBS superior, penicillin, streptomycin, Trypan Blue and PBS were purchased from Biochrom AG (Berlin, Germany). Chemicals were obtained from Roth (Karlsruhe, Germany).

Human embryonic kidney (HEK) 293 wild type cells were cultivated in Dulbecco's MEM with stable L-glutamine and 10 % fetal bovine serum (FBS), penicillin and streptomycin. Cell culture was done under standard conditions (5 % CO_2, 37°C). Positive (metabolically labeled) cells were treated for 3 days with Ac_4ManNAz (100 µM) by coincubation. Negative cells (metabolically unlabeled) were grown under standard conditions without Ac_4ManNAz treatment for the same time. After harvesting cells have been washed with PBS followed by live cell counting (Trypan Blue staining using a TC20™ Automated Cell Counter, Bio-Rad). All cells used in the experiments had >90 % viability.

Cell-labeling:

20 million positive (Ac_4ManNAz treated) and negative (untreated) cells were harvested and pelleted by centrifugation (400 g, 4 min, 25 °C). The cells were resuspended in 400 µL DPBS (Biochrome AG) containing 50 µM CrA-BCN. Incubation with CrA-BCN was done for 30 min at 37 °C. After incubation, cells were washed with modified HBBS (three times) and encapsulated within alginate beads.

4.4.4. Cell immobilization by alginate encapsulation

Cell encapsulation was done as described in Ref [151]. The labeled cells have been washed (3 times) and re-suspending in 1 mL modified Hank's Balanced Salt Solution without $CaCl_2$ and $MgSO_4$ (modified HBSS, H4641, Sigma Aldrich). The suspension of cells was further mixed with 1 mL of modified HBBS containing 2 % alginate (alginic acid sodium salt from brown algae, Sigma Aldrich) and 2 % mannitol. The cell-alginate solution (1 % alginate, 1 % mannitol in modified HBBS) was trickled into a solution containing 1.5 % $CaCl_2$ and 1 % mannitol by the use of a custom made droplet generator[97]. Polymerization was done for ca. 30 min under agitation at 4° C. The beads size (diameter of 1 mm) was controlled by the gas pressure at the droplet generator (ca. 1.5 bar). After encapsulation the labeled cells were incubated for additional 18 h within in Dulbecco's MEM with stable L-glutamine and 10 % fetal bovine serum (FBS) to reduce/equilibrate the calcium concentration within the alginate beads. Bead incubation was done within spinner vessels (stirring speed: 30 rpm) under standard cell culture conditions (5 % CO_2, 37°C).

4.5. Hyper-CEST spectroscopy and imaging

4.5.1. Hardware

All NMR/MRI experiments were performed on a 9.4 T NMR spectrometer (Bruker Biospin, Ettlingen, Germany) equipped with gradient coils for imaging applications. For excitation and detection a double resonant probe (^{129}Xe and ^{1}H) with an inner diameter of 10 mm was used.

4.5.2. Data acquisition

Following the delivery of hp-xenon, a continuous wave saturation pulse was applied to achieve CEST weighting before signal acquisition of free xenon in solution. Frequency, length and power of the saturation pulse were adjusted for each experiment individually as given within the results section.

Spectroscopy:
Experiments have been performed in Topspin 2.OPV (Bruker BioSpin MRI GmbH, Ettlingen, Germany).

Imaging:
Experiments have been performed in ParaVision Version 5.1 (Bruker BioSpin MRI GmbH, Ettlingen, Germany). All MR images were acquired using fast hyper-CEST-adapted single-shot sequences [70] with the same in plane geometry (field of view = 20 x 20 mm^2, matrix size = 32 x 32, in-plane resolution = 625 µm) and a 90 degree Gaussian-shaped excitation pulse. For experiments with direct xenon delivery, an echo planar imaging (EPI) readout (slice thickness = 22 mm, Fourier acceleration factor = 1.68, double sampling, bandwidth = 101 kHz, echo time = 5.7 ms, acquisition time = 19.8 ms) was used. A Rapid Acquisition with Relaxation Enhancement (RARE [152]) readout (slice thickness = 20 mm, centric *k*-space encoding, bandwidth = 5 kHz, echo time = 10 ms, acquisition time = 320 ms, rare factor = 32) was employed for imaging experiments based on continuous perfusion with xenon saturated medium (indirect xenon delivery).

4.5.3. Data post processing:

Image processing was done using MATLAB (R2012a, MathWorks, Natick, MA). CEST-spectra were fitted by using an exponential Lorentzian function[102] in OriginPro 8.6.OG (OriginLab, Northampton, MA).

References

1. Spiegel, P. K. The first clinical X-ray made in America--100 years. *AJR Am. J. Roentgenol.* 164, 241–243 (1995).
2. Timeline - Developments in medical imaging. *Sciencelearn Hub* at <http://sciencelearn.org.nz/Contexts/See-through-Body/Timeline>
3. Jain, R. K. Delivery of molecular medicine to solid tumors: lessons from in vivo imaging of gene expression and function. *J. Controlled Release* 74, 7–25 (2001).
4. Matsumura, T. *et al.* Safety of Gadopentetate Dimeglumine after 120 Million Administrations over 25 Years of Clinical Use. *Magn. Reson. Med. Sci.* 12, 297–304 (2013).
5. Schreiber, H. & Rowley, D. A. Awakening Immunity. *Science* 330, 761–762 (2010).
6. Hussain, T. & Nguyen, Q. T. Molecular imaging for cancer diagnosis and surgery. *Adv. Drug Deliv. Rev.* 66, 90–100 (2014).
7. Weissleder, R. Molecular Imaging in Cancer. *Science* 312, 1168–1171 (2006).
8. Siegel, R., Ma, J., Zou, Z. & Jemal, A. Cancer statistics, 2014. *CA. Cancer J. Clin.* 64, 9–29 (2014).
9. James, M. L. & Gambhir, S. S. A Molecular Imaging Primer: Modalities, Imaging Agents, and Applications. *Physiol. Rev.* 92, 897–965 (2012).
10. Janjic, J. M. & Ahrens, E. T. Fluorine-containing nanoemulsions for MRI cell tracking. *Wiley Interdiscip. Rev. Nanomed. Nanobiotechnol.* 1, 492–501 (2009).
11. Koh, M. B. C. & Suck, G. Cell therapy: promise fulfilled? *Biol. J. Int. Assoc. Biol. Stand.* 40, 214–217 (2012).
12. Winter, P. M. *et al.* Molecular Imaging of Angiogenesis in Nascent Vx-2 Rabbit Tumors Using a Novel αvβ3-targeted Nanoparticle and 1.5 Tesla Magnetic Resonance Imaging. *Cancer Res.* 63, 5838–5843 (2003).
13. Barrett, J. A. *et al.* First-in-man evaluation of 2 high-affinity PSMA-avid small molecules for imaging prostate cancer. *J. Nucl. Med. Off. Publ. Soc. Nucl. Med.* 54, 380–387 (2013).
14. Tran Cao, H. S. *et al.* Tumor-specific fluorescence antibody imaging enables accurate staging laparoscopy in an orthotopic model of pancreatic cancer. *Hepatogastroenterology.* 59, 1994–1999 (2012).
15. Weissleder, R. & Mahmood, U. Molecular Imaging. *Radiology* 219, 316–333 (2001).
16. Shilo, M., Reuveni, T., Motiei, M. & Popovtzer, R. Nanoparticles as computed tomography contrast agents: current status and future perspectives. *Nanomed.* 7, 257–269 (2012).
17. Rabin, O., Manuel Perez, J., Grimm, J., Wojtkiewicz, G. & Weissleder, R. An X-ray computed tomography imaging agent based on long-circulating bismuth sulphide nanoparticles. *Nat. Mater.* 5, 118–122 (2006).
18. Buck, A. K. *et al.* Economic evaluation of PET and PET/CT in oncology: evidence and methodologic approaches. *J. Nucl. Med. Technol.* 38, 6–17 (2010).
19. Fletcher, J. W. *et al.* A comparison of the diagnostic accuracy of 18F-FDG PET and CT in the characterization of solitary pulmonary nodules. *J. Nucl. Med. Off. Publ. Soc. Nucl. Med.* 49, 179–185 (2008).
20. Huang, B., Law, M. W.-M. & Khong, P.-L. Whole-Body PET/CT Scanning: Estimation of Radiation Dose and Cancer Risk. *Radiology* 251, 166–174 (2009).
21. Kresse, M. *et al.* Targeting of ultrasmall superparamagnetic iron oxide (USPIO) particles to tumor cells in vivo by using transferrin receptor pathways. *Magn. Reson. Med. Off. J. Soc. Magn. Reson. Med. Soc. Magn. Reson. Med.* 40, 236–242 (1998).
22. Sun, C., Sze, R. & Zhang, M. Folic acid-PEG conjugated superparamagnetic nanoparticles for targeted cellular uptake and detection by MRI. *J. Biomed. Mater. Res. A* 78A, 550–557 (2006).
23. Ahrens, E. T. & Bulte, J. W. M. Tracking immune cells in vivo using magnetic resonance imaging. *Nat. Rev. Immunol.* 13, 755–763 (2013).
24. Sosnovik, D. E., Nahrendorf, M. & Weissleder, R. Molecular Magnetic Resonance Imaging in Cardiovascular Medicine. *Circulation* 115, 2076–2086 (2007).

25. Rudin, M. & Weissleder, R. Molecular imaging in drug discovery and development. *Nat. Rev. Drug Discov.* 2, 123–131 (2003).

26. Hashemi, R. H., Bradley, W. G. & Lisanti, C. J. *MRI: The Basics*. (Lippincott Williams & Wilkins, 2012).

27. Morawski, A. M. *et al.* Targeted nanoparticles for quantitative imaging of sparse molecular epitopes with MRI. *Magn. Reson. Med. Off. J. Soc. Magn. Reson. Med. Soc. Magn. Reson. Med.* 51, 480–486 (2004).

28. Lebel, R. *et al.* Novel solubility-switchable MRI agent allows the noninvasive detection of matrix metalloproteinase-2 activity in vivo in a mouse model. *Magn. Reson. Med. Off. J. Soc. Magn. Reson. Med. Soc. Magn. Reson. Med.* 60, 1056–1065 (2008).

29. Olson, E. S. *et al.* Activatable cell penetrating peptides linked to nanoparticles as dual probes for in vivo fluorescence and MR imaging of proteases. *Proc. Natl. Acad. Sci. U. S. A.* 107, 4311–4316 (2010).

30. Castelli, D. D., Terreno, E., Longo, D. & Aime, S. Nanoparticle-based chemical exchange saturation transfer (CEST) agents: NANOPARTICLE-BASED CEST AGENTS. *NMR Biomed.* 26, 839–849 (2013).

31. Aime, S., Delli Castelli, D. & Terreno, E. Highly sensitive MRI chemical exchange saturation transfer agents using liposomes. *Angew. Chem. Int. Ed Engl.* 44, 5513–5515 (2005).

32. Flament, J. *et al.* In vivo CEST MR imaging of U87 mice brain tumor angiogenesis using targeted LipoCEST contrast agent at 7 T. *Magn. Reson. Med.* 69, 179–187 (2013).

33. Witte, C. & Schröder, L. NMR of hyperpolarised probes. *NMR Biomed.* 26, 788–802 (2013).

34. Wilson, D. M. & Kurhanewicz, J. Hyperpolarized 13C MR for Molecular Imaging of Prostate Cancer. *J. Nucl. Med.* 55, 1567–1572 (2014).

35. Bhattacharya, P. *et al.* Parahydrogen-induced polarization (PHIP) hyperpolarized MR receptor imaging in vivo: a pilot study of 13C imaging of atheroma in mice. *NMR Biomed.* 24, 1023–1028 (2011).

36. Dmochowski, I. Xenon out of its shell. *Nat. Chem.* 1, 250–250 (2009).

37. Lachmann, B. *et al.* Safety and efficacy of xenon in routine use as an inhalational anaesthetic. *The Lancet* 335, 1413–1415 (1990).

38. Goodson, B. M. Nuclear Magnetic Resonance of Laser-Polarized Noble Gases in Molecules, Materials, and Organisms. *J. Magn. Reson.* 155, 157–216 (2002).

39. Tomaselli, M., Meier, B. H., Robyr, P., Suter, U. W. & Ernst, R. R. Probing microheterogeneity in polymer systems via two-dimensional 129xenon NMR spy detection. A heterogeneous model blend system. *Chem. Phys. Lett.* 205, 145–152 (1993).

40. Moudrakovski, I. L. *et al.* Chemical Shift Imaging with Continuously Flowing Hyperpolarized Xenon for the Characterization of Materials. *J. Magn. Reson.* 144, 372–377 (2000).

41. Bowers, C. R. *et al.* Exploring Surfaces and Cavities in Lipoxygenase and Other Proteins by Hyperpolarized Xenon-129 NMR. *J. Am. Chem. Soc.* 121, 9370–9377 (1999).

42. Dubois, L. *et al.* Probing the Hydrophobic Cavity of Lipid Transfer Protein from Nicotiana tabacum through Xenon-Based NMR Spectroscopy. *J. Am. Chem. Soc.* 126, 15738–15746 (2004).

43. Palaniappan, K. K., Francis, M. B., Pines, A. & Wemmer, D. E. Molecular Sensing Using Hyperpolarized Xenon NMR Spectroscopy. *Isr. J. Chem.* 54, 104–112 (2014).

44. Schröder, L. Xenon for NMR biosensing – Inert but alert. *Phys. Med.* 29, 3–16 (2013).

45. Witte, C., Kunth, M., Rossella, F. & Schröder, L. Observing and preventing rubidium runaway in a direct-infusion xenon-spin hyperpolarizer optimized for high-resolution hyper-CEST (chemical exchange saturation transfer using hyperpolarized nuclei) NMR. *J. Chem. Phys.* 140, 084203 (2014).

46. Walker, T. G. & Happer, W. Spin-exchange optical pumping of noble-gas nuclei. *Rev. Mod. Phys.* 69, 629–642 (1997).

47. Nikolaou, P. *et al.* XeNA: An automated 'open-source' 129Xe hyperpolarizer for clinical use. *Magn. Reson. Imaging* 32, 541–550 (2014).

48. Mugler, J. P. & Altes, T. A. Hyperpolarized 129Xe MRI of the human lung. *J. Magn. Reson. Imaging* 37, 313–331 (2013).

49. Cleveland, Z. I. *et al.* Hyperpolarized 129Xe MR Imaging of Alveolar Gas Uptake in Humans. *PLoS ONE* 5, e12192 (2010).

50. Cleveland, Z. I. *et al.* In Vivo MR Imaging of Pulmonary Perfusion and Gas Exchange in Rats via Continuous Extracorporeal Infusion of Hyperpolarized 129Xe. *PLoS ONE* 7, e31306 (2012).

51. Zhou, X. *et al.* MRI of stroke using hyperpolarized 129Xe. *NMR Biomed.* 24, 170–175 (2011).

52. Mazzanti, M. L. *et al.* Distribution of Hyperpolarized Xenon in the Brain Following Sensory Stimulation: Preliminary MRI Findings. *PLoS ONE* 6, e21607 (2011).

53. Choquet, P. *et al.* Method to determine in vivo the relaxation time T1 of hyperpolarized xenon in rat brain. *Magn. Reson. Med.* 49, 1014–1018 (2003).

54. Duhamel, G. *et al.* Xenon-129 MR imaging and spectroscopy of rat brain using arterial delivery of hyperpolarized xenon in a lipid emulsion. *Magn. Reson. Med.* 46, 208–212 (2001).

55. Shapiro, M. G. *et al.* Genetically encoded reporters for hyperpolarized xenon magnetic resonance imaging. *Nat. Chem.* 6, 629–634 (2014).

56. Driehuys, B., Möller, H. E., Cleveland, Z. I., Pollaro, J. & Hedlund, L. W. Pulmonary Perfusion and Xenon Gas Exchange in Rats: MR Imaging with Intravenous Injection of Hyperpolarized 129Xe1. *Radiology* 252, 386–393 (2009).

57. Brotin, T. & Dutasta, J.-P. Cryptophanes and Their Complexes—Present and Future. *Chem. Rev.* 109, 88–130 (2009).

58. Bartik, K., Luhmer, M., Heyes, S. J., Ottinger, R. & Reisse, J. Probing Molecular Cavities in α-Cyclodextrin Solutions by Xenon NMR. *J. Magn. Reson. B* 109, 164–168 (1995).

59. Dubes, A. *et al.* Distribution and Modification of Sorption Sites in Amphiphilic Calixarene-Based Solid Lipid Nanoparticles from Hyperpolarized 129Xe NMR Spectroscopy. *J. Am. Chem. Soc.* 126, 6236–6237 (2004).

60. Kim, B. S. *et al.* Water soluble cucurbit[6]uril derivative as a potential Xe carrier for 129Xe NMR-based biosensors. *Chem. Commun. Camb. Engl.* 2756–2758 (2008). doi:10.1039/b805724a

61. Claessens, M., Fabre, O., Zimmermann, D. & Reisse, J. N.M.R. Study of Molecular Interactions between Xenon and Crown Ethers. *Bull. Sociétés Chim. Belg.* 93, 983–990 (1984).

62. Desvaux, H. *et al.* Dynamics of Xenon Binding Inside the Hydrophobic Cavity of Pseudo-Wild-type Bacteriophage T4 Lysozyme Explored through Xenon-Based NMR Spectroscopy. *J. Am. Chem. Soc.* 127, 11676–11683 (2005).

63. McKim, S. & Hinton, J. F. Evidence of xenon transport through the gramicidin channel: a 129Xe-NMR study. *Biochim. Biophys. Acta BBA - Biomembr.* 1193, 186–198 (1994).

64. Tilton, R. F. & Kuntz, I. D. Nuclear magnetic resonance studies of xenon-129 with myoglobin and hemoglobin. *Biochemistry (Mosc.)* 21, 6850–6857 (1982).

65. Dong, Z., Luo, Q. & Liu, J. Artificial enzymes based on supramolecular scaffolds. *Chem. Soc. Rev.* 41, 7890 (2012).

66. Taratula, O., Hill, P. A., Khan, N. S., Carroll, P. J. & Dmochowski, I. J. Crystallographic observation of 'induced fit' in a cryptophane host–guest model system. *Nat. Commun.* 1, 148 (2010).

67. Spence, M. M. *et al.* Functionalized xenon as a biosensor. *Proc. Natl. Acad. Sci.* 98, 10654–10657 (2001).

68. Kilian, W., Seifert, F. & Rinneberg, H. Dynamic NMR spectroscopy of hyperpolarized (129)Xe in human brain analyzed by an uptake model. *Magn. Reson. Med. Off. J. Soc. Magn. Reson. Med. Soc. Magn. Reson. Med.* 51, 843–847 (2004).

69. Schröder, L., Lowery, T. J., Hilty, C., Wemmer, D. E. & Pines, A. Molecular Imaging Using a Targeted Magnetic Resonance Hyperpolarized Biosensor. *Science* 314, 446–449 (2006).

70. Kunth, M., Döpfert, J., Witte, C., Rossella, F. & Schröder, L. Optimized Use of Reversible Binding for Fast and Selective NMR Localization of Caged Xenon. *Angew. Chem. Int. Ed Engl.* 33, 8217–8220 (2012).

71. Döpfert, J., Witte, C. & Schröder, L. Fast Gradient-Encoded CEST Spectroscopy of Hyperpolarized Xenon. *ChemPhysChem* 15, 261–264 (2014).

72. Rubin, S. M., Spence, M. M., Goodson, B. M., Wemmer, D. E. & Pines, A. Evidence of nonspecific surface interactions between laser-polarized xenon and myoglobin in solution. *Proc. Natl. Acad. Sci.* 97, 9472–9475 (2000).

73. Boutin, C. *et al.* Hyperpolarized 129Xe NMR signature of living biological cells. *NMR Biomed.* 24, 1264–1269 (2011).

74. Han, S.-I. *et al.* NMR-Based Biosensing with Optimized Delivery of Polarized 129Xe to Solutions. *Anal. Chem.* 77, 4008–4012 (2005).

75. Palaniappan, K. K. *et al.* Molecular Imaging of Cancer Cells Using a Bacteriophage-Based 129Xe NMR Biosensor. *Angew. Chem. Int. Ed.* n/a–n/a (2013). doi:10.1002/anie.201300170

76. Baumer, D., Brunner, E., Blümler, P., Zänker, P. P. & Spiess, H. W. NMR Spectroscopy of Laser-Polarized 129Xe Under Continuous Flow: A Method To Study Aqueous Solutions of Biomolecules. *Angew. Chem. Int. Ed.* 45, 7282–7284 (2006).

77. Cleveland, Z. I., Möller, H. E., Hedlund, L. W. & Driehuys, B. Continuously Infusing Hyperpolarized 129Xe into Flowing Aqueous Solutions Using Hydrophobic Gas Exchange Membranes. *J. Phys. Chem. B* 113, 12489–12499 (2009).

78. Hilty, C., Lowery, T. J., Wemmer, D. E. & Pines, A. Spectrally Resolved Magnetic Resonance Imaging of a Xenon Biosensor. *Angew. Chem. Int. Ed.* 45, 70–73 (2006).

79. Qing, K. *et al.* Regional mapping of gas uptake by blood and tissue in the human lung using hyperpolarized xenon-129 MRI. *J. Magn. Reson. Imaging* (2013). doi:10.1002/jmri.24181

80. Shukla, Y. *et al.* Hyperpolarized 129Xe magnetic resonance imaging: tolerability in healthy volunteers and subjects with pulmonary disease. *Acad. Radiol.* 19, 941–951 (2012).

81. Aaron, J. A. *et al.* Structure of a 129Xe-Cryptophane Biosensor Complexed with Human Carbonic Anhydrase II. *J. Am. Chem. Soc.* 130, 6942–6943 (2008).

82. Chambers, J. M. *et al.* Cryptophane Xenon-129 Nuclear Magnetic Resonance Biosensors Targeting Human Carbonic Anhydrase. *J. Am. Chem. Soc.* 131, 563–569 (2009).

83. Wei, Q. *et al.* Designing 129Xe NMR Biosensors for Matrix Metalloproteinase Detection. *J. Am. Chem. Soc.* 128, 13274–13283 (2006).

84. Roy, V. *et al.* A Cryptophane Biosensor for the Detection of Specific Nucleotide Targets through Xenon NMR Spectroscopy. *ChemPhysChem* 8, 2082–2085 (2007).

85. Schlundt, A. *et al.* A xenon-129 biosensor for monitoring MHC-peptide interactions. *Angew. Chem. Int. Ed Engl.* 48, 4142–4145 (2009).

86. Seward, G. K., Wei, Q. & Dmochowski, I. J. Peptide-Mediated Cellular Uptake of Cryptophane. *Bioconjug. Chem.* 19, 2129–2135 (2008).

87. Boutin, C. *et al.* Cell uptake of a biosensor detected by hyperpolarized 129Xe NMR: the transferrin case. *Bioorg. Med. Chem.* 19, 4135–4143 (2011).

88. Meldrum, T., Schröder, L., Denger, P., Wemmer, D. E. & Pines, A. Xenon-based molecular sensors in lipid suspensions. *J. Magn. Reson. San Diego Calif 1997* 205, 242–246 (2010).

89. Stevens, T. K., Ramirez, R. M. & Pines, A. Nanoemulsion contrast agents with sub-picomolar sensitivity for xenon NMR. *J. Am. Chem. Soc.* (2013). doi:10.1021/ja402885q

90. Wolber, J., Rowland, I. J., Leach, M. O. & Bifone, A. Perfluorocarbon emulsions as intravenous delivery media for hyperpolarized xenon. *Magn. Reson. Med.* 41, 442–449 (1999).

91. Barnett, B. P. *et al.* Use of perfluorocarbon nanoparticles for non-invasive multimodal cell tracking of human pancreatic islets. *Contrast Media Mol. Imaging* 6, 251–259 (2011).

92. Tirotta, I. *et al.* 19F Magnetic Resonance Imaging (MRI): From Design of Materials to Clinical Applications. *Chem. Rev.* (2014). doi:10.1021/cr500286d

93. Ahrens, E. T. & Zhong, J. In vivo MRI cell tracking using perfluorocarbon probes and fluorine-19 detection. *NMR Biomed.* 26, 860–871 (2013).

94. Lanza, G. M. *et al.* A Novel Site-Targeted Ultrasonic Contrast Agent With Broad Biomedical Application. *Circulation* 94, 3334–3340 (1996).

95. Giraudeau, C. *et al.* 19F molecular MR imaging for detection of brain tumor angiogenesis: in vivo validation using targeted PFOB nanoparticles. *Angiogenesis* 16, 171–179 (2013).

96. Bimodal Perfluorocarbon Nanoemulsions for Nasopharyngeal Carcinoma Targeting - Springer. doi:10.1007/s11307-013-0622-2

97. León Fiszman, G., Karara, A. L., Finocchiaro, L. M. E. & Glikin, G. C. A laboratory scale device for microencapsulation of genetically engineered cells into alginate beads. *Electron. J. Biotechnol.* 5, 23–24 (2002).

98. Klippel, S. *et al.* Cell Tracking with Caged Xenon: Using Cryptophanes as MRI Reporters upon Cellular Internalization. *Angew. Chem. Int. Ed.* 53, 493–496 (2014).

99. Rossella, F., Rose, H. M., Witte, C., Jayapaul, J. & Schröder, L. Design and Characterization of Two Bifunctional Cryptophane A-Based Host Molecules for Xenon Magnetic Resonance Imaging Applications. *ChemPlusChem* (2014). doi:10.1002/cplu.201402179

100. Schröder, L. *et al.* Temperature Response of ^{129}Xe Depolarization Transfer and Its Application for Ultrasensitive NMR Detection. *Phys. Rev. Lett.* 100, 257603 (2008).

101. Sloniec, J. *et al.* Biomembrane Interactions of Functionalized Cryptophane-A: Combined Fluorescence and 129Xe NMR Studies of a Bimodal Contrast Agent. *Chem. – Eur. J.* (2013). doi:10.1002/chem.201203773

102. Zaiss, M., Schnurr, M. & Bachert, P. Analytical solution for the depolarization of hyperpolarized nuclei by chemical exchange saturation transfer between free and encapsulated xenon (HyperCEST). *J. Chem. Phys.* 136, 144106–144106–10 (2012).

103. Kadayakkara, D. K., Ranganathan, S., Young, W.-B. & Ahrens, E. T. Assaying macrophage activity in a murine model of inflammatory bowel disease using fluorine-19 MRI. *Lab. Invest.* 92, 636–645 (2012).

104. Ahrens, E. T., Young, W.-B., Xu, H. & Pusateri, L. K. Rapid quantification of inflammation in tissue samples using perfluorocarbon emulsion and fluorine-19 nuclear magnetic resonance. *BioTechniques* 50, 229–234 (2011).

105. Ahrens, E. T., Flores, R., Xu, H. & Morel, P. A. In vivo imaging platform for tracking immunotherapeutic cells. *Nat. Biotechnol.* 23, 983–987 (2005).

106. Partlow, K. C. *et al.* 19F magnetic resonance imaging for stem/progenitor cell tracking with multiple unique perfluorocarbon nanobeacons. *FASEB J.* 21, 1647–1654 (2007).

107. Helfer, B. M. *et al.* 19F MRI Tracer Preserves In Vitro and In Vivo Properties of Hematopoietic Stem Cells. *Cell Transplant.* 22, 87–97 (2013).

108. Klippel, S., Freund, C. & Schröder, L. Multichannel MRI Labeling of Mammalian Cells by Switchable Nanocarriers for Hyperpolarized Xenon. *Nano Lett.* 14, 5721–5726 (2014).

109. Rose, H. M. *et al.* Development of an antibody-based, modular biosensor for 129Xe NMR molecular imaging of cells at nanomolar concentrations. *Proc. Natl. Acad. Sci.* 111, 11697–11702 (2014).

110. Li, R. H., Altreuter, D. H. & Gentile, F. T. Transport characterization of hydrogel matrices for cell encapsulation. *Biotechnol. Bioeng.* 50, 365–373 (1996).

111. Berthault, P. *et al.* Effect of pH and Counterions on the Encapsulation Properties of Xenon in Water-Soluble Cryptophanes. *Chem. – Eur. J.* 16, 12941–12946 (2010).

112. Mynar, J. L., Lowery, T. J., Wemmer, D. E., Pines, A. & Fréchet, J. M. J. Xenon Biosensor Amplification via Dendrimer−Cage Supramolecular Constructs. *J. Am. Chem. Soc.* 128, 6334–6335 (2006).

113. Meldrum, T. *et al.* A Xenon-Based Molecular Sensor Assembled on an MS2 Viral Capsid Scaffold. *J. Am. Chem. Soc.* 132, 5936–5937 (2010).

114. Stevens, T. K. *et al.* HyperCEST detection of a ^{129} Xe-based contrast agent composed of cryptophane-A molecular cages on a bacteriophage scaffold. *Magn. Reson. Med.* 69, 1245–1252 (2013).

115. Witte, C. *et al.* Live-cell MRI of xenon Hyper-CEST biosensors targeted to metabolically-labeled cell-surface glycans. *in press*, DOI: 10.1002/anie.201410573R1.

116. Walczak, P., Kedziorek, D. A., Gilad, A. A., Lin, S. & Bulte, J. W. M. Instant MR labeling of stem cells using magnetoelectroporation. *Magn. Reson. Med. Off. J. Soc. Magn. Reson. Med. Soc. Magn. Reson. Med.* 54, 769–774 (2005).

117. Rogers, W. J., Meyer, C. H. & Kramer, C. M. Technology Insight: in vivo cell tracking by use of MRI. *Nat. Clin. Pract. Cardiovasc. Med.* 3, 554–562 (2006).

118. Schnurr, M., Sydow, K., Rose, H. M., Dathe, M. & Schröder, L. Brain Endothelial Cell Targeting Via a Peptide-Functionalized Liposomal Carrier for Xenon Hyper-CEST MRI. *Adv. Healthc. Mater.* (2014). doi:10.1002/adhm.201400224

119. Alberts, B. *et al.* Transport into the Cell from the Plasma Membrane: Endocytosis. (2002). at <http://www.ncbi.nlm.nih.gov/books/NBK26870/>

120. Helfer, B. M. *et al.* Functional assessment of human dendritic cells labeled for in vivo (19)F magnetic resonance imaging cell tracking. *Cytotherapy* 12, 238–250 (2010).

121. Te Boekhorst, B. C., van Tilborg, G. A., Strijkers, G. J. & Nicolay, K. Molecular MRI of Inflammation in Atherosclerosis. *Curr. Cardiovasc. Imaging Rep.* 5, 60–68 (2012).

122. Daldrup-Link, H. E. *et al.* MR Imaging of Tumor Associated Macrophages with Clinically-Applicable Iron Oxide Nanoparticles. *Clin. Cancer Res. Off. J. Am. Assoc. Cancer Res.* 17, 5695–5704 (2011).

123. Hammers, C. M. & Stanley, J. R. Antibody phage display: technique and applications. *J. Invest. Dermatol.* 134, e17 (2014).

124. Kunth, M., Witte, C. & Schröder, L. Quantitative chemical exchange saturation transfer with hyperpolarized nuclei (qHyper-CEST): Sensing xenon-host exchange dynamics and binding affinities by NMR. *J. Chem. Phys.* 141, 194202 (2014).

125. Noble, G. T., Stefanick, J. F., Ashley, J. D., Kiziltepe, T. & Bilgicer, B. Ligand-targeted liposome design: challenges and fundamental considerations. *Trends Biotechnol.* 32, 32–45 (2014).

126. Van der Meel, R. *et al.* Extracellular vesicles as drug delivery systems: Lessons from the liposome field. *J. Control. Release Off. J. Control. Release Soc.* (2014). doi:10.1016/j.jconrel.2014.07.049

127. Klibanov, A. L., Maruyama, K., Torchilin, V. P. & Huang, L. Amphipathic polyethyleneglycols effectively prolong the circulation time of liposomes. *FEBS Lett.* 268, 235–237 (1990).

128. Chang, H.-I. & Cheng, M.-Y. Clinically-Proven Liposome-Based Drug Delivery: Formulation, Characterization and Therapeutic Efficacy. *J. Nanomedicine Biotherapeutic Discov.* 01, (2012).

129. Campbell, C. T., Sampathkumar, S.-G. & Yarema, K. J. Metabolic oligosaccharide engineering: perspectives, applications, and future directions. *Mol. Biosyst.* 3, 187–194 (2007).

130. Prescher, J. A. & Bertozzi, C. R. Chemistry in living systems. *Nat. Chem. Biol.* 1, 13–21 (2005).

131. Dube, D. H. & Bertozzi, C. R. Glycans in cancer and inflammation--potential for therapeutics and diagnostics. *Nat. Rev. Drug Discov.* 4, 477–488 (2005).

132. Suwa, T., Ozawa, S., Ueda, M., Ando, N. & Kitajima, M. Magnetic resonance imaging of esophageal squamous cell carcinoma using magnetite particles coated with anti-epidermal growth factor receptor antibody. *Int. J. Cancer* 75, 626–634 (1998).

133. Neves, A. A. *et al.* Imaging Cell Surface Glycosylation in Vivo Using 'Double Click' Chemistry. *Bioconjug. Chem.* 24, 934–941 (2013).

134. Cipolla, L., Gregori, M. & So, P.-W. Glycans in Magnetic Resonance Imaging: Determinants of Relaxivity to Smart Agents, and Potential Applications in Biomedicine. *Curr. Med. Chem.* 18, 1002–1018 (2011).

135. Gao, X., Cui, Y., Levenson, R. M., Chung, L. W. K. & Nie, S. In vivo cancer targeting and imaging with semiconductor quantum dots. *Nat. Biotechnol.* 22, 969–976 (2004).

136. Freire, M. G., Dias, A. M. A., Coelho, M. A. Z., Coutinho, J. A. P. & Marrucho, I. M. Aging mechanisms of perfluorocarbon emulsions using image analysis. *J. Colloid Interface Sci.* 286, 224–232 (2005).

137. Janjic, J. M., Srinivas, M., Kadayakkara, D. K. K. & Ahrens, E. T. Self-delivering Nanoemulsions for Dual Fluorine-19 MRI and Fluorescence Detection. *J. Am. Chem. Soc.* 130, 2832–2841 (2008).

138. Bae, P. K. & Chung, B. H. Multiplexed detection of various breast cancer cells by perfluorocarbon/quantum dot nanoemulsions conjugated with antibodies. *Nano Converg.* 1, 1–8 (2014).

139. Vandsburger, M. H., Radoul, M., Cohen, B. & Neeman, M. MRI reporter genes: applications for imaging of cell survival, proliferation, migration and differentiation. *NMR Biomed.* (2012). doi:10.1002/nbm.2869

140. Schaffer, D. V., Koerber, J. T. & Lim, K. Molecular engineering of viral gene delivery vehicles. *Annu. Rev. Biomed. Eng.* 10, 169–194 (2008).

141. Shapiro, M. G. *et al.* Biogenic gas nanostructures as ultrasonic molecular reporters. *Nat. Nanotechnol.* 9, 311–316 (2014).

142. Mura, S., Nicolas, J. & Couvreur, P. Stimuli-responsive nanocarriers for drug delivery. *Nat. Mater.* 12, 991–1003 (2013).

143. Al-Jamal, W. T. & Kostarelos, K. Liposomes: from a clinically established drug delivery system to a nanoparticle platform for theranostic nanomedicine. *Acc. Chem. Res.* 44, 1094–1104 (2011).

144. Wolber, J., Cherubini, A., Dzik-Jurasz, A. S. K., Leach, M. O. & Bifone, A. Spin-lattice relaxation of laser-polarized xenon in human blood. *Proc. Natl. Acad. Sci.* 96, 3664–3669 (1999).

145. Zhou, X. *et al.* Reinvestigating hyperpolarized (129)Xe longitudinal relaxation time in the rat brain with noise considerations. *NMR Biomed.* 21, 217–225 (2008).

146. De Vries, I. J. M. *et al.* Magnetic resonance tracking of dendritic cells in melanoma patients for monitoring of cellular therapy. *Nat. Biotechnol.* 23, 1407–1413 (2005).

147. Bentolila, L. A., Ebenstein, Y. & Weiss, S. Quantum dots for in vivo small-animal imaging. *J. Nucl. Med. Off. Publ. Soc. Nucl. Med.* 50, 493–496 (2009).

148. Dinish, U. S., Balasundaram, G., Chang, Y.-T. & Olivo, M. Actively targeted in vivo multiplex detection of intrinsic cancer biomarkers using biocompatible SERS nanotags. *Sci. Rep.* 4, 4075 (2014).

149. Berthault, P., Bogaert-Buchmann, A., Desvaux, H., Huber, G. & Boulard, Y. Sensitivity and Multiplexing Capabilities of MRI Based on Polarized 129Xe Biosensors. *J. Am. Chem. Soc.* 130, 16456–16457 (2008).

150. Appelt, S. *et al.* Experimental studies of rubidium absolute polarization at high temperatures. *Appl. Phys. Lett.* 75, 427–429 (1999).

151. Orive, G., Hernández, R. M., Gascón, A. R. & Pedraz, J. L. in *Immobilization of Enzymes and Cells* (ed. Guisan, J. M.) 345–355 (Humana Press, 2006). at <http://link.springer.com/protocol/10.1007/978-1-59745-053-9_30>

152. Hennig, J., Nauerth, A. & Friedburg, H. RARE imaging: a fast imaging method for clinical MR. *Magn. Reson. Med. Off. J. Soc. Magn. Reson. Med. Soc. Magn. Reson. Med.* 3, 823–833 (1986).

Acknowledgment

First of all I thank my supervisors Dr. Leif Schröder and Prof. Dr. Christian Freund for their excellent intellectual, financial and personal support throughout the complete project. I thank Prof. Dr. Christian Freund especially for his confidence.

I further would like to thank Dr. Leif Schröder for creating an extraordinary friendly and dynamic research atmosphere and along with this for giving me the chance to see Europe, America and Asia. Related to the strong interdisciplinary challenges this work was a real team effort. I'm deeply grateful to all members of the "biosensor imaging" family including: Dr. Christopher Witte, Dr. Honor May Rose, Dr. Jabadurai Jayapaul as well my student "co-workers": Jörg Döpfert, Martin Kunth, Federica Rossella and Matthias Schnurr. Thanks you guys for your help, for sharing office, lab and free time.

I would like to say a special "thank you" to Chris, who was my mentor along the xenon project. Without his theoretical and practical skills and his willing to teach others, this thesis would not have been possible.

I want to thank all members of the FMP for providing assistance with new equipment, techniques and paperwork and in particular the people from the machine shop for building all the "strange devices" I was asking for.

I further want to express gratitude to Dr. Andreas Schlundt, who pointed my attention to the exciting field of xenon MRI and Dr. Peter Schmieder for teaching me what it means to be a NMR spectroscopist. Thank you all.

Publications and Conference contributions

Peer-reviewed journal publications

Witte C., Martos V., Rose H. M., Reinke S., **Klippel S.**, Schröder L. & Hackenberger C. (2015).
Live-cell MRI of xenon Hyper-CEST biosensors targeted to metabolically-labeled cell-surface glycans.
Angewandte Chemie International Edition, in press, DOI: 10.1002/anie.201410573R1.

Klippel S., Freund C., & Schröder, L (2014).
Multichannel MRI Labeling of Mammalian Cells by Switchable Nanocarriers for Hyperpolarized Xenon.
Nano Letters, *14*(10), 5721–5726.

Rose H. M., Witte C., Rossella F., **Klippel S.**, Freund C., & Schröder L. (2014).
Development of an antibody-based, modular biosensor for 129Xe NMR molecular imaging of cells at nanomolar concentrations.
Proceedings of the National Academy of Sciences of the United States of America. *111*(32), 11697–702.

Klippel S., Döpfert J., Jayapaul J., Kunth M., Rossella F., Schnurr M., Freund C., & Schröder L. (2014).
Cell-tracking with Caged Xenon: Using Cryptophanes as MRI Reporters upon Cellular Internalization.
Angewandte Chemie International Edition, *53*(2), 493–496.

Klippel S., Wieczorek, M., Schümann M., Krause E., Marg B., Seidel T. Freund C. (2011).
Multivalent Binding of Formin-binding Protein 21 (FBP21)-Tandem-WW Domains Fosters Protein Recognition in the Pre-spliceosome.
Journal of Biological Chemistry, *286*(44), 38478–38487.

Oral presentations at conferences

"Multi-channel MRI cell-labeling with hyperpolarized xenon"
World Molecular Imaging Congress (WMIC), 2014, Seoul, South Korea

"Xenon-Based Hyper-CEST-MRI of Cryptophane Labeled Cells"
EUROMAR, 2013, Hersonissos, Crete, Greece

Poster presentations at conferences

"Xenon Based Hyper-CEST-MRI of Cryptophane Labeled Cells"
56th Experimental Nuclear Magnetic Resonance Conference (ENC), 2013
Pacific Grove, California, USA